(Plasmonic Metal Core)/(Semiconductor Shell) Nanostructures

具有表面等離子體激元特性的金屬/半導體核/殼納米結構

FANG, Caihong

房彩虹

A Thesis Submitted in Partial Fulfillment

of the Requirements for the Degree of

Doctor of Philosophy

in

Materials Science and Engineering

The Chinese University of Hong Kong

August 2014

Thesis/Assessment Committee

Professor XIAO, Xudong (Chair)
Professor WANG, Jianfang (Thesis Supervisor)
Professor YU, Chai Mei Jimmy (Committee Member)
Professor YANG, Zhi (External Examiner)

Abstract

Over the past several years, integration of metal nanocrystals that can support localized surface plasmon has been demonstrated as one of the most promising methods to the improvement of the light-harvesting efficiency of semiconductors. Ag and Au nanocrystals have been extensively hybridized with semiconductors by either deposition or anchoring. However, metal nanocrystals tend to aggregate, reshape, detach, or grow into large nanocrystals, leading to a loss of the unique properties seen in the original nanocrystals. Fortunately, core/shell nanostructures, circumventing the aforementioned problems, have been demonstrated to exhibit superior photoactivities. To further improve the light-harvesting applications of (plasmonic metal core)/(semiconductor shell) nanostructures, it is vital to understand the plasmonic and structural evolutions during the preparation processes, design novel hybrid nanostructures, and improve their light-harvesting performances. In this thesis, I therefore studied the plasmonic and structural evolutions during the formation of (Ag core)/(Ag_2S shell) nanostructures. Moreover, I also prepared (noble metal core)/(TiO_2 shell) nanostructures and investigated their plasmonic properties and photon-harvesting applications.

Clear understanding of the sulfidation process can enable fine control of the plasmonic properties as well as the structural composition of Ag/Ag_2S nanomaterials. Therefore, I investigated the plasmonic and structural variations during the sulfidation process of Ag nanocubes both experimentally and numerically. The sulfidation reactions were carried out at both the ensemble and single-particle levels. Electrodynamic simulations were also employed to study the variations of the plasmonic properties and plasmon modes. Both experiment and simulation results revealed that sulfidation initiates at the vertices of Ag nanocubes. Ag nanocubes are then gradually truncated and each nanocube becomes a nanosphere eventually. The cubic shape is maintained throughout the sulfidation process, with the edge length

being increased gradually.

TiO$_2$ is one of the most important semiconductors that are employed in light-harvesting applications. It has been extensively studied for a variety of applications by virtue of its low toxicity, biological compatibility, chemical and thermal stability, resistance to photocorrosion, and relative abundance. However, the photocatalytic activity of TiO$_2$ is limited to the UV region because of its wide band gap, which limits its applications in light harvesting. Although (Au core)/(TiO$_2$ shell) nanostructures can improve the photocatalytic activities of TiO$_2$ in visible light, it has only been demonstrated in a few experiments and has been limited with Au nanospheres. Compared with Au nanospheres, Au nanorods offer more attractive plasmonic features, including stronger electric field enhancements and synthetically tunable longitudinal plasmon wavelengths over the visible to near-infrared region. The coating of Au nanorod therefore can largely improve light harvesting capability of TiO$_2$. In this thesis, I developed a facile and versatile method for the preparation of (Au nanocrystal core)/(TiO$_2$ shell) nanostructures by using a Ti(III) compound as the titania precursor. By employing Au nanorods with different sizes and varying the shell thickness, the plasmonic bands of the core/shell nanostructures can be tailored. TiO$_2$ can also be grown on other monometallic and bimetallic Pd, Pt, Au nanocrystals. As a proof-of-concept application, (Au nanorod core)/(TiO$_2$ shell) nanostructures were utilized in dye-sensitized solar cells to function as a scattering layer. The resultant solar cells exhibited higher power conversion efficiencies with a thinner thickness compared to the traditional TiO$_2$ solar cells. In addition, I also examined the property of plasmon-enhanced reactive oxygen species generation. Moreover, the TiO$_2$ shell with a high refractive index can efficiently couple with the plasmon resonance modes of the Au nanorod core, leading to Fano resonances. Fano resonances for both the transverse and longitudinal plasmon modes were simultaneously observed. The longitudinal Fano resonance is tunable by changing the plasmon energy of the nanorod core. In addition, coating with TiO$_2$ intensifies the transverse plasmon mode of the Au nanorod core.

I believe that my research study will be very helpful for the design and applications of metal/semiconductor nanostructures. The full understanding of the plasmonic and structural evolutions during the preparation processes will be useful for designing metal/semiconductor hybrid nanomaterials with desired compositions and plasmonic properties. The efforts towards the investigations of the preparation, plasmonic properties, and applications of (noble metal core)/(semiconductor shell) nanostructures are important for widening their light-harvesting applications.

摘要

通過與具有表面等離子體激元特性的金屬納米晶複合，半導體納米材料的捕光能力可以得到很大地提高。銀、金納米晶因其獨特的表面等離子體特性，已被廣泛應用于半導體複合物的製備。其中通過沉積或者粘合方式得到的複合物存在一定弊端，比如：金屬納米晶暴露在實驗環境中，導致其團聚、變形、脫落、或者長大，使原有的獨特表面等離子特性改變或消失。核/殼結構納米材料可以有效地避免以上問題，因而表現出優越的光活性。爲了進一步拓寬金屬/半導體核/殼結構在光能捕獲方面的應用，我們需要深入理解製備過程中表面等離子體激元特性及材料結構的變化、設計合成新的納米材料。在這篇畢業論文中，我研究了在製備 Ag/Ag$_2$S 核/殼結構過程中的表面等離子體特性及材料結構的變化，制備了 Au/TiO$_2$ 核/殼結構，并對他們的應用及表面等離子體共振激元特性進行了研究。

理解硫化過程有助於更好的控制其表面等離子體特性和結構組成。因此，我分別從實驗和數值模擬兩方面研究了銀納米立方塊在硫化過程中表面等離子體特性及其相應 Ag/Ag$_2$S 核/殼的組成及結構的變化。硫化反應分別在溶液及單顆粒環境下進行。同時，我們應用數值模擬計算揭示硫化過程中表面等離子體特性及模式變化。實驗和數值計算均表明硫化反應首先發生在銀納米立方塊的棱角和頂點。隨著反應的進行，銀立方塊被逐步鈍化為球狀銀納米顆粒。與此同時，納米立方結構的尺寸也隨之小幅增加。

二氧化鈦是一種重要的被應用於光能捕獲的半導體納米材料。因其低毒性、生物兼容性、化學及熱穩定性、耐光腐蝕性以及資源豐富等特點，TiO$_2$ 已經被廣泛研究。但是 TiO$_2$ 僅在紫外光區具有光化學活性，這大大限制了其在光能捕獲方面的應用。儘管 Au/TiO$_2$ 核/殼結構複合物可以提高 TiO$_2$ 在可見區的光催化活性，但是對於該核/殼結構的合成鮮為報導，而且已報導的工作也是限制在以金納米球作為核層。與金納米球相比，金納米棒具有更引人關注的表面等離子體特性，例如金納米棒具有更高的電場增強，而且金棒的縱向共振波長可以從可見

區調控到近紅外區。因此金納米棒/二氧化鈦核/殼結構可以更有效的提高二氧化鈦的光捕獲能力。在此論文中，我發展了一種合成 Au/TiO_2 核/殼結構的方法，并研究其在光能捕獲方面的應用。在該方法中，我選擇三價鈦作為鈦源，可控合成了 Au/TiO_2 核/殼結構。通過對核的尺寸及殼層厚度的調節，實現了對核/殼結構的共振波長的調控。另外這種方法也適用於其他單組份或者雙組份的鉑、鈀、金納米晶。爲了驗證在光能捕獲方面的應用潛能，Au/TiO_2 核/殼結構納米材料被作為散射層而應用於染料敏化太陽能電池中，結果發現這種電池具有較高光電轉化效率。另外，我們還研究了表面等離子體共振激元增強下的活性氧化物的生成。再者，具有較高介電常數的二氧化鈦殼層可以與金納米晶核耦合產生法諾共振效應。結果表明金納米棒的橫向、縱向共振峰均能和殼層材料發生共振耦合而產生對應的法諾效應。納米棒的縱向共振峰的可調性實現了對應的法諾共振峰的可調性。同時，包覆二氧化鈦殼層后，金納米棒的橫向共振模式被大幅放大。

本論文的研究有利於人們了解金屬/半導體納米結構的設計及應用。硫化過程中表面等離子體共振激元特性及結構變化的研究，對具有特定組分及共振特性的複合物的設計合成具有指導意義。對貴金屬/半導體核殼結構製備、共振特性及應用的研究也擴展了其在光能捕獲方面的應用。

Acknowledgements

This thesis does not just represent my work. It is much like a "diary" that records my changes and growth. When I look through my thesis, I can even remember the feelings I went through in both academic and personal lifetime when I did each work. Living through the happiness, perplexity, pain, despair, and becoming hopeful again during the past five years in The Chinese University of Hong Kong (including my MPhil study), I should give my deepest appreciation to the kind people who stand around me with selfless supports, only to some of whom it is possible to give particular mention here.

First and foremost, I must offer my most profound thanks to my thesis advisor, Professor Jianfang Wang. Thanks to him, I had the unique opportunity to study here and therefore changed the rest of my life. I cannot imagine what my life would be like if I were not a PhD student here. I appreciate his expertise, understanding, and vast knowledge in many areas, providing insightful discussions about my research works. From finding an appropriate subject in the beginning to the thesis writing process, his words can always inspire me to "try again" and bring me to a higher level of thinking. Actually, he taught me gradually how to grow from an experimentalist to an independent thinker and even an instructor. He is my best role model for a scientist, supervisor, and teacher. I wish that I could be as enthusiastic, energetic, and fruitful as him in my future research career.

Special thanks also go to Professor Tao Chen for his scientific advice, knowledge, and valuable suggestions in the measurements and discussions of my work upon the application of (Au nanocrystal core)/(TiO_2 shell) nanostructures in dye-sensitized solar cells. I also would like to thank Professor Hongkai Wu from The Hong Kong University of Science and Technology for his kind help during my first two years in The Chinese University of Hong Kong. I also should give my thanks to my PhD

thesis committee members, Professor Xudong Xiao, Professor Jimmy C. Yu, and the external examiner Professor Zhi Yang for their helpful advices and suggestions and the time spent on my thesis.

I am indebted to my collaborators who helped me finish my researches. Dr. Lei Shao and Dr. Ruibing Jiang helped me a lot in performing finite-difference time-domain simulations. Dr. Yih Hong Lee taught me patiently how to prepare Ag nanocubes in high yields. Mr. Shuai Chang spent a lot of time in the measurements of solar cell performances. Mr. Henglei Jia helped me finish the work of (Au nanocrystal core)/(TiO$_2$ shell) nanostructures. All of them were busy with their own works, but they gave me their hands when I encountered difficulties.

The members of our group have contributed tremendously to my personal and research time. I gained cherish friendships from our group. I therefore would like to acknowledge our current group members, including Mr. Qifeng Ruan, Miss Qian Li, Mr. Feng Qin, Mr. Yuting Tao, Mr. Junxin Wang, Miss Tian Zhao, Ms. Nina Jiang, Mr. Shouren Zhang, Miss Xiaolu Zhuo, and Mr. Xingzhong Zhu. Special appreciation should be given to our previous group members. I will forever remember the happy time together with them.

In addition, I also want to say thanks to Mr. Andrew S. K. Lee, Mr. Man Hau Yeung, and all of the ladies in the general office for their kindness and warm help.

Lastly, I am deeply grateful to my family for their love and encouragement. My hard-working parents sacrificed their lives and did their best to provide me a comfortable environment. My brother and sisters spent a lot of time in caring my parents, allowing me to focus on my works. Most of all, I should deliver my thanks to my husband, Zhiqing Cui, who unconditionally supported me to finish this thesis study. These past years have not been an easy life for us. He always stands by me and has faith on me during my good or bad time. I am so happy to have all of them in my life.

Table of Contents

List of Figures

Chapter 1

Introduction

This thesis starts with a general overview on noble metal nanocrystals. At the outset, I will give a brief introduction in *Section 1.1* about localized surface plasmon that noble metal nanocrystals can support, the preparation of noble metal nanocrystals, and the applications of plasmonic nanocrystals. In *Section 1.2* I will talk about the applications of plasmonic nanocrystals in solar cells and photocatalysis that have attracted much attention in solar energy harvesting. I will further introduce metal/semiconductor hybrid nanostructures with special configurations, including their preparations, properties, and utilizations in solar energy harvesting, in *Section 1.3*. At the end of this chapter (*Section 1.4*), I will present a brief outline of this thesis.

1.1 Plasmonic Properties of Noble Metal Nanocrystals

Nowadays, nanoscience and nanotechnology have become an active theme of scientific investigation. Among various nanomaterials, noble metal nanocrystals, especially Au and Ag nanocrystals, have become a "hot topic" because of their unique optical, electronic, and catalytic properties, as well as their potential applications in many areas [1–3]. Their fascinating properties mostly arise from the localized surface plasmon resonance (LSPR) they can support, which are collective oscillations of free electrons in the metal conduction band, geometrically confined by the shape of the nanocrystal. I will first introduce the fundamental knowledge of the LSPR of noble metal nanocrystals in *Section 1.1.1*. Since the outstanding LSPR properties of noble metal nanocrystals can be synthetically tailored by tuning their shapes and sizes, I will briefly present the growth of noble metal nanocrystals in *Section 1.1.2*. At the end of

this part, I will give an overview about the applications of plasmonic metal nanocrystals.

1.1.1 Localized Surface Plasmon Resonance

When a metal nanoparticle is illuminated by an incident light, the oscillating electric field drives the free electrons in the conduction band to oscillate coherently. If the electron cloud moves away from the nuclei, a resorting force from the Coulombic attraction between the negatively charged electron cloud and the positively charged nuclei causes collective electron oscillations [4]. This process is illustrated in Figure 1.1, by taking a metallic nanosphere as an example. LSPR occurs when the frequency of the incident light matches the inherent frequency of the collective oscillation of the free electrons in the conduction band. Under the resonant condition, the oscillation strength reaches maximum. Both the light absorption and scattering are significantly enhanced under the light illumination at the resonance wavelength, making noble metal nanocrystals exhibit rich colors. Colloidal noble metals can therefore be used to make ruby glass and decorate windows in ancient times. Lycurgus Cup, a most representative example, was manufactured in the 5th to 4th century A. D. by incorporating Au particles into glass. It appears red in transmitted light and turns to green in reflected light because of the presence of Au nanoparticles in the cup. Besides noble metal nanostructures, other materials, such as semiconductor sulfides and oxides, also possess LSPR when their charge carrier concentrations are high enough [5–8].
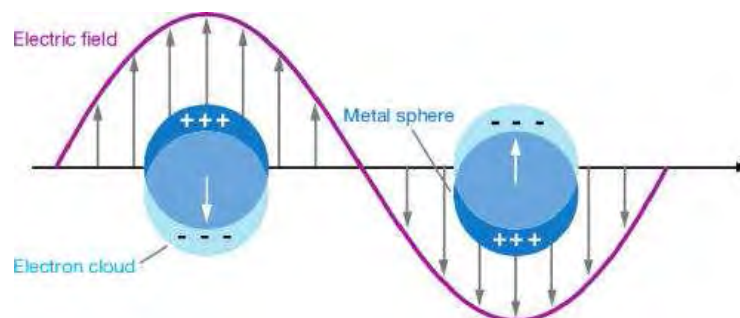
Figure 1.1 Schematic illustrating the displacement of the free electrons in the conduction band of a spherical metal nanoparticle relative to the nuclei. This figure comes from internet.

LSPR endows plasmonic metal nanostructures with very large absorption and scattering cross-sections at their plasmon resonance wavelength. Figure 1.2a and b display the comparison of the optical cross-sections of plasmonic metal nanocrystals with other optical species, including atoms/ions, organic fluorophores, and semiconductor quantum dots [9,10]. All of them show strong light responses. Both the absorption and scattering cross-sections of the optical species decrease with decreasing sizes, but the scattering cross-sections decrease more quickly than the absorption cross-sections. Therefore, the absorption cross-sections are orders of magnitude larger than the scattering cross-sections for atoms/ions, organic dyes, and semiconductor quantum dots. For plasmonic metal nanocrystals, both absorption and scattering are important. Moreover, plasmonic metal nanocrystals have their optical cross-sections larger than their physical cross-sections. A larger absorption or scattering cross-section means a higher probability of light being absorbed or scattered. Plasmonic metal nanocrystals therefore give higher light absorption or scattering properties compared to other optical species.
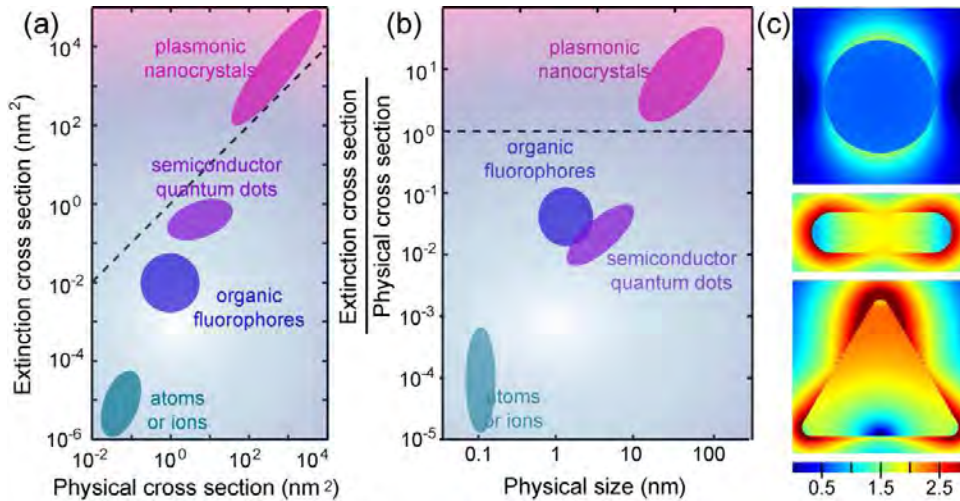
Figure 1.2 Extinction cross-sections of optical species and electric field contours around Au nanocrystals. (a) Extinction cross-sections of various optical species *versus* their physical cross-sections [9]. (b) Ratios between the extinction and physical cross-sections *versus* their physical sizes [9]. (c) Electric field contours around a Au nanosphere, nanorod, and nanotriangle nanocrystal with the same volume from top to bottom, respectively. The diameter of the Au nanosphere is 50 nm. The nanorod has a diameter and length of 30 nm and 102 nm, respectively. The Au nanotriangle is an equilateral triangle with an edge length of 87 nm and a thickness of 10 nm [10].

Under resonant excitation, the LSPR of a noble metal nanocrystal can strongly concentrate incident light in a small volume surrounding the nanocrystal. The field intensity is maximal at the metal surface and decays approximately exponentially away from the metal surface. The field intensity can be further enhanced by increasing the curvature of the metal nanocrystal [11,12]. Generally, the sharper a plasmonic metal nanocrystal is, the higher enhancement the electric field exhibits. Figure 1.2c shows the electric filed distribution contours of differently shaped Au nanocrystals, taking a Au nanosphere, nanorod, and triangle with the same volume as example, obtained from finite-difference time-domain simulations [10]. The electric field enhancement at the surface of an isolated nanoparticle ranges from ~50 to 10^3, depending on the size and shape [10]. Besides, the field intensity can be enhanced to even higher than 10^6 between two Au nanorods separated by ~1 nm [13,14]. Surface

plasmon resonance decays mainly through either a radiative scattering of resonant photons on large plasmonic nanocrystals, or the formation of energetic charge carriers in small particles [15,16]. The energetic charge carriers can relax to locally heat the nanocrystal or transfer their energy to the surrounding medium, which can improve the performance of the nearby nanomaterials, for example, semiconductors for solar energy harvesting. I will discuss plasmon-enhanced solar energy harvesting including their mechanisms and applications in detail in *Section 1.2*.

1.1.2 Noble Metal Nanocrystals

The LSPR properties of plasmonic metal nanostructures highly depend on their compositions, sizes, shapes, and surrounding environment [17]. The ability to control these parameters therefore enables one to control their plasmonic properties. Consequently, preparing plasmonic nanostructures with well-defined shapes and well-controlled sizes, which I will focus on in this section, greatly facilitates our study of the plasmonic behaviors of such nanostructures (*Section 1.1.1.*). In general, there are two preparation strategies, "top-down" and "bottom-up" methods. Using "top-down", "bottom-up", or hybrid methods that combine the virtues of both, high-quality noble metal nanocrystals with a wide variety of shapes and sizes have been prepared. A vast range of methods have been developed and are continuing to be developed. I do not attempt to give a comprehensive introduction of all methods in this thesis. Instead, I will first present a general overview on "top-down" methods. Then I would like to focus on the "bottom-up" methods by taking the growth of Ag nanocubes and Au nanorods as examples.

"Top-down" methods mean that bulk metal is "cut" into small particles at the nanoscale. Although many different "top-down" methods have been developed to fabricate metal nanostructures, they mainly follow the general strategy of pattern transfer. A pre-designed pattern is fabricated on a substrate, which is then replicated to a thin metal film on the substrate. Two separate steps are involved in this process,

which are a lithography step to produce the pattern, and a transfer process to replicate the pattern in the metal film [21]. Commonly used "top-down" methods are photolithography and electron beam lithography. Owing to the diffraction limit of light, metal nanostructures produced by photolithography are limited in the range of several hundred nanometers. On the other hand, electron beam lithography can produce metal nanostructures with sizes ranging from ~10 nm to several hundred nanometers. Nowadays, "top-down" methods have mainly been applied for the preparation of metal nanostructures with complex morphologies in two dimensions. However, these methods usually require costly equipments and are time-consuming. In addition, metal nanostructures with well-defined three-dimensional geometries are hard to be fabricated using "top-down" methods [22–24]. More importantly, plasmonic metal nanostructures obtained from "top-down" methods are usually polycrystalline, which can degrade their plasmonic properties owing to the additional loss mechanism of localized plasmon resonance caused by electron scattering at the grain boundaries [25]. These shortcomings limit the applications of "top-down" methods both in practical applications and fundamental research.

"Bottom-up" methods are built on the techniques of chemical synthesis or assembly. They start with atoms, ions, or molecules. Typical "bottom-up" methods for the fabrication of plasmonic metal nanostructures include wet-chemical, microwave-assisted, sonochemical, solvothermal, electrochemical, and photochemical reduction methods. Variously shaped nanostructures have been grown using these strategies, such as nanorods, nanocubes, nanooctahedra, nanostars, nanosheets, and porous nanoparticles [26]. Here, I will focus on the growth of Ag nanocrystals via a polyol process and Au nanocrystals via a seed-mediated method, which played an irreplaceable role during my PhD study.
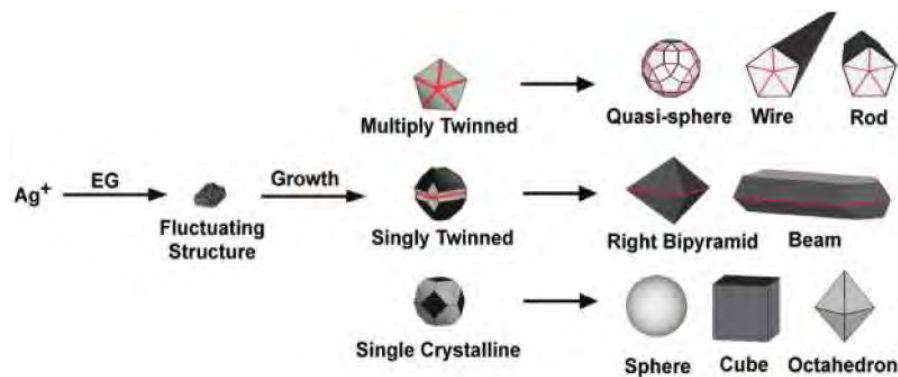
Figure 1.3 A polyol method for the synthesis of Ag nanocrystals with various morphologies. The reducing agent employed in this figure is ethylene glycol [26].

The polyol process is a robust and versatile approach for growing various Ag nanocrystals at different reaction conditions [27–29]. The reaction conditions that can be varied during the preparation process include the reaction temperature, the concentration of reagents, and the presence of trace ions. A polyol, such as ethylene glycol, 1,2-propylene, or 1,5-pentanediol, servers as both a reducing agent and a solvent in a typical synthesis process [30,31]. $AgNO_3$ and CF_3COOAg are the two mostly used silver sources while poly (vinyl pyrrolidone) is the commonly used stabilizer. Generally, a stabilizer and a Ag precursor are injected into a preheated polyol solvent (140–160 °C). The reduction of the Ag precursor results in the nucleation and growth of the nanostructures. Figure 1.3 displays Ag nanostructures synthesized using the polyol process. Typically, the reduction of Ag^+ by polyol forms nuclei with fluctuating structures. As the nuclei grow larger, the seeds form three predominant types of structures (twinned, singly-twinned, and single-crystalline), which grow into different morphologies under different reaction conditions [26]. It should be pointed out that oxidative etching is also an effective way to control the final shape of Ag nanocrystals, because the seeds, especially for singly-twinned and multiply-twined seeds, are sensitive to oxidative etching owing to the presence of defects.   Oxidative etching is typically realized by adding trace ions, such as Cl^- or Br^-. When an oxidative etching agent is introduced and combined with oxygen from air, the etching will influence the relative proportions of different seeds, causing the

formation of a variety of Ag nanostructures. For example, when a weaker ligand Br$^-$ is introduced, the combination of Br$^-$ and O$_2$ only dissolves multiply-twinned seeds by oxidative etching, resulting in a right bipyramid shape [32]. However, when Cl$^-$, a stronger ligand, is introduced, the joint action of Cl$^-$ and O$_2$ dissolves both singly-twinned and multiply-twinned seeds, leading to the production of Ag nanocubes [33].
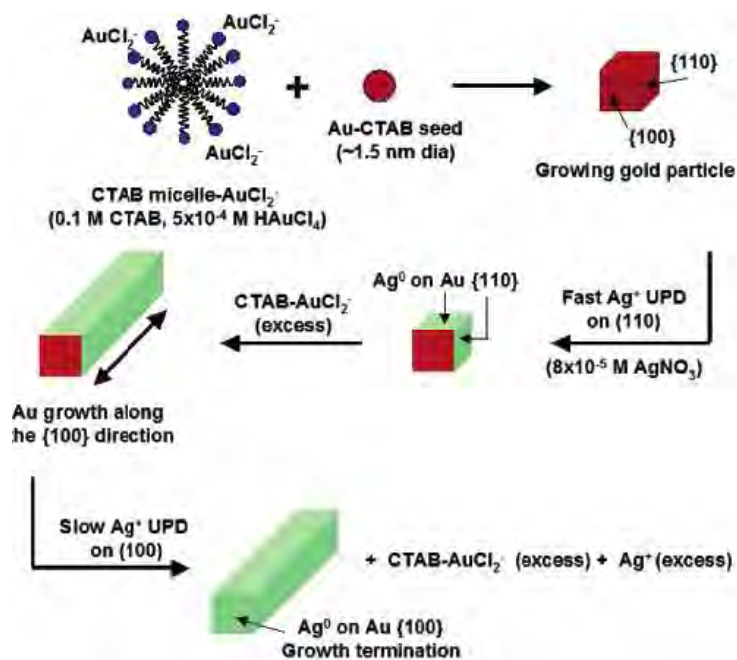
Figure 1.4 Mechanism of Au nanorod growth from Au seeds in the presence of Ag$^+$. The nanorod growth is realized in the presence of CTAB [37].

Researchers have developed many approaches for the growth of Au nanocrystals in solutions in the presence of various surfactants. Surfactants not only serve as stabilizers to prevent aggregation of Au nanostructures, but also function as "soft templates" that can direct the growth of Au nanocrystals. The seed-mediated growth is the most commonly used method for growing Au nanocrystals. Generally, the seed-mediated method can be realized in two steps. In the first step, the seeds with a diameter of ~1.5 nm are prepared by reducing chloroauric acid in the presence of a stabilizer. In the second step, the seeds are injected into the growth solution that is formed by reducing Au(III) complex ions into Au(I) complex ions using a mild

reducing agent. The added seeds thereafter catalyze the further reduction of Au(I) complex ions to Au (0), which is deposited on the surface of the seeds, leading to the growth of Au nanocrystals. By carefully changing the nature of the surfactant, the pH value of the growth solution, and the seed structure, Au nanocrystals with different shapes, such as nanorods, nanospheres, nanocubes, and nanopolyhedra, can be fabricated [34]. In the growth process of Au nanorods, Murphy and co-workers found that $AgNO_3$ played a favorable role in the control growth of Au nanorods [35]. They further improved the yield of Au nanorods up to 99% by using cetyltrimethylammonium bromide (CTAB) as the surfactant in the seed preparation and in the growth solution [36]. The growth mechanism in the presence of Ag^+, which was proposed by Murphy *et al.* [37], is illustrated in Figure 1.4 on the basis of an electric field-directed growth mechanism [38]. In the growth solution, $AuCl_4^-$ is first bound with CTAB micelles, which are then reduced to Au^+, forming $AuCl_2^-$–CTAB micelles. After the seed solution is added, Ag^+ is believed to selectively bind with the {110} facets of Au nanocrystals and slow down the growth rate of these facets. As a result, reduced Au atoms will be predominately deposited onto the {100} facets, giving a faster grown rate on the {100} facets than that on the {110} facets. The different growth rates will break the structural symmetry, leading to the formation of the nanorod morphology.

1.1.3 Applications of Noble Metal Nanocrystals supporting Localized Surface Plasmon Resonance

Noble metal nanostructures have been widely used in many areas. The remarkably enhanced electric field in the vicinity of their surface enables the utilization in the amplification of various optical signals. On the other hand, LSPR endows noble metal nanocrystals with large absorption and scattering cross-sections. Plasmonic noble metal nanoparticles can therefore be used in photothermal conversion-based therapy, biological labeling and imaging, and light harvesting applications. Moreover,

plasmonic properties, such as plasmon resonance wavelengths, are very sensitive to the surrounding environment, thus making plasmonic metal nanocrystals excellent candidates as biological molecular and ionic sensors.

1.1.3.1 Plasmonic modulation of optical signals

When plasmonic metal nanocrystals are integrated with optical species, such as organic fluorophores or semiconductor quantum dots, the electromagnetic field enhancement allows for effective amplification of optical signals. Figure 1.5a illustrates the process of plasmon-enabled optical magnification [39]. The optical species placed adjacent to a metal nanocrystal essentially feel an enhanced excitation light intensity because of the strengthened electromagnetic field due to plasmon resonance. Therefore, the light absorption of the optical component is increased, and the light-emission is modulated. A variety of optical signals, including Raman scattering [41,42], high-harmonic generation [43,44], circular dichroism [45,46], fluorescence [47,48], and two-photon photoluminescence [49,50], have been reported to be amplified. Among them, surface enhanced Raman scattering (SERS) is regarded as an important application of noble metal nanostructures. The SERS mechanism involves mainly the electromagnetic field enhancement and the chemical enhancement [51–53]. Since the Raman intensity is approximately proportional to the forth power of the electromagnetic field, the signal can be amplified significantly when probe molecules are placed in the vicinity of plasmonic nanostructures. El-Sayed *et al.* reported that the Raman enhancement factor reached 10^4–10^5 when Raman-active molecules were absorbed on Au nanorods because of the strong field enhancements at the ends of Au nanorods [54]. The enhancement can be further increased by self-assembly of Au nanocrystals. The gap region between two nanocrystals, so-called "hot spot", provides extremely large field enhancements and therefore unprecedented SERS signals can be obtained from Raman molecules located in these "hot spots" (Figure 1.5b). Thomas and co-workers demonstrated that the enhancement factor of Raman signals can increase to ~1.4×10^5 due to the localization

of molecules in the "hot spots" of the dimmers and can be enhanced even higher by oligomers with more aligned Au nanorods [55]. Similar to SERS, fluorescence intensity can also be strongly amplified by the "hot spots" near colloidal metal nanoparticles or the gap regions between nanostructures [56,57]. Enhancement factors up to ~1340 for single-molecule fluorescence has been found in carefully designed bowtie nanoantennas [47].
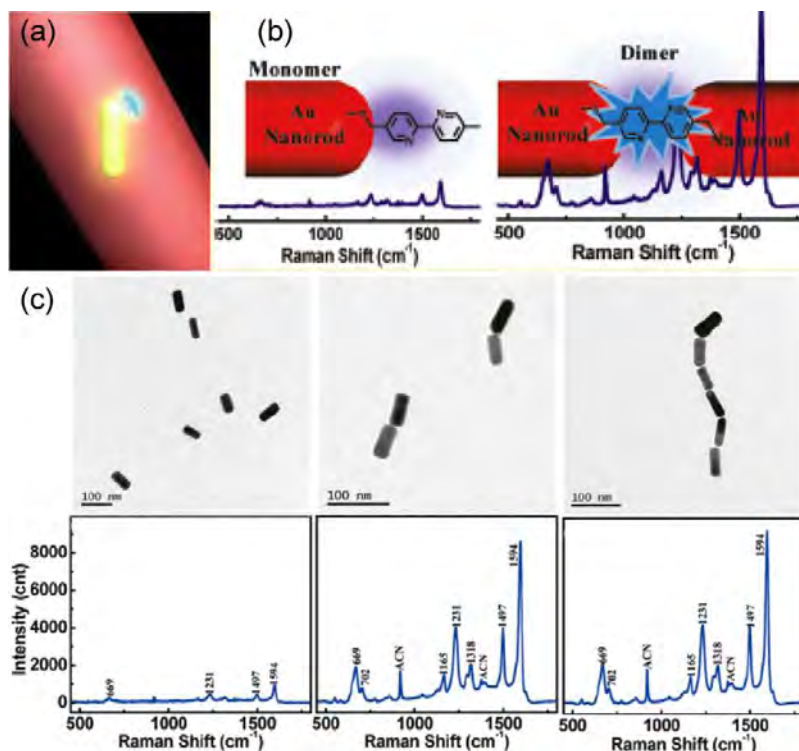
Figure 1.5 Plasmonic modulation of optical signals. (a) Schematic showing the plasmonic enhancement of optical signals from a molecular species that is locatednear a Au nanorod [39]. (b) SERS from a single Au nanorod (right) and a Au nanorod dimer (left) [55]. (c) TEM images (top) and corresponding Raman spectra (bottom) of a single nanorod, a Au nanorod dimer, and a Au oligomer, respectively [55].

1.1.3.2 Biological sciences

The applications of plasmonic metal nanostructures in biological and medical areas are extensively broad, including biosensors, clinical chemistry, detection and photothermolysis of cancer cells and microorganisms, targeted delivery of drug and

genes, bioimaging and monitoring of cells or issues [58]. In particular, Au nanorods have been used in diagnostics and therapy in biological applications. Such wide applications are based on the distinct physical and chemical properties of noble metal nanostructures. First, they provide high surface-to-volume ratios. Second, the plasmon resonance wavelengths can be tailored over a wide range from the visible to near-infrared region by synthetically varying their compositions, sizes, and shapes. Therefore, they are feasible for medical diagnosis or therapy with different excitation wavelengths in the range of the transparency window, where biological tissues only slightly absorb light [34].

LSPR endows noble metal nanocrystals with large scattering cross-sections as described in the previous section, making them excellent candidates for biological labeling and imaging based on optical recording. Furthermore, noble metal nanocrystals do not suffer from photobleaching, which is a severe problem for conventional dye molecules. As demonstrated by El-Sayed *et al.*, anti-EGFR conjugated Au nanocrystals can bond selectively to malignant cancerous HOC cells [59]. Such malignant cells thus show a distinguishable imaging contrast, which is distinctly different from noncancerous cells under dark-field scattering imaging (Figure 1.6a). For noncancerous cells, it is hard to distinguish due to the nonselective interactions between the nanostructures and the cells (Figure 1.6b). With plasmonic metal nanoparticles, it is possible to "map out" malignant cells on the basis of their scattering images as proved by many research results [60,61].

Plasmonic metal nanocrystals with large absorption cross-sections possess excellent photothermal effect. The nonradiative decay of excited surface plasmon transfers the energy of absorbed photons into metal lattice vibrations, which in turn results in a localized temperature increase. Under the resonant excitation, nanostructures show high photothermal conversion efficiencies. Because of this feature, plasmonic nanoparticles have been extensively employed in photothermal therapy and control of drug delivery. After Au nanoparticles were first used in

photothermal therapy, which is referred to plasmonic photothermal therapy, in 2003 [62], plasmonic photothermal therapy has been used in *vivo*. Sailor and co-workers found that poly(ethylene glycol)-modified Au nanorods can accumulate in xenograft tumor in mice (Figure 1.6c). Effective photothermal treatment *in vivo* of this tumor was achieved by the illumination with a NIR laser for only 10 min [63]. As a particularly promising property, plasmonic photothermal conversion has also been applied to control drug delivery. Figure 1.6d illustrates schematically photothermal drug delivery. Drug molecules are incorporated into mesoporous SiO_2 shells [64]. Under the excitation with a NIR laser, the local temperature rise leads to the dehybridization of the drug that is anchored on the SiO_2 surface, allowing for remotely controlled drug delivery.
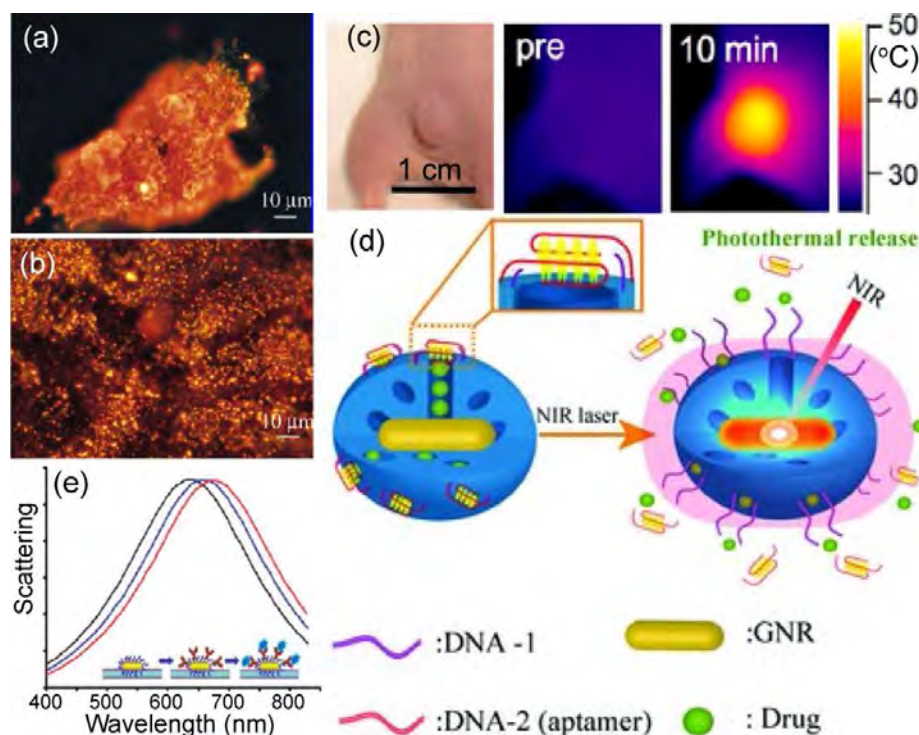
Figure 1.6 Plasmon in biological sciences. (a,b) Optical dark-field scattering image of cancerous HOC and normal HaCaT cells incubated with anti-EGFR conjugated Au nanorods, respectively [59]. (c) Photothermal treatment *in vivo*. Infrared thermographic maps of the tumor region in a mouse, showing the temperature distributions obtained before and after the laser illumination for 10 min [63]. (d)

Illustration for NIR light-driven drug release of gust molecules from the pores of aptamer-covered nanovehicles [64]. (e) Schematic describing the principle of plasmonic biological sensors [66].

Noble metal nanocrystals have been explored as plasmonic biological sensors. The adsorption of biological molecules on the surface of noble metal nanocrystals changes the refractive index of the surrounding environment and induces a shift of the plasmon resonance wavelength. For example, to monitor biomolecules, Au nanorods are modified with a self-assembled monolayer of antibodies [65]. Secondary antibody molecules are monitored by measuring the plasmon peak shifts because of the reactions between the two types of antibody molecules, as shown in Figure 1.6e. A recent study showed a sensing limit of prostate antigens to be as low as attomolar using single Au nanorods [66]. Plasmonic sensing can also be extended to the detection of threatening species in our daily life, such as metal ions or nitrites [67–69].

1.1.3.3 Plasmon-enhanced light harvesting applications

Plasmonic metal nanostructures have been found to play important roles in light harvesting applications, including photochemical reactions and solar cells. A variety of photochemical reactions ranging from organic synthesis, photodegradation of organic pollutants in the environment, to photo-driven water splitting has been improved by utilizing noble metal nanocrystals [70–72]. Both pure plasmonic nanostructures and hybrids between noble metal nanoparticles and semiconductors can be employed to enhance the reaction rate and the chemical selectivity. The LSPR enhancements under resonant excitation can improve the light absorption and therefore the generation of electron–hole pairs in nearby semiconductors. Moreover, the photothermal conversion of plasmonic nanostructures results in a temperature increase, leading to a higher reaction rate. In addition, "hot electrons" gaining energy form plasmon decay can be excited under resonant illumination, which thereafter take

part in catalytic reactions. In solar cells, plasmonic nanoparticles are introduced to increase the light absorption. I will discuss the detailed mechanisms and typical applications in light harvesting applications in the following section (*Section 1.2*).

1.2 Plasmonic Solar Energy Harvesting and Applications

Energy is a vital issue for human society. Development of renewable, highly efficient, and green energies has therefore become a global topic in research and practical applications. Among various candidates, such as hydroelectric, wind, nuclear, and geothermal energy, solar energy is the most promising source. It is estimated that approximate 89000 TW of solar energy strikes the earth's surface. It is much larger than the average consumption rate during a year on the earth (~15 TW in 2012 reported from International Energy Agency). Harvesting solar energy is therefore an appealing option for solving energy crisis. In this section, I will give an introduction about solar harvesting approaches, focusing on plasmon-enhanced solar cells and photocatalysis. I will introduce plasmon-enhanced mechanisms in *Section 1.2.1*, plasmon-enhanced solar cells in *Section 1.2.2*, and plasmon-enhanced photocatalysis in *Section 1.2.3*. I should point out that plasmonic metal nanocrystals have been hybridized with photocatalytic nanomaterials in various manners, including chemical or physical deposition, attachment of pre-grown metal nanocrystals, and preparation of nanostructures with special configurations. In this section, plasmon-enhanced light harvesting applications are focused on the previous two ways in which plasmonic metal-decorated semiconductor nanostructures are prepared. The applications of the nanostructures with special configurations, such as core/shell, eccentric and york/shell, and Janus nanostructures, will be discussed in next section in this thesis (*Section 1.3*).

1.2.1 Mechanisms

To introduce the light harvesting applications in solar cells and photocatalysis, I

would like to discuss the plasmon-enhanced mechanisms that are proposed in recent studies. These mechanisms are applicable for all of the structures that hybridize plasmonic metal nanocrystals with semiconductors.

In a comprehensive review paper, three plasmon-enhanced mechanisms in solar cells were proposed, including light scattering enhancement, near-field enhancement, and surface plasmon polaritons [73]. Herein, I will focus on the light scattering enhancement and near-field enhancement related to the use of metal nanostructures. For the two mechanisms, metal nanostructures are positioned at different locations of a solar cell. On the one hand, metal nanostructures are placed on the top of a solar cell, where metal nanostructures can serve as subwavelength scattering elements due to their larger scattering cross-sections under resonant illumination. The incident light is scattered by the plasmonic metal nanostructures. Moreover, light scattered at an angle beyond the critical angle for total internal reflection will be trapped into the cell. As a result, the incident light can pass through the absorber layer several times, increasing the effective optical path length (Figure 1.7a). On the other hand, plasmonic metal nanostructures can also be embedded into the semiconductor absorber layer. The near-field enhancement around these metal nanostructures can couple to nearby semiconductors (Figure 1.7b). The effective absorption cross-sections of the semiconductors are thus increased, leading to the increase in charge carrier generation. These two light-trapping strategies allow for great decreases in the thickness of solar cells, while keeping or even increasing the power conversion efficiency of the solar cells. The contribution of each mechanism is dependent on the size of plasmonic metal nanostructures, the nature of semiconductor absorbers, and the structure of the solar cells [74].
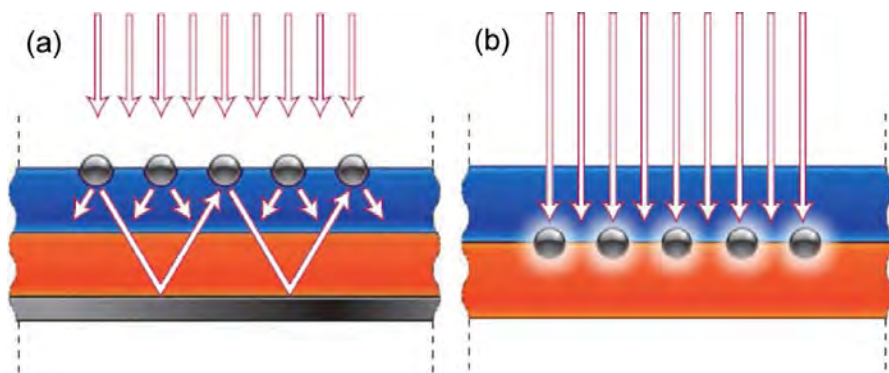
Figure 1.7 Schematics of plasmonic light trapping in thin-film solar cells. (a) Light trapping by scattering incident light from plasmonic metal nanostructures. Incident light is scattered and trapped into the absorber layer by multiple and high-angle scattering, resulting in the increase of the effective optical path in cells [73]. (b) Light trapping by excitation of the LSPR in plasmonic nanostructures that are embedded into the absorber layer. The field enhancement of plasmonic nanostructures can improve the light absorption ability of the light absorber [73].

Plasmon-enhanced photocatalytic reactions can generally be divided into two groups in accordance to the type of catalysts [39]. One group is based on hybrids between plasmonic metal nanocrystals with photocatalytically active semiconductors. Charge-separation effect and plasmonic effect are proposed in the enhancement of photocatalytic performances in these hybrids. For a semiconductor photocatalyst, an absorbed photon excites an electron from the valence band to the conduction band, creating an electron–hole pair which can take part in chemical reactions after they are separated. When a metal nanocrystal is in contact with a semiconductor, the photon-induced electrons in the semiconductor can transfer to the metal nanocrystal, because the Femi levels of noble metals are usually lower than the conduction band edges of common semiconductors (Figure 1.8a). This is the charge-separation effect. In this case, the metal cocatalyst acts as an electron sink. It has been well-studied and will not be described in detail in this thesis [75–78]. I will instead focus on the plasmonic effect, including light absorption enhancement and hot electron effect. The other mechanism is direct catalysis by pure plasmonic noble metals under resonant

excitation. I will also discuss its underlying principle in detail.

As mentioned in *Section 1.1.1*, LSPR endows plasmonic nanocrystals with strong localized field enhancement near the metal surface. The large electromagnetic field can enhance light absorption of semiconductors if their absorption spectra can overlap with the LSPR of metal nanocrystals. In these hybrids, the illumination light with an appropriate wavelength simultaneously excites the electron–hole pairs in semiconductors and the plasmon resonance in metal nanocrystals. The part of the semiconductor close to the plasmonic metal nanocrystal is therefore subjected to a stronger electromagnetic field (Figure 1.8b), whose intensity is several orders higher than that of the far-field illumination light. The concentration of the electron–hole pairs generated in this part is therefore remarkably increased, because the charge carrier generation rate is proportional to the electromagnetic field intensity [79]. The plasmon-enhanced localized electromagnetic field decays nearly exponentially away from the metal surface and extends up to 10 nm to 50 nm, which is dependent on the sizes and shapes of metal nanocrystals [9,73]. Therefore, the generation rate of electron–hole pairs can be increased within this spacing range. In this case, plasmonic metal nanocrystals serve as light processers. They can concentrate light energy and transfer it to nearby semiconductors. In addition, larger scattering cross-sections of plasmonic metals owing to LSPR also contribute to the increase of light absorption in photocatalytic reactions. The effective optical path length in catalysts is increased because of the multiple scattering of incident light, which is quite similar to the light trapping mechanism described previously in solar cells [73]. To maximize the plasmon-enhanced light absorption in semiconductors, perfect spectral overlap among the LSPR of metal nanocrystals, the absorption of semiconductors, and the wavelength of the incident light is highly desired. The spatial geometry arrangement of metal nanocrystals and semiconductors is also important, because the field enhancement caused by plasmon resonance is strongly dependent on the sizes and shapes of metal nanocrystals and the spacing away from the metal surface.
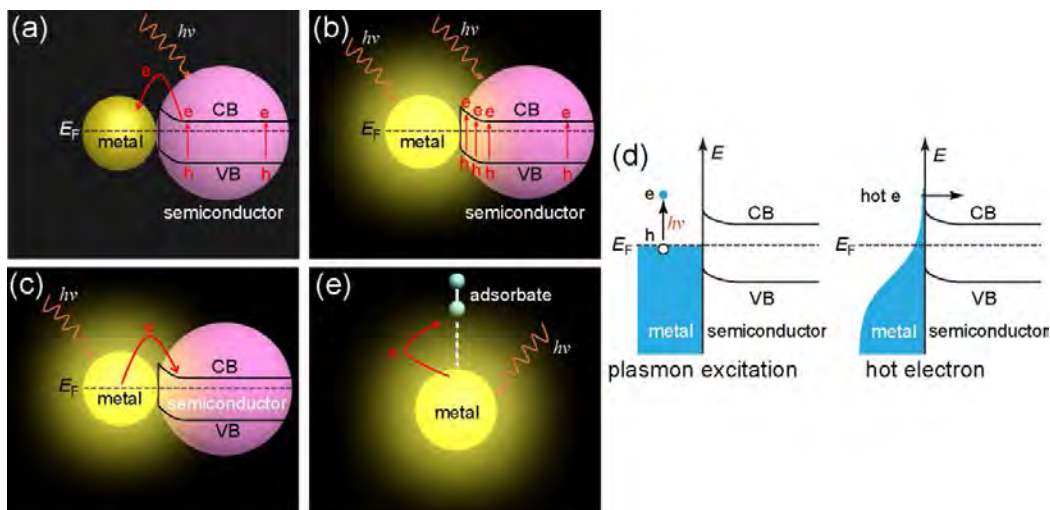
Figure 1.8 Schematics describing the charge-separation and plasmonic effects for photocatalytic reactions. (a) Charge-separation process. (b) Plasmon-enhanced light absorption [10]. (c) Hot-electron effect [10]. (d) Process of the hot-electron effect [10]. (e) Pure metal plasmonic photocatalysis. CB and VB refer to the conduction band and valence band of the semiconductor photocatalyst, respectively. E_F represents the Fermi energy level.

Another plasmonic mechanism is known as plasmonic sensitization. The excited electrons in metal nanocrystals under resonant illumination transfer to the conduction band of wide-band-gap semiconductors (Figure 1.8c). Most semiconductors employed in photocatalytic reactions are n-type. When they are in contact with metal nanocrystals, a Schottky barrier is formed. This potential barrier blocks the electron transfer from metal nanocrystals to semiconductors. However, a population of energetic electrons will be generated under resonant excitation. These energetic electrons are called "hot electrons". The "hot electron" process is shown in Figure 1.8d. Under excitation, each plasmon decays either radiatively into a photon or non-radiatively into an electron–hole pair [80]. For metal nanocrystals small enough for subradiant plasmon modes, the dominant decay manner is electron–hole pair generation. The most probable electron–hole pair generation occurs when the excited plasmon causes an electron from the Fermi level of metal nanocrystals to an unoccupied state below the vacuum level (Figure 1.8d, left side). The excited hot

electrons will quickly lose coherence and form a non-equilibrium Fermi-Dirac-type distribution through random thermalization by Auger scattering (Figure 1.8d, right side). The plasmon-induced hot electrons in metal nanocrystals with energy higher than the Schottky barrier have the probability to overcome the barrier and inject to the conduction band of semiconductors. The probability of electron transfer is dependent on the barrier height and the energy of the hot electrons. Because of plasmonic sensitization, the wide-band-gap semiconductor, which is initially photocatalytic inactive in visible light, accepts the excited electrons and therefore exhibits visible light photocatalysis. The extra electrons in the conduction band of the semiconductor can perform catalytic reduction reactions [81,82]. The holes left in the metal have a mild oxidative ability, which can be employed in chemoseletive oxidation of organic compounds [70,83].

Pure plasmonic nanocrystals can also be used as photocatalysts in chemical reactions. Under resonant excitation, plasmonic metal nanocrystals are able to increase the catalytic reaction rate. This enhancement mechanism is proposed to result from "hot electrons" and photothermal heating. The former is an electron transfer process (Figure 1.8e). Similar to plasmonic sensitization, hot electrons induced by resonant excitation of metal nanocrystals inject to the lowest unoccupied molecular orbital [17,39,84,85]. The injection leads to the weakening and stretching of the original chemical bond of adsorbates and transient anions form. The transient anions subsequently decay and transfer back the injected electron into the metal nanocrystal, which results in the deposition of energy into the molecular vibrational mode. If the deposited energy is high enough to overcome the activation barrier that is required for the dissociation of the adsorbate, a chemical reaction can then take place [17,84]. Besides, a reaction system can be heated because of the photothermal effect. Temperature increases change the reaction rate according to Arrhenius equation. The temperature increase is dependent on several parameters, including the concentration and plasmon resonance wavelength of plasmonic photocatalysts, the wavelength and intensity of the illumination photons, and the surrounding environment. The

photothermal effect should be taken into account when plasmonic photocatalysts with a high concentration is illuminated at the plasmon resonance wavelength.

1.2.2 Plasmon-Enhanced Solar Cells

Solar cell, converting sunlight into electricity, is an encouraging technology that can allow large scale electric generation. Worldwide photovoltaic production reached 5 GW in 2008, and is expected to increase to 20 GW in 2015. Currently, 90% of the solar cells in market is made of crystalline silicon wafer. Silicon solar cells always possess a thickness at the range of 180–300 μm because the absorber must be "optically thick" to allow for near-complete light absorption and be physically thin to facilitate photocarrier current collection [73]. The expensive material and fabrication process of crystalline silicon make solar cells expensive. It is therefore of great interest to design thin-film solar cells using special absorbers or structures with a thickness of about 1–2 μm. A major limitation is that their light absorption is ineffective in thin-film solar cells. Therefore, designing solar cells that can trap light inside them to increase light absorption is highly desired. Light trapping is achieved by a pyramidal surface texture in conventional thick silicon solar cells [86,87]. Such configuration is not suitable for thin film solar cells for geometrical reasons and the larger surface areas increase minority carrier recombination in the surface and junction [73]. As an alternative way, plasmonic metal nanostructures are used to enhance light absorption in thin film solar cells.
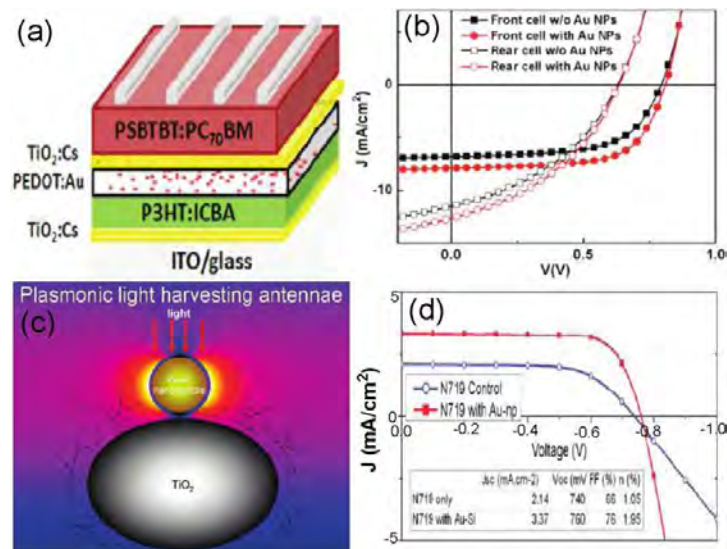
Figure 1.9 Plasmon-enhanced thin-film solar cells. (a) Schematic of a plasmonic tandem solar cell [102]. (b) Current density–voltage curves of the tandem solar cells with or without Au nanocrystals [102]. (c) Schematic showing the plasmon-enhanced effect in dye-sensitized solar cells [106]. (d) Current–voltage characteristics of the dye-sensitized solar cells with the thickness of 1.1 μm with or without Au@SiO$_2$ nanostructures in the active layer [106].

The light scattering enhancement in solar cells by metal nanostructures was first recognized by Stuart and Hall [88,89]. They observed a noticeable increase in the photocurrent density by employing metal islands in solar cells. This research area then remained almost dormant for several years, until the appearance of thin-film solar cells. Recently, plasmonic metal nanostructures have been incorporated into thin-film photovoltaic devices, such as organic photovoltaic systems [90,91] and dye-sensitized solar cells [92,93]. For organic solar cells, the power conversion efficiency has been improved by 15–70% through incorporating active metal nanostructures [94–99]. The efficiency of organic photovoltaic cells has been enhanced by a factor of 1.7 [100,101]. A high enhancement factor of 3 has been achieved for charge generation in organic photovoltaic devices by introducing Ag nanoprisms [90]. Similarly, Au nanostructures have been embedded into the interconnecting layer that connects two subcells in an inverted tandem polymer solar cell (Figure 1.9a) [102]. The

plasmon-enhanced absorption leads to an improvement in the efficiency of both the top and bottom subcells. As a result, a 20% enhancement of the power conversion efficiency is obtained (Figure 1.9b). The plasmon-enhanced effect has also been investigated in dye-sensitized solar cells, in which inorganic semiconductors are sensitized with dye molecules. Researchers first mixed bare metallic structures into dye-sensitized solar cells to advance their performances [103–106]. However, bare metal nanostructures cause the recombination and back reaction of charge carriers and corrosion of metals by electrolytes. Recently, an insulating SiO_2 has been used to protect metal nanostructures [107,108]. In particular, Snaith and co-workers systematically investigated plasmon-enhanced dye-sensitized solar cells by incorporation Au@SiO_2 nanostructures (Figure 1.9c) [106]. The power conversion efficiency is increased by almost 53% (Figure 1.9d). The performance of the cells keeps unaltered after aging for more than 1 month, indicating that the coating of SiO_2 can inhibit corrosion from electrolytes. However, the insulating layer should be very thin. The best thickness is 3 nm. No significant enhancement was detected in the performance of solar cells with the shell thickness up to 8 nm. To date, it is very difficult to prepare such thin silica shells on metal cores. Moreover, parts of the photon-induced charge carriers generated by dye molecules adsorbed on SiO_2 surface are lost due to the difficulty in the injection of charge carriers into insulting SiO_2 [109]. Specially structured plasmonic metal/semiconductors, which I will introduce in *Section 1.3*, are therefore an appealing candidate in the application of dye-sensitized solar cells.

1.2.3 Plasmon-Enhanced Photocatalysis

Photocatalysis is a potentially useful route to achieve solar energy harvesting. The solar energy can be stored in chemical bonds that can be released later in practical applications. However, its efficiency and selectivity is too low to allow for practical large scale applications. In the past several decades, many methods have been

developed for improving the photocatalytic performance, including the plasmon-enhanced strategy [76]. In this section, I will discuss three major plasmon-enhanced photocatalytic reactions, including photodegradation for environmental cleaning, synthesis of organic molecules, and water splitting.

1.2.3.1 Photodegradation for environmental cleaning

Photodegradation of organic pollutants assisted by photocatalysts is an effective and cheap way for achieving environmental cleaning. In photodegradation, photon-induced holes and electrons react respectively with H_2O and adsorbed O_2 to generate hydroxyl radicals. The reactions are shown as following [110]:

$$H_2O + h^+ \rightarrow \cdot OH + H^+$$

$$O_2 + e^- \rightarrow O_2^{-\bullet}$$

$$O_2^{-\bullet} + H^+ \rightarrow \cdot OOH$$

$$\cdot OOH + e^- + H^+ \rightarrow H_2O_2$$

$$H_2O_2 + e^- \rightarrow \cdot OH + OH^-$$
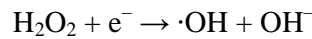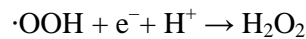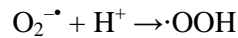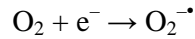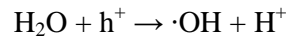
Hydroxyl radicals can break down organic pollutants into clean small molecules such as CO_2, NH_3, and H_2O. However, conventional semiconductor photocatalysts exhibit poor catalytic performance in the visible region because of their wide bandgaps and high electron–hole recombination rates. Integration with noble metal nanocrystals can overcome these limits through the mechanisms described in *Section 1.2.1*. The photocatalytic performance can therefore be greatly improved. A vast of works have been reported in recent years (Figure 1.10) [39,111,112]. Ong *et al.* reported the use of Ag nanocrystals to increase the light absorption in the visible region and enhance electron–hole separation in TiO_2. As a result, the photocatalytic degradation rate of Rhodamine B solution is 2 times higher than that of TiO_2 nanostructures without Ag nanocrystals [113]. A model system was also designed to ascertain the plasmon-enhanced absorption effect in photodegradation [114]. In this system, both Au nanorods and Au@Ag nanorods were hybridized to Pt/n-Si/Ag photodiodes,

respectively (Figure 1.10a and b). A silica film was employed to block the electron transfer between the plasmonic metal nanocrystals and semiconductors. The photodegradation properties are enhanced (Figure 1.10c). The decomposition rate of nitrobenzene is almost three times large after the decoration of Au@Ag nanocrystals under resonant illumination. The enhancement factor was found to show a strong spectral dependence, which qualitatively matches well with the LSPR spectrum of the metal nanocrystals. Au nanocrystals were found to enhance light absorption and act as an electron sinker by hybridization with Cu_2O nanowires. The photodegradation performance of methyl blue was highly improved under visible light [115].
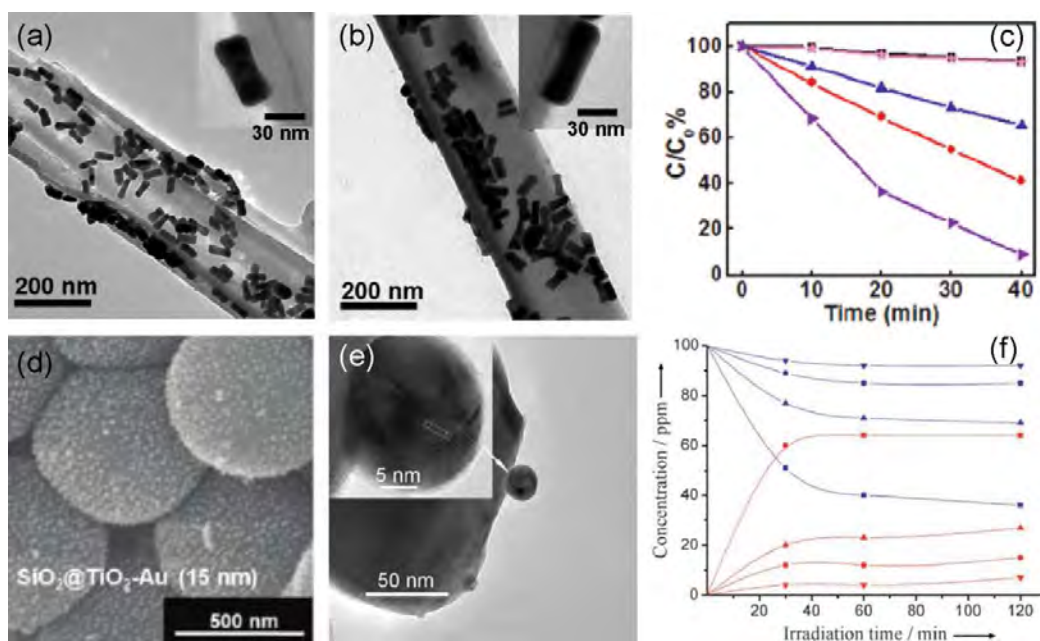
Figure 1.10 Plasmon-enhanced photodegradation of organic pollutants. (a,b) TEM images of Pt/n-Si/Ag photodiode decorated with Au nanorods and Au@Ag nanorods, respectively. The inset is an individual nanocrystal on the surface of the photodiode [114]. (c) Photodegradation of nitrobenzene including two controls and four catalysts. Nitrobenzene alone (black squares); Pt/n-Si/Ag photodiodes alone (blue triangles); Au nanorods-based diodes (red circles); mixture of nitrobenzene and Au@Ag nanorods (magenta stars); Au@Ag NRs-based diodes (violet right-triangles) [114]. (d) SEM image of Au nanocrystals deposited on $SiO_2@TiO_2$ nanospheres [116]. (e) TEM

image of Au nanocrystals decorated on ZrO_2. The white arrow indicates a Au nanocrystal [128]. (f) Oxidation of HCHO (100 ppm). The blue lines represent the reactant HCHO and the red lines refer to the product of CO_2. The reaction was carried out at different light intensities (square: 0.17; triangle: 0.13; circle: 0.08; inverted triangle: 0.02 W cm^{-2}) [128].

Photocatalytic degradation of organic pollutants was also achieved by directly incorporating plasmonic metal nanocrystals with wide-band-gap semiconductors on the basis of plasmonic sensitization. Ag or Au nanocrystals integrated with TiO_2 is a widely researched topic [113, 116–120]. Kim *et al.* reported a method to photodecompose methyl blue by utilizing Au nanocrystals decorated on $SiO_2@TiO_2$ nanospheres as the photocatalyst [116]. Scanning electron microscopy (SEM) imaging reveals that Au nanocrystals are uniformly decorated at a high density (Figure 1.10d). The plasmonic photocatalysts are photoactive under visible light illumination, while the $SiO_2@TiO_2$ nanospheres are only photo-responsive under ultraviolet light illumination. In other wide-band-gap semiconductors, such as silver halide and $KNbO_3$, plasmonic sensitization has also been observed [121–126]. Plasmonic metal nanocrystals supported on oxide semiconductors have also been utilized to decompose organic compounds to inorganic chemicals on the basis of photothermal heating [127]. Gao and his co-workers reported photocatalytic degradation of HCHO to CO_2 at room temperature using Au nanocrystal-loaded semiconductors including ZrO_2, CeO_2, and Fe_2O_3 nanostructures [128]. When Au nanocrystal-loaded ZrO_2 nanostructures were used as the catalyst (Figure 1.10e), the concentration of HCHO was decreased by 64% in 2 h under the illumination of blue light at a power density of 0.17 W cm^{-2} (Figure 1.10f). The content of CO_2 product was also increased accordingly. These results verify that HCHO can be decomposed into CO_2 at room temperature. The photocatalytic activity in this type of photocatalysts is tentatively ascribed to photothermal heating and hot holes. Such reactions taking place at ambient temperature offer great convenience for environmental purification in our daily life.

1.2.3.2 Synthesis of organic molecules

Plasmonic enhancement has also been demonstrated in photocatalytic synthesis of organic molecules. Photocatalytic synthesis of organic molecules is normally achieved by partial oxidation of reactants, while they are oxidized into small molecules in photodegradation. Semiconductor photocatalysts have limitations in the synthesis of organic molecules because of their high oxidation potentials [129]. Recently, selective oxidation of alcohols to carbonyl compounds with O_2 becomes very attractive. A lot of works have been devoted to the mild oxidation capability of Au nanostructures that were decorated on semiconductors [131–137]. Tada *et al.* found that the chemoselective oxidation of alcohols was highly improved when Au nanocrystal-deposited TiO_2 nanostructures were utilized as the catalyst [83]. Au nanocrystal-deposited CeO_2 nanostructures were also applied to oxidize benzyl alcohols to benzaldehydes in the presence of O_2 under the illumination of green light (Figure 1.11a). Plasmon-enhanced absorption in photocatalysis is further proved by correlation of the apparent quantum efficiency with the photoresponse of the Au/CeO_2 photocatalyst (Figure 1.11b). Hirai and co-workers found that Au nanocrystals located on the surface of P25 behave as the active sites to realize aerobic oxidation of 1-phenylethanol to acetophenone (Figure 1.11d) [70]. Under visible light illumination, the excited electrons in Au nanocrystals transfer to the conduction band of P25 nanostructure, which can thereafter oxidize 1-phenylethanol to acetophenone in the presence of O_2. The yield of acetophenone can be improved obviously (Figure1.10d). Sunlight was also used as the light source to activate this reaction, which will pave the way for cheap and easy chemical production.

In addition, pure plasmonic metal nanocrystals have also been used as photocatalysts to drive selective oxidation reactions. An important example is the one that ethylene is partially oxidized to ethylene oxide using Ag nanocubes as catalysts [84]. The oxidation rate increases almost fourfold upon visible light illumination in comparison with that of the experiment carried out in dark (Figure 1.11e). It is

postulated that the hot electrons, generated on the Ag nanocube surface under resonant excitation, inject to the lowest unoccupied molecular orbital of the adsorbed O_2, allowing for the activation of O–O bond at low temperatures. The detailed process has been illustrated in *Section 1.2.1* about the mechanisms. The activated O_2 molecules subsequently take part in partial oxidation of ethylene to ethylene oxide. Recently, several works have proved that the photocatalytic properties of pure noble metal nanocrystals are not unique to silver nanocubes [40,138,139]. Other plasmonic metal nanocrystals are also anticipated to be used as photocatalysts for the synthesis of organic compounds.
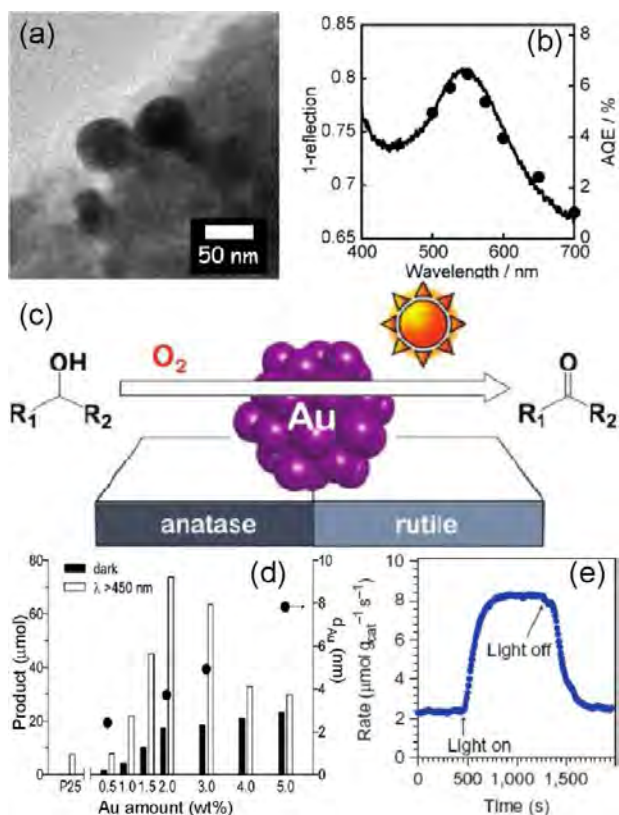
Figure 1.11 Plasmon-enhanced photocatalysis in the synthesis of organic molecules. (a) TEM image of Au nanocrystals loaded on CeO_2 nanostructures used for benzyl alcohol oxidation [83]. (b) Extinction spectrum of Au/CeO_2 (left axis) and the action spectrum in benzyl alcohol oxidation (block circles, right axis) [83]. (c) Schematic describing the catalyst constructed by loading Au nanocrystals on P25 nanostructures used to oxidize 1-phenylethanol under visible light illumination [70]. (d) Amounts of

acetophenone formed from the oxidation of 1-phenylethanol using Au/P25 as the catalyst [70]. (e) Rate of ethylene epoxidation in dark and under visible light illumination employing Ag nanostructures as the catalyst [84].

1.2.3.3 Water splitting

Since the production of hydrogen from water was first demonstrated by Fujishima and Honda in early 1970s [141], water splitting has attracted a lot of attention due to its potential to solve energy and environment issues. Two half-reactions are involved in photocatalytic water splitting, which are the oxygen-evolution half-reaction participated by holes ($H_2O + h^+ \rightarrow H^+ + O_2$) and the hydrogen-evolution half-reaction driven by electrons ($H^+ + e^- \rightarrow H_2$) [17]. Two major system configurations can be utilized to realize water splitting. One is the photoelectrochemical cell containing a working semiconductor electrode and a counter electrode. The hydrogen and oxygen half-reactions can occur on the two separate electrodes. For example, energetic holes execute the oxygen-evolution half-reaction on the working electrode for n-type semiconductors, while electrons move to the counter electrode and drive the hydrogen-evolution half-reaction. Another alternative design is on the basis of powder photocatalysts. In such systems, semiconductor photocatalysts are dispersed in water. Under light illumination, separated holes and electrons diffuse to the surface of the photocatalyst where they drive the hydrogen-evolution and oxygen-evolution half-reactions at specifically designed sites. In order to drive the water-splitting reaction, the bottom edge of the conduction band of semiconductors must be more negative than the H^+/H_2 potential, while the top edge of the valence band must be more positive than the O_2/H_2O potential.
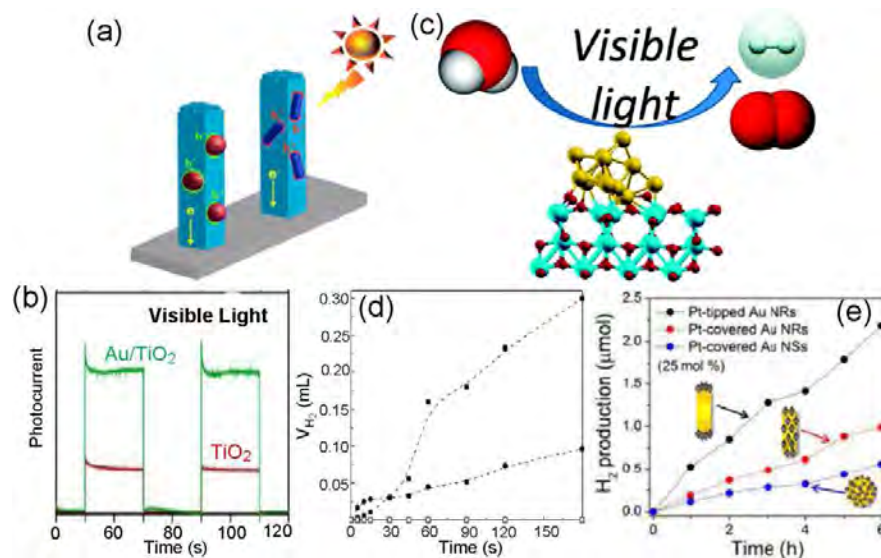
Figure 1.12 Plasmon-enhanced water splitting. (a) Schematic describing Au nanocrystal-decorated TiO_2 nanowires for photo electrochemical water splitting [147]. (b) Photocurrent curves *versus* Ag/AgCl for Au nanorod-decorated TiO_2 electrodes under visible light illumination (73.3 mW cm^{-2}, with a 430 nm long-pass filter) [147]. (c) Schematic depicting the Au nanocrystals supported on P25 used in photocatalytic water splitting [81]. (d) Photocatalytic H_2 generation under the illumination of a 532 nm-laser and visible light using Au(1.5 wt%)/TiO_2 nanostructures. Solid squares: Au/TiO_2 under 532 nm-laser; solid circles: Au/TiO_2 under visible light; hollow squares: Au/TiO_2 under 532 nm-laser; hollow circles: Au/TiO_2 under visible light [81]. (e) Time-dependent H_2 evolution under visible light illumination (460 nm–820 nm) using Pt-modified Au nanocrystals, including Pt-tipped, Pt-covered Au nanorods, and Pt-covered Au nanospheres, as catalysts [151].

Obviously, efficient light absorption and electron–hole separation will benefit water splitting. Several research works have demonstrated that the introduction of LSPR can improve water splitting performances [72,142–144]. Cronin and co-workers observed plasmon-enhanced photocurrents in water splitting under visible light illumination by loading Au nanocrystals on anodic TiO_2 electrodes [145]. The introduction of Ag nanocrystals increases the charge carrier concentrations in n-TiO_2 electrodes, leading to a ~10 enhancement factor of the photocurrent under visible light

illumination [146]. Recently, to enhance the photoactivity of the entire UV-visible region of sunlight, Li *et al.* attached Au nanospheres, nanorods, and their mixtures onto TiO_2 nanowire electrodes (Figure 1.12a) [147]. The photoactivities were all improved. For example, the photocurrent density of the Au nanorod-decorated TiO_2 electrode is almost three times that of the TiO_2 electrode (Figure 1.12b). These observations give us a new strategy to improve solar water splitting by employing plasmonic nanostructures. Photocatalysts that are dispersed into water pool have also been applied in plasmon-enhanced photocatalytic water splitting [148–150]. García and co-workers studied the generation of hydrogen or oxygen from water by use of Au nanocrystal-deposited TiO_2 as photocatalysts under either a monochromatic laser or filtered polychromatic light illumination (Figure 1.12c) [81]. Au/TiO_2 nanostructures were dispersed into water in the presence of ethylene diamine tetraacetic acid as a sacrificial electron donor. Hydrogen evolution using a monochromatic laser with a wavelength of 532 nm, which is the resonance wavelength of the Au nanocrystals, exhibits an increase in the evolution rate (Figure 1.11d). In contrast, only a negligible amount of hydrogen can be detected with TiO_2 as the catalyst. In this work, the Au nanocrystals play dual roles as light harvesters and catalytic sites for gas formation. Other semiconductors, such as WO_3 and CeO_2, decorated with Au nanocrystals, were also applied to drive the water-splitting reaction under visible light [82]. In addition, pure plasmonic metal nanocrystals can also act as photocatalysts for the water-splitting reaction. Very recently, Majima *et al.* reported a hydrogen generation under visible and near-infrared light illumination using Pt-modified Au nanocrystals as catalysts [151]. Under light illumination, hot electrons transfer from Au to Pt where the hydrogen-evolution half-reaction takes place. Pt-tipped Au nanorods, facilitating electron–hole separation, exhibit a much higher hydrogen generation rate compared with Pt-covered Au nanorods and Au nanospheres (Figure 1.12e). Since the research on plasmon-enhanced water splitting is still at the early stage, the findings described above provide insights to the design of novel photocatalysts in this area.

1.3 Metal/Semiconductor Nanostructures for Plasmon-Enhanced Solar Energy Harvesting Applications

Plasmon-enhanced applications in light harvesting are highly dependent on their configurations, such as the size, shape, and composition of the individual component. Although hybrid nanostructures that are formed by decorating plasmonic metal nanocrystals onto semiconductors show splendid photoactivities, there are still disadvantages that need to be overcome to further fully realize the potential of plasmon. First, the size and shape of the plasmonic nanocrystals are difficult to be controlled, leading to the difficulty in the control of the photocatalytic activity. Second, the nanostructures are exposed to reactants, products, and the surrounding. They therefore suffer from aggregation and shape or size changes, resulting in the loss or change of the unique properties seen in the original nanocrystals. The decorated metal nanocrystals can fall off from the semiconductors because of the weak adhesive force, which will lower their recycling capability. Additionally, the active interface is also small. Special nanostructures, including core/shell, eccentric, york/shell, and Janus nanostructures have therefore been prepared for the sake of improving the photocatalytic performance. In this section, I will introduce their preparation, properties, and applications in solar energy harvesting.

1.3.1 Preparation of Plasmonic Metal/Semiconductor Nanostructures

Preparation is the first step for any application involving plasmonic metal/semiconductor nanostructures. The synthesis of metal/semiconductor nanostructures is crucial during my PhD study. I will therefore summarize the solution-based synthesis method beforehand in this section.

The most widely employed strategy for preparing metal/semiconductor nanostructures is based on so-called a "seeded growth" approach. The seeds are

pre-grown metal nanocrystals (or semiconductors), which serve as primary growth centers for accommodating secondary semiconductor (or metal) portions of different components. The use of the "seeded growth" method to prepare metal/semiconductor nanostructures allows the shapes and sizes and thus their plasmonic properties to be rationally chosen. Thermodynamically, the growth energy barrier that requires for a given material to condensation on the seeds should be lower than the activation energy that is needed to trigger the corresponding self-nucleation. Furthermore, the facet energy of the seeds is an important factor in determining the final morphology. A secondary material can grow on the seeds forming core/shell nanostructures with continuous and discrete shell, if the seeds have exposed facets with similar energies. On the other hand, if the energies of the exposed facets are significantly different, metal/semiconductor nanostructures will grow into asymmetric eccentric or Janus nanostructures. To date, various semiconductors, spanning from narrow-band-gap to wide-band-gap semiconductors, have been involved to design and synthesize metal/semiconductor nanostructures, such as oxide, chalcogenide, halogen semiconductors, and so forth [152–156]. As an example for narrow-band-gap semiconductors, Cu_2O with a bandgap of 2.1 eV is grown on metal nanocrystals. Huang et $al.$ prepared (Au nanocrystal)/(Cu_2O shell) nanostructures by using Au nanocrystals as structure-directing cores, which were mixed with $CuCl_2$, surfactant, NaOH, and $NH_2OH \cdot HCl$. Different shell morphologies were obtained by varying the shape of Au nanocrystal core and the volume of $NH_2OH \cdot HCl$ [153]. Rod-like (Au nanocrystal)/(Cu_2O shell) nanostructures were synthesized in this work when Au nanorods were employed as the cores. Another group obtained a uniform truncated octahedral (Au nanocrystal)/(Cu_2O shell) nanostructures using Au nanorods as the cores (Figure 1.13a) when $Cu(NO_3)_2$ was employed as the precursor [155]. This strategy was also extended to other metal nanocrystals, such as Pt, Pd, and Ag nanocrystals [157]. Another type of semiconductors widely hybridized with metals is wide-band-gap semiconductors. Besides core/shell morphology, other symmetry-breaking structures, such as eccentric, Janus, or york/shell structures, have

also been prepared [10,156,158]. For example, (Au nanosphere core)/(ZnS shell) nanostructures were synthesized under hydrothermal condition (Figure 1.13b) [156]. The presence of Ag^+ builds a wetting layer, which is necessary for the successful deposition of ZnS on Au nanocrystals. Han and co-workers prepared eccentric Au/TiO_2 nanostructures using pre-formed Au nanospheres as seeds (Figure 1.13c) [158]. The facet-dependent binding strength of citrate ions on Au nanospheres induces facet-selective condensation of TiO_2 in the sol–gel coating process. When the cetyltrimethylammonium bromide-stabilized Au nanospheres or nanorods were used as the seeds, Janus structures were obtained by the same synthesis route (Figure 1.13d and e) [160]. Starting from pre-made semiconductors, several works have been devoted to the synthesis of (semiconductor core)/(metal shell) nanostructures [161,162]. (Fe_2O_3 core)/(Au shell) nanostructures have been prepared using spindle-shaped hematite as seeds (Figure 1.13f) [163]. For the growth of Au shell, the seeds were modified with amine molecules, which facilitated the deposition and growth of Au shell.
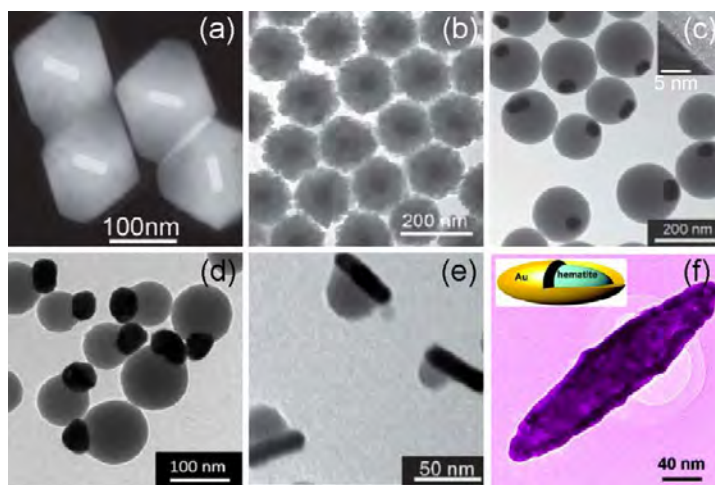
Figure 1.13 Metal/semiconductor nanostructures prepared by the "seeded growth" method. (a) High-angle annular dark-field scanning transmission electron microscopy image of the (Au nanorod core)/(Cu_2O shell) nanostructures [155]. (b–f) TEM images of (Au nanosphere core)/(ZnS shell), eccentric (Au nanosphere)/TiO_2, Janus (Au nanosphere)/TiO_2, Janus (Au nanorod)/TiO_2, and (Fe_2O_3 nanorice core)/(Au shell)

nanostructures. The inset in (f) is the schematic of the core/shell nanostructure [156,158,160].

There have been successful efforts to develop one-pot methods for the synthesis of metal/semiconductor nanostructures, in which metal and semiconductor precursors are simultaneously placed together. Under appropriate conditions, the precursors generate homogeneous nucleation of the individual components, forming special configurations. To realize such smart systems has been a challenging task. So far, only a few cases have been documented [164–170]. In general, the reduction of metal ions induces fast nucleation of metal nanoparticles which is subsequently hybridized with semiconductors. With such a one-pot synthesis method, it is much difficult to control the shape of plasmonic metal nanocrystals. Ag and Au nanocrystals have been involved in this strategy. For instance, Hu *et al.* developed a thermal-decomposition route for preparing Janus Ag/Ag_2S nanostructures by a one-pot method (Figure 1.14a) [167]. In this process, silver precursor was injected into hot oleylamine at 180 °C under N_2 atmosphere. It is proposed that Ag nuclei are first generated at a low temperature due to the decomposition of the silver precursor followed by the coating of Ag_2S at a high temperature. Janus Ag/Ag_2S nanostructures were formed at an even higher temperature. Li and co-workers also reported a solvothermal method to prepare (Ag core)/(Fe_3O_4 shell) nanostructures *via in situ* chemical reduction of $AgNO_3$ and $Fe(NO_3)_3$ (Figure 1.14b) [168]. The size of the core and the thickness of the shell can be tuned by carefully choosing the reaction conditions. (Ag core)/(TiO_2 shell) nanostructures, a wide-band-gap semiconductor as the shell, have also been grown by a one-pot synthesis route, which involves the reduction of silver ions and the hydrolysis of titanium(triethanolaminato)isopropoxide [169]. (Au core)/(TO_2 shell) nanostructures were also achieved, in which $HAuCl_4$ was mixed with a reduction agent and TiT_4 followed by a hydrothermal possess [170]. Figure 1.14c is the SEM image of the obtained (Au nanosphere core)/(TiO_2 shell) nanostructures. Other metal nanocrystals, such as Pd and Pt, can also be applied in such growth routes to obtain respective metal/semiconductor nanostructures.
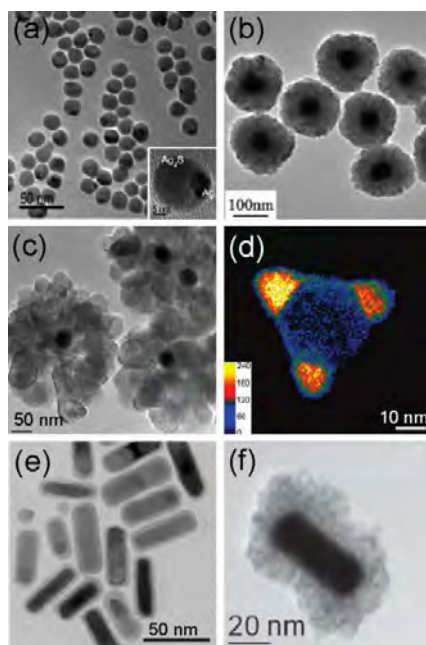
Figure 1.14 Metal/semiconductor nanostructures prepared by other methods. (a–c) TEM images of Janus Ag/Ag$_2$S, (Ag core)/(Fe$_3$O$_4$ shell), and (Au core)/(TiO$_2$ shell) nanostructures, respectively. The inset in (a) is the TEM image of the magnified individual Janus Ag/Ag$_2$S nanostructure [167,168,170]. (d) Color-composite energy-filtered TEM image of an individual Ag/Ag$_2$S nanoplate. The orange color corresponds to S. The color scale in the inset indicates the electron counts of the image. (e,f) TEM images of (Au nanorod core)/(Ag$_2$S shell) and (Au nanorod core)/(CdS shell) nanostructures, respectively [180].

On certain occasions, pre-grown plasmonic metal nanocrystals can take part in chemical reactions acting as a reactant. A metal/semiconductor nanostructure is formed if metal nanocrystals are partially reacted. Ag nanocrystals, as an example, in monometallic form were sulfidated into Ag$_2$S to form Ag/Ag$_2$S nanostructures [171–175]. As illustrated in Figure 1.14d, Xia's group synthesized Ag/Ag$_2$S nanoplates by partial sulfidation of Ag nanoplates using NaS$_x$ solution. The Ag/Ag$_2$S nanostructures keep the shape of the Ag nanocrystals, which is also confirmed by employing Ag nanospheres and nanocubes in the sulfidation reaction. On the other hand, bimetallic nanocrystals are good candidates for the synthesis of

metal/semiconductor nanostructures. The metal component with low chemical activity maintains its plasmonic properties, while the other one with high chemical activity participates in the reaction to form a semiconductor. Au/Ag bimetallic nanocrystals were employed in the formation of Au/(silver chalcogenide) nanostructures [176–180]. For example, Guyot-Sionnest *et al.* synthesized (Au core)/(Ag$_2$S shell) nanostructures by the sulfidation of Au/Ag bimetallic nanorods (Figure 1.14e) [180]. Ag shell is sulfidated into narrow-band-gap Ag$_2$S shell by (NH$_2$)$_2$CS at room temperature. Wang's group further converted Ag$_2$S shell into CdS shell through a cation-exchange process [181]. The (Au nanorod core)/(CdS shell) nanostructures were prepared by just stirring the mixture of pre-made (Au core)/(Ag$_2$S shell) nanostructures with Cd(NO$_3$)$_2$ solution at room temperature. This route creates new possibilities for the synthesis of plasmonic metal/semiconductor nanostructures.

1.3.2 Properties of Plasmonic Metal/Semiconductor Nanostructures

Metal/semiconductor nanostructures give an opportunity to combine LSPR with semiconducting properties and achieve synergistic behaviors. When a metal nanocrystal is in contact with semiconductor, the conduction and valence band of the semiconductor component is bent at the interface. The major properties of the semiconductor ingredient, such as the bandgap energy, remain unchanged. Besides, the LSPR properties of the metal nanocrystal will be significantly altered after the formation of the metal/semiconductor nanostructure. First of all, the metal/semiconductor nanostructure offers a way to synthetically tune the LSPR properties, because LSPR is highly dependent on the surrounding medium. In general, the localized plasmon resonance wavelength of a noble metal nanocrystal shows a red shift after the metal nanocrystal is hybridized with a semiconductor because of the general higher dielectric function of the semiconductor. For example, tunable full-color of LSPR in the visible range has been achieved by varying the composition of Au@Ag@Ag$_2$S nanocubes [178]. The plasmon resonance wavelength can be tuned

from ~500 nm to ~750 nm by continuous addition of sulfide ions into Au@Ag nanocubes (Figure 1.15a). The sulfide ions react with Ag shell and generate Ag_2S, causing the red shift of the extinction peak. The aqueous colloidal solutions therefore exhibit rich colors as indicated by their digital photographs. In addition, the LSPR of the metal/semiconductor nanostructure can also be tuned by control of the configuration [182] and phase transition of the shelled semiconductor [183].
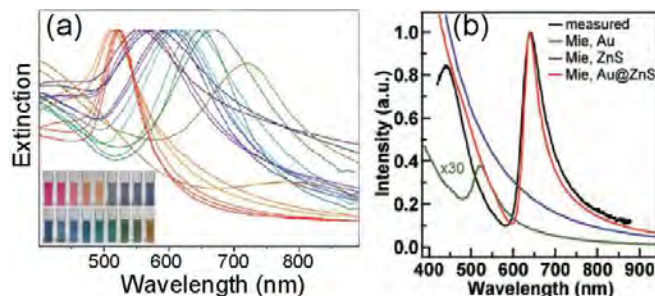
Figure 1.15 LSPR properties of metal/semiconductor nanostructures. (a) Extinction spectra indicating the LSPR variations during the sulfidation of Au@Ag nanocubes. The inset is the digital photograph of corresponding colloidal solutions [178]. (b) Measured and calculated scattering spectra of a single (Au core)/(ZnS shell) nanostructure. The scattering spectra of the Au core and hollow ZnS shell were calculated separately according to Mie theory [184].

Metal/semiconductor nanostructures can trigger new plasmon resonance behaviors, which are significantly different from those of the corresponding plasmonic metal nanocrystal and semiconductor ingredients. The modification of the incident electromagnetic field by the semiconductor component changes the interaction of the incident light and plasmonic metal nanocrystal, enabling the appearance of new intriguing plasmon resonance properties. Fano resonances characterized by their asymmetric non-Lorentzian spectral profile have been observed in metal/semiconductor nanostructures [184]. The asymmetric scattering profiles resulting from Fano resonance in (Au sphere core)/(sulfide shell) nanostructures have been observed. Figure 1.15b displays the calculated and measured scattering spectra of a single (Au sphere core)/(ZnS shell) nanostructure. The Au nanosphere shows a

scattering peak at around 525 nm. The hollow ZnS shell exhibits an increasing scattering background toward the short-wavelength region. However, the (Au sphere core)/(ZnS shell) nanostructure gives a scattering peak that has a clear asymmetric Fano line shape. The calculated scattering is in good agreement with the measured one. The interference between the narrow plasmon resonance of the Au core and the broad scattering from the ZnS shell causes the Fano resonance. Under appropriate light excitation, the electromagnetic field induces both the electron oscillation of the Au core and the polarization charge oscillation of the ZnS shell. The polarization charges in the ZnS shell can interact with and transfer energy to the free electrons in the Au core through the Coulombic interaction. Such an interaction mechanism leads to the red shift and enhancement of the plasmon resonance in the Au core. Because a jump of π in the phase shift occurs across the narrow plasmon resonance [185], the interference changes from constructive to destructive. The destructive interference reduces the total oscillation strength due to the partial cancellation between the free electron and polarization charge oscillations, resulting in an asymmetric scattering peak. New plasmonic Fano materials can be designed on the basis of these observations.

1.3.3 Plasmonic Metal/Semiconductor Nanostructures in Solar Energy Harvesting

Plasmonic metal/semiconductor nanostructures with special configurations offer a unique opportunity in solar energy harvesting compared with metal nanocrystal-decorated semiconductor nanostructures. For example, core/shell nanostructures provide "three-dimensional" contact between the plasmonic metal nanocrystal and the semiconductor components, which facilitates charge transfer processes at the interface. Janus nanostructures merge two or more components at a junction site and expose other regions, giving a chance to enhance desired properties as well as producing synergistic effects. Compared with plasmonic metal nanocrystal-decorated semiconductors, specially structured metal/semiconductor nanostructures hold more inherent advantages in plasmon-enhanced solar cells and photocatalysis. Since plasmon-enhanced solar harvesting applications using plasmonic metal nanocrystal-decorated semiconductors have been illustrated carefully in *Section 1.2*, below I will therefore only select several well-designed nanostructures as examples to demonstrate the applications of specially structured metal/semiconductor nanostructures in photovoltaic and photocatalytic applications. As described above, although the incorporation of $Au@SiO_2$ prevents the corrosion of metal nanocrystals in dye-sensitized solar cells, the collection efficiency of photo-induced charge carriers is low due to the insulating SiO_2 shell [109]. In this regard, (plasmonic metal core)/(semiconductor shell) nanostructures become excellent candidates in plasmon-enhanced solar cells [186–189]. (Ag core)/(TiO_2 shell) nanostructures have been incorporated into the TiO_2 photoanode in dye-sensitized solar cells, which prevents charge carrier recombination and back reaction, protects metal corrosion, improves charge transfer, and maximizes the LSPR effect [109]. Figure 1.16a depicts the current density–voltage and power conversion efficiency curves of the traditional and plasmonic dye-sensitized solar cells with the same photoanode thickness. The plasmonic dye-sensitized solar cells with (Ag core)/(TiO_2 shell) nanostructures show an increase of 37% in the short-circuit current density from

6.07 mA/cm^2 to 8.31 mA/cm^2. The power conversion efficiency is also improved by 42% from 3.1% to 4.4%. Moreover, the optimal photoanode thickness was also examined. It is found that the power conversion efficiency was improved by 15% after the introduction of (Ag core)/(TiO$_2$ shell) nanostructures, while the photoanode thickness was decreased by 25%. It is expected that this approach will enable the utilization of plasmonic (metal core)/(semiconductor shell) nanostructures in other thin-film photovoltaic devices.
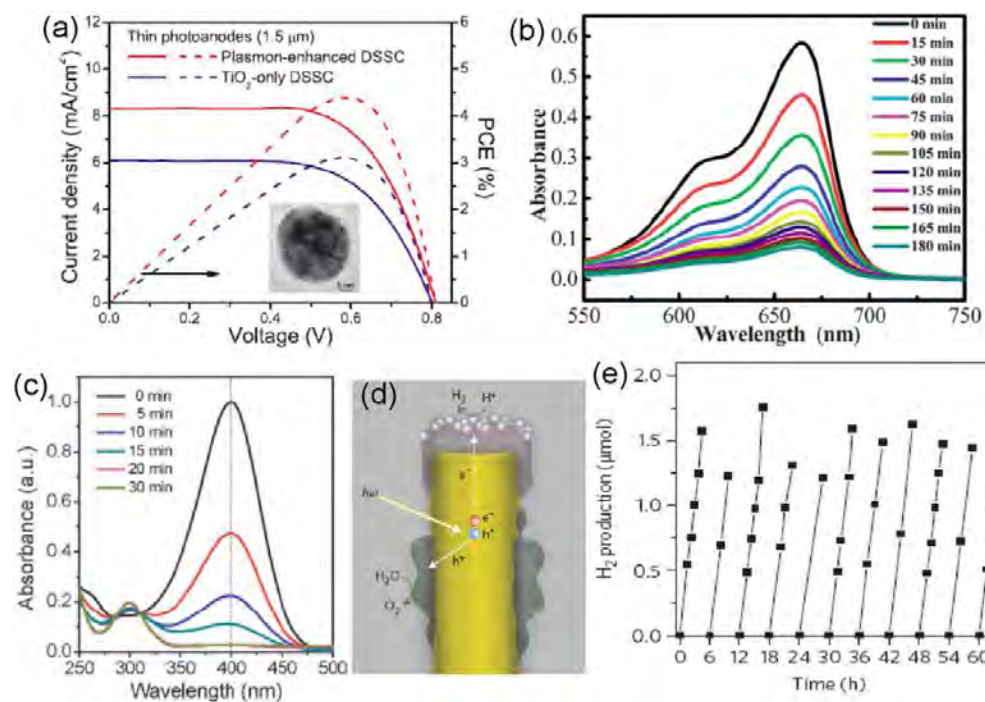
Figure 1.16 Metal/semiconductor nanostructures with special configurations in solar energy harvesting applications. (a) Current density (solid lines) and power conversion efficiency (dashed lines) curves of the plasmonic and TiO$_2$-only dye-sensitized solar cells with the same photoanode thickness of 1.5 μm. The inset is the TEM image of a single (Ag core)/(TiO$_2$ shell) nanostructure [109]. (b) Time-dependent absorption spectra of methylene blue upon visible light illumination in the presence of (Au/Ag core)/(TiO$_2$ shell) nanostructures as the photocatalyst [197]. (c) Time-dependent variations of the absorption spectra during the catalytic reduction process of 4-nitrophenol [159]. (d) Schematic of an individual plasmonic photocatalyst in water splitting, which is composed of an inner Au nanorod, the shelled TiO$_2$, and the

decorated Pt nanoparticles [198]. (e) Hydrogen evolution as a function of the illumination time under visible light ($\lambda > 410$ nm) [198].

A vast number of experiments have demonstrated the potential applications of metal/semiconductor nanostructures with special configurations in photocatalysis, such as photodegradation of organic pollutants, photosynthesis of organic compounds, and photon-induced water splitting [119,160,170,190–196]. Xu and co-workers examined the photocatalytic activities of (Au/Ag core)/(TiO$_2$ shell) nanostructures under visible light by decomposing methylene blue [197]. From the absorption spectra taken at different illustration time (Figure 1.16b), methylene blue is seen to gradually decompose under visible light. 86% of methylene blue is degraded after illumination for 180 min. The enhanced photocatalytic property is ascribed to the highly effective light absorption of the plasmonic Au/Ag nanocrystals, which can inject the photon-induced hot electrons to the conduction band of TiO$_2$. Eccentric Au/TiO$_2$ nanostructures were employed in the photocatalytic reduction of 4-nitrophenol into 4-aminophenol [159]. As indicated from the absorption spectra (Figure 1.16c), the absorption intensity of 4-nitrophenol at 400 nm decreases with the illumination time and a new peak at 400 nm appears, proving the successful synthesis of 4-aminophenol. Moreover, under the protection of the shelled TiO$_2$, the photocatalyst is stable enough to be reactivated and reused over five cycles without obvious reduction in photoactivity. Moskovits *et al.* designed a plasmonic "water splitter" based on a TiO$_2$-coated Au nanorod array [198]. The water splitter consisting of an aligned Au nanorod coated with TiO$_2$ functions as a light-harvesting antenna. Pt nanocrystals and a cobalt-based catalyst were integrated to enhance hydrogen and oxygen generation, respectively. The detailed structure is shown in Figure 1.16d. Electron–hole pairs are generated upon the plasmon excitation of the Au nanorods. The hot electrons inject to the conduction band of TiO$_2$ and transport to the Pt nanoparticles to generate hydrogen. The holes move to the cobalt-based catalyst to produce oxygen. Experimentally, hydrogen was clearly detected even after illumination for ~2 h (Figure 1.15e). No noticeable reduction in photoactivity was observed after 11

sequential 6-h runs. The hydrogen production rate was estimated to be 0.25 μmol h^{-1} in a cell with the photocatalyst weighted at 0.22 mg. The involvement of plasmonic metal/semiconductor hybrid nanostructures offers an encouraging way to achieve efficient solar energy harvesting, although the solar-to-energy efficiency is still too low for practical utilization.

1.4 Outline of This Thesis

As stated above, plasmonic metal/semiconductor nanostructures have great potentials in solar energy harvesting applications, which is of vital benefit for human life. Many efforts should be made on this area to pave the way for the practical use of plasmonic metal/semiconductor nanostructures, such as the investigation of their plasmonic properties and novel synthesis route. Any of improvements in this area will undoubtedly make plasmonic metal/semiconductor nanostructures richer and more useful. In this thesis, I will thus focus on plasmonic metal/semiconductor nanostructures, including the plasmonic properties and synthesis methods. Two typical semiconductors, narrow-band-gap Ag$_2$S and wide-band-gap TiO$_2$, are hybridized with plasmonic metal nanocrystals during my PhD study. The detailed contents of this thesis are organized as follows.

I will present the experimental preparation of noble metal nanocrystals in Chapter 2, which is the basis of this thesis. The characterization techniques I used will also be introduced in this chapter.

Chapter 3 gives the details of my research on the formation process of Ag/Ag$_2$S nanocubes by sulfidation of Ag nanocubes. The plasmonic properties of Ag nanocubes, and the spectral, plasmonic, and structural evolutions during the sulfidation process are investigated in detail. A sulfidation process is also proposed. In Chapter 4, I will introduce my work on (Au core)/(TiO$_2$ shell) nanostructures. I have developed a versatile and convenient route to the preparation of (metal core)/(TiO$_2$

shell) nanostructures at room temperature. TiO$_2$ coating has been successfully carried out on monometallic and bimetallic Pd, Pt, Au nanocrystals. I have also examined the plasmon-enhanced photon harvesting applications of (Au nanocrystal core)/(TiO$_2$ shell) nanostructures in dye-sensitized solar cells and the generation of reactive oxygen species. Furthermore, I will introduce my work on the tunable Fano resonance of (Au nanorod core)/(TiO$_2$ shell) nanostructures in Chapter 5. The effects of the plasmon resonance energy of the Au nanorod core on Fano resonance have been investigated experimentally.

Finally, a conclusion will be given in Chapter 6.

References

[1] Andres, R. P.; Bielefeld, J. D.; Henderson, J. I.; Janes, D. B.; Kolagunta, V. R.; Kubiak, C. P.; Mahoney, W. J.; Osifchin, R. G. *Science* **1996**, *273*, 1690–1693.

[2] Millstone, J. E.; Park, S.; Shuford, K. L.; Qin, L.; Schatz, G. C.; Mirkin, C. A. *J. Am. Chem. Soc.* **2005**, *127*, 5312–5313.

[3] Ming, T.; Feng, W.; Tang, Q.; Wang, F.; Sun, L. D.; Wang, J. F.; Yan, C. H. *J. Am. Chem. Soc.* **2009**, *131*, 16350–16351.

[4] Kelly, K. L.; Coronado, E.; Zhao, L. L.; Schatz, G. C. *J. Phys. Chem. B* **2003**, *107*, 668−677.

[5] Boltasseva, A.; Atwater, H. A. *Science* **2011**, *331*, 290–291.

[6] Manthiram, K.; Alivisatos, A. P. *J. Am. Chem. Soc.* **2012**, *134*, 3995–3998.

[7] Luther, J. M.; Jain, P. K.; Ewers, T.; Alivisatos, A. P. *Nat. Mater.* **2011**, *10*, 361–366.

[8] Zhao, Y. X.; Pan, H. C.; Lou, Y. B.; Qiu, X. F.; Zhu, J. J.; Burda, C. *J. Am. Chem. Soc.* **2009**, *131*, 4253–4261.

[9] Ming, T.; Chen, H. J.; Jiang, R. B.; Li, Q.; Wang, J. F. *J. Phys. Chem. Lett.* **2012**, *3*, 191–202.

[10] Jiang, R. B.; Li, B. X.; Fang, C. H.; Wang, J. F. *Adv. Mater.* DOI: 10.1002/adma.201400203.

[11] Sau, T. K.; Rogach, A. L.; Jäckel, F.; Klar, T. A.; Feldmann, J. *Adv. Mater.* **2010**, *22*, 1805–1825.

[12] Kou, X. S.; Ni, W. H.; Tsung, C.-K.; Chan, K.; Lin, H.-Q.; Stucky, G. D.; Wang, J. F. *Small*, **2007**, *3*, 2103–2113.

[13] Shao, L.; Fang, C. H.; Chen, H. J.; Man, Y. C.; Wang, J. F.; Lin, H.-Q. *Nano Lett.* **2012**, *12*, 1424–1430.

[14] Shao, L.; Woo, K. C.; Chen, H. J.; Jin, Z.; Wang, J. F.; Lin, H.-Q. *ACS Nano* **2010**, *4*, 3053–3062.

[15] Burda, C.; Chen, X.; Narayanan, R.; El-Sayed M. A. *Chem. Rev.* **2005**, *105*,

1025–1102.

[16] Evanoff, Jr., D. D.; Chumanov, G. *Chem. Phys. Chem.* **2005**, *6*, 1221–1231.

[17] Linic, S.; Christopher, P.; Ingram, D. B. *Nat. Mater.* **2011**, *10*, 911–921.

[18] Jain, P. K.; Huang, X. H.; El-Sayed, I. H.; El-Sayed M. A. *Acc. Chem. Res.* **2008**, *41*, 1578–1586.

[19] Schuller, J. A.; Barnard, E. S.; Cai, W. S.; Jun, Y. C.; White, J. S.; Brongersma, M. L. *Nat. Mater.* **2010**, *9*, 193–204

[20] Yang, T.; Tatsuma, T. *J. Am. Chem. Soc.* **2005**, *127*, 7632–7637.

[21] Matthew, P.; Garnett, B. Introduction to metal-nanoparticle plasmonics 52.

[22] Yang, Y. Y.; Huang, S. M.; He, H. Z.; Mau, A. W. H.; Dai, L. M. *J. Am. Chem. Soc.* **1999**, *121*, 10832–10833.

[23] Sohn, J. I.; Lee, S.; Song, Y.-H.; Choi, S.-Y.; Cho, K.-I.; Nam, K.-S. *Appl. Phys. Lett.* **2001**, *78*, 901–903.

[24] Revzin, A.; Russell, R. J.; Yadavalli, V. K.; Koh, W.-G.; Deister, C.; Hile, D. D.; Mellott, M. B.; Pishko, M. V. *Langmuir* **2001**, *17*, 5440–5447.

[25] Shao, L.; Ruan, Q. F.; Jiang, R. B.; Wang, J. F. *Small* **2014**, *10*, 802–811.

[26] Rycenga, M.; Cobley, C. M.; Zeng, J.; Li, W. Y.; Moran, C. M.; Zhang, Q.; Qin, D.; Xia, Y. N. *Chem. Rev.* **2011**, *111*, 3669–3712.

[27] Tao, A.; Sinsermsuksakul, P. Yang, P. D. *Angew. Chem. Int. Ed.* **2006**, *45*, 4597–4601.

[28] Wiley, B. J.; Wang, Z. H.; Wei, J.; Yin, Y. D.; Cobden, D. H.; Xia, Y. N. *Nano Lett.* **2006**, *6*, 2273–2278.

[29] Wiley, B. J.; Sun, Y. G.; Mayers, B.; Xia, Y. N. *Chem. Eur. J.* **2005**, *11*, 454–463.

[30] Wiley, B. J.; Sun, Y. G.; Xia, Y. N. *Acc. Chem. Res*. **2007**, *40*, 1067–1076.

[31] Sun, Y. G.; Xia, Y. N. *Science* **2002**, *298*, 2176–2179.

[32] Wiley, B. J.; Xiong, Y. J.; Li, Z.-Y.; Yin, Y. D.; Xia, Y. N. *Nano Lett.* **2006**, *6*, 765–768.

[33] Wiley, B. J.; Herricks, T.; Sun, Y. G.; Xia, Y. N. *Nano Lett*. **2004**, *4*, 1733–1739.

[34] Li, N.; Zhao, P. X.; Astruc. D. *Angew. Chem. Int. Ed.* **2014**, *53*, 1756–1789.

[35] Jana, N. R.; Gearheart, L.; Murphy, C. J. *J. Phys. Chem. B* **2001**, *105*, 4065–4067

[36] Nikoobakht, B.; El-Sayed, M. A. *Chem. Mater.* **2003**, *15*, 1957–1962.

[37] Orendorff, C. J.; Murphy, C. J. *J. Phys. Chem. B* **2006**, *110*, 3990–3994.

[38] Pérez-Juste, J.; Liz-Marzán, L. M.; Carnie, S.; Chan, S. Y. C.; Mulvaney, P. *Adv. Funct. Mater.* **2004**, *14*, 571–579.

[39] Xiao, M. D.; Jiang, R. B.; Wang, F.; Fang, C. H.; Wang, J. F.; Yu, J. C. *J. Mater. Chem. A* **2013**, *1*, 5790–5805.

[41] Porter, M. D.; Lipert, R. J.; Siperko, L. M.; Wang, G. F.; Narayanan, R. *Chem. Soc. Rev.* **2008**, *37*, 1001–1011.

[42] Qian, X.-M.; Nie, S. M. *Chem. Soc. Rev.* **2008**, *37*, 912–920.

[43] Kim, S.; Jin, J. H.; Kim, Y.-J.; Park, I.-Y.; Kim, Y.; Kim, S.-W. *Nature* **2008**, *453*, 757–760.

[44] Park, I.-Y.; Kim, S.; Choi, J.; Lee, D.-H.; Kim, Y.-J.; Kling, M. F.; Stovkman, M. I.; Kim, S.-W. *Nat. Photonics* **2011**, *5*, 677–681.

[45] Fan, Z. Y.; Govorov, A. O. *Nano Lett.* **2010**, *10*, 2580–2587.

[46] Slocik, J. M.; Govorov, A. O.; Rajesh, R. N. *Nano Lett.* **2011**, *11*, 701–705.

[47] Kinkhabwala, A.; Yu, Z. F.; Fan, S. H.; Avlasevich, Y.; Müllen, K.; Moerner, W. E. *Nat. Photonics* **2009**, *3*, 654–657.

[48] Ming, T.; Zhao, L.; Yang, Z.; Chen, H. J.; Sun, L. D.; Wang, J. F.; Yan, C. H. *Nano Lett.* **2009**, *9*, 3896–3903.

[49] Zheludev, N. I.; Prosvirnin, S. L.; Papasimakis, N.; Fedotov, V. A. *Nat. Photonics* **2008**, *2*, 351–354.

[50] Noginov, M. A.; Zhu, G.; Belgrave, A. M.; Bakker, R.; Shalaev, V. M.; Narimanov, E. E.; Stout, S.; Herz, E.; Suteewong, T., Wiesner, U. *Nature* **2009**, *460*, 1110–1112.

[51] Kerker, M.; Wang, D.-S.; Chew, H. *J. Chem, Phys.* **1978**, *69*, 4159–4174.

[52] Moskovits, M. *Rev. Mod. Phys.* **1985**, *57*, 783–825.

[53] Chen, C. Y.; Burstein, E. *Phys. Rev. Lett.* **1980**, *45*, 1287–1291.

[54] Nikoobakht, B.; Wang, J. P.; El-Sayed, M. A. *Chem. Phys. Lett.* **2002**, *366*,

17–23.

[55] Kumar, J.; Thomas, G. *J. Phys. Chem. Lett*. **2011**, *2*, 610–615.

[56] Schmelzeisen, M.; Zhao, Y.; Klapper, M.; Müllen, K.; Kreiter, M. *ACS Nano* **2010**, *4*, 3309–3317

[57] Pompa, P. P.; Martiradonna, L.; Torre, A. D.; Sala, F. D.; Manna, L.; Vittorio, D.; Calabi, F.; Cingolani, R.; Rinaldi, R. *Nat. Nanotechnol.* **2006**, *1*, 126–130.

[58] Dykman, L.; Khlebesov, N. *Chem. Soc. Rev.* **2012**, *41*, 2256–2282.

[59] Huang, X. H.; El-Sayed, I. H.; Qian, W.; El-Sayed, M. A. *J. Am. Soc. Chem.* **2006**, *128*, 2115–2120.

[60] Dreaden, E. C.; Alkilany, A. M.; Huang, X. H.; Murphy, C. J.; El-Sayed, M. A. *Chem. Soc. Rev*. **2012**, *41*, 2740–2779.

[61] Chande, N.; Shukla, R.; Katti, K. V.; Kannan, R. *Nano Lett*. **2009**, *9*, 1798–1805.

[62] Hirsch, L. R.; Stafford, R. J.; Bankson, J. A.; Sershen, S. R.; Rivera, B.; Price, R. E.; Hazle, J. D.; Halas, N. J.; West, J. L. *Proc. Natl Acad. Sci. USA.* **2003**, *100*, 13549–13554.

[63] Park, J.-H.; Maltzahn, G. V.; Xu, M. J.; Fogal, V.; Kotamraju, V. R.; Ruoslahti, E.; Bhatia, S. N.; Sailor, M. J. *Proc. Natl Acad. Sci. USA.* **2010**, *107*, 981–986.

[64] Yang, X. J.; Liu, X.; Liu, Z.; Pu, F.; Ren, J. S.; Qu, X. G. *Adv. Mater*. **2012**, *24*, 2890–2895.

[65] Mayer, K. M.; Lee, S.; Liao, H. W.; Rostro, B. C.; Fuentes, A.; Scully, P. T.; Nehl, C. L.; Hafner, J. H. *ACS Nano* **2008**, *2*, 687–692.

[66] Truong, P. L.; Cao, C.; Park, S.; Kim, M.; Sim, S. J. *Lab Chip* **2011**, *11*, 2591–2597.

[67] Wang, G. Q.; Chen, Z. P.; Wang, W. H.; Yan, B.; Chen, L. X. *Analyst* **2011**, *136*, 174–178.

[68] Rex, M.; Hernandez, F. E.; Campiglia, A. D. *Anal. Chem*. **2006**, *78*, 445–451.

[69] Huang, H. W.; Qu, C. T.; Liu, X. Y.; Huang, S. W.; Xu, Z. J.; Zhu, Y. J.; Chu, P. K. *Chem. Commun*. **2011**, *47*, 6897–6899.

[70] Tsukamoto, D.; Shiraishi, Y.; Sugano, Y.; Ichikawa, S.; Tanaka, S.; Hirai, T. *J. Am.*

Soc. Chem. **2012**, *134*, 6309–6315.

[71] Thimsen, E.; Formal, F. L.; Grätzel, M.; Warren, S. C. *Nano Lett*. **2011**, *11*, 35–43.

[72] Thomann, I.; Pinaud, B. A.; Chen, Z. B.; Clemens, B. M.; Jaramillo, T. F.; Brongersma, M. L. *Nano Lett*. **2011**, *11*, 3440–3446.

[73] Atwater, H. A.; Polman, A. *Nat. Mater.* **2010**, *9*, 205–213.

[74] Catchpole, K. R.; Polman, A. *Appl. Phys. Lett*. **2008**, *93*, 191113.

[75] Han, F.; Kambala, V. S. R.; Srinivasan, M.; Rajarathnam, D.; Naidu, R. *Appl. Catal. A* **2009**, *359*, 25–40.

[76] Kumar, S. G.; Devi, L. G. *J. Phys. Chem. A* **2011**, *115*, 13211–13241.

[77] Zhang, L. W.; Mohamed, H. H.; Dillert, R.; Bahnemann, D. *J. Photochem. Photobiol. C* **2012**, *13*, 263–276.

[78] Yang, J. H.; Wang, D. G.; Han, H. X.; Li, C. *Acc. Chem. Res.* **2013**, *46*, 1900–1909.

[79] Lee, J.; Javed, T.; Skeini, T.; Govorov, A. O.; Bryant, G. W.; Kotov, N. A. *Angew. Chem. Int. Ed.* **2006**, *45*, 4819–4823.

[80] Sönnichsen, C.; Franzl, T.; Wilk, T.; Plessen, G.; Feldmann, J. *Phys. Rev. Lett.* **2002**, *88*, 077402.

[81] Silva, C. G.; Juárez, R.; Marino, T.; Molinari, R.; García, H. *J. Am. Chem. Soc.* **2011**, *133*, 595–602.

[82] Primo, A.; Matino, T.; Corma, A.; Molimari, R.; García, H. *J. Am. Chem. Soc.* **2011**, *133*, 6930–6933.

[83] Naya, S.-I.; Inoue, A.; Tada, H. *J. Am. Chem. Soc.* **2010**, *132*, 6292–6293.

[84] Pan, Z. W.; Lu, Y.-Y.; Liu, F. *Nat. Chem.* **2011**, *3*, 467–472.

[85] Lindstrom, C. D.; Zhu, X.-Y. *Chem. Rev.* **2006**, *106*, 4281–4300.

[86] Yablonovitch, E.; Cody, G. D. *IEEE Trans. Electr. Dev.* **1982**, *29*, 300–305.

[87] Deckman, H. W.; Roxlo, C. B.; Yablonovitch, E. *Opt. Lett*. **1983**, *8*, 491–493.

[88] Stuart, H. R.; Hall, D. G. *Appl. Phys. Lett*. **1996**, *69*, 2327–2329.

[89] Stuart, H. R.; Hall, D. G.   *Appl. Phys. Lett*. **1998**, *73*, 3815–3817.

[90] Kulkarni, A. P.; Noone, K. M.; Munechika, K.; Guyer, S. R.; Ginger, D. S. *Nano Lett.* **2010**, *10*, 1501–1505.

[91] Stavytska-Barba, M.; Salvafor, M.; Kulkarni, A.; Ginger, D. S.; Kelly, M. *J. Phys. Chem. C* **2011**, *115*, 20788–20794.

[92] Ding, B.; Lee, B. J.; Yang, M. J.; Jung, H. S.; Lee, J.-K. *Adv. Energy Mater.* **2011**, *1*, 415–421.

[93] Liu, Y.-G.; Hsu, Y.-K.; Chen, Y.-C.; Wang, S.-B.; Miller, J. T.; Chen, L.-C.; Chen, K.-H. *Energy Environ. Sci.* **2012**, *5*, 8917–8922.

[94] Kim, S.-S.; Na, S.-I.; Jo, J.; Kim, D.-Y.; Nah, Y.-C. *Appl. Phys. Lett.* **2008**, *93*, 073307.

[95] Chen, X.; Zhao, C.; Rothberg, L.; Ng, M.-K. *Appl. Phys. Lett.* **2008**, *93*, 123302.

[96] Naidu, B. V. K.; Park, J. S.; Kim, S. C.; Park, S.-M.; Lee, E.-J.; Yoon, K.-J.; Lee, S. J.; Lee, J. W.; Gal, Y.-S.; Jin, S.-H. *Sol. Energy Mater. Sol. Cells* **2008**, *92*, 397–401.

[97] Chen, F.-C.; Wu, J.-L.; Lee, C.-L.; Hong, Y.; Kuo, C.-H.; Huang, M. H. *Appl. Phys. Lett.* **2009**, *95*, 013305.

[98] Wu, J.-L.; Chen, F.-C.; Hsiao, Y.-S.; Chien, F.-C.; Chen, P.; Kuo, C.-H.; Huang, M. H.; Hsu, C.-S. *ACS Nano* **2011**, *5*, 959–967.

[99] Wang, D. H.; Kim, D. Y.; Choi, K. W.; Seo, J. H.; Im, S. H.; Park, J. K.; Park, O. O.; Heeger, A. J. *Angew. Chem. Int. Ed.* **2011**, *50*, 5519–5523.

[100] Morfa, A. J.; Rowlen, K. L.; Reilly, T. H.; Romero, M. J.; Van de Lagemaat, J. *Appl. Phys. Lett.* **2008**, *92*, 013504.

[101] Lindquist, N. C.; Luhman, W. A.; Oh, S. H.; Holmes, R. J. *Appl. Phys. Lett.* **2008**, *93*, 123308.

[102] Yang, J.; You, J. B.; Chen, C.-C.; Hsu, W.-C.; Tan, H.-R.; Zhang, X. W.; Hong, Z.; Yang, Y. *ACS Nano* **2011**, *5*, 6210–6217.

[103] Hagglund, C.; Zach, M.; Kasemo, B. *Appl. Phys. Lett.* **2008**, *92*, 013113.

[104] Standridge, S. D.; Schartz, G. C.; Hupp, J. T.; *Langmuir* **2009**, *25*, 2569–2600.

[105] Wen, C.; Ishikawa, K.; Kishima, M.; Yamade, K. *Sol. Energy Mater. Sol. Cells*

2000, *61*, 339–351.

[106] Brown, M. D.; Suteewong, T.; Kumar, R. S.; D'Innovenzo, V.; Petrozza, A.; Lee, M. M.; Wiesner, U.; Snaith, H. J. *Nano Lett* **2011**, *11*, 438–445.

[107] Gangishetty, M. K.; Lee, K. E.; Scott, R. W. J.; Kelly, T. L. *ACS Appl. Mater. Interfaces* **2013**, *5*, 11044–11051.

[108] Wooh, S.; Lee, Y.-G.; Tahir, M. N.; Song, D.; Meister, M.; Laquai, F.; Tremel, W.; Bisquert, J.; Kang, Y. S.; Char, K. *J. Mater. Chem. A* **2013**, *1*, 12627–12634.

[109] Qi, J. F.; Dang, X. N.; Hammond, P. T.; Belcher, A. M. *ACS Nano* **2011**, *9*, 7108–7116.

[110] Chen, C. C.; Ma, W. H.; Zhao J. C. *Chem. Soc. Rev.* **2010**, *39*, 4206–4219.

[111] Tanaka, A.; Ogino, A.; Iwaki, M.; Hashimoto, K.; Ohnuma, A.; Amano, F.; Ohtani, B.; Kominami, H. *Langmuir* **2012**, *28*, 13105–13111.

[112] Zhang, H, M.; Liang, C. H.; Liu, J.; Tian, Z. F.; Wang, Z. F.; Cai, W. P. *Langmuir* **2012**, *28*, 3938–3944.

[113] Xiang, Q. J.; Yu, J. G.; Cheng, B.; Ong, H. C. *Chem. Asian J.* **2010**, *5*, 1466–1474.

[114] Qu, Y. Q.; Cheng, R.; Su, Q.; Duan, X. F. *J. Am. Chem. Soc.* **2011**, *133*, 16730–16733.

[115] Pan, Y. L.; Deng, S. Z.; Polavarapu, L.; Gao, N. Y.; Yuan, P. Y.; Sow, C. H.; Xu, Q.-H. *Langmuir* **2012**, *28*, 12304–12310.

[116] Kochuveedu, S. T.; Kim D.-P.; Kim, D. H. *J. Phys. Chem. C* **2012**, *116*, 2500–2506.

[117] Wen, Y. Y.; Ding, H. M.; Shan, Y. K. *Nanoscale* **2011**, *3*, 4411–4417.

[118] Logar, M.; Jančar, B.; Šturm S.; Suvorov, D. *Langmuir* **2010**, *26*, 12215–12224.

[119] Zhang, Q.; Lima, D. Q.; Lee, I.; Zaera, F.; Chi, M. F.; Yin, Y. D. *Angew. Chem. Int. Ed.* **2011**, *50*, 7088–7092.

[120] Zhang, J.; Li, L. P.; Yan T. J.; Li, G. S. *J. Phys. Chem. C* **2011**, *115*, 13820–13828.

[121] Wang, P.; Huang, B. B.; Zhang, X. Y.; Qin, X. Y.; Jin, H.; Dai, Y.; Wang, Z. Y.;

Wei, J. Y.; Zhan, J.; Wang, S. Y.; Wang, J. P.; Whangbo, M.-H. *Chem. Eur. J.* **2009**, *15*, 1821–1824.

[122] Hu, C.; Peng, T. W.; Hu, X. X.; Nie, Y. L.; Zhou, X. F.; Qu, J. H.; He, H. *J. Am. Chem. Soc.* **2010**, *132*, 857–862.

[123] An, C. H.; Wang, R. P.; Wang, S. T.; Zhang, X. Y. *J. Mater. Chem.* **2011**, *21*, 11532–11536.

[124] Zhu, M. S.; Chen, P. L.; Liu, M. H. *ACS Nano* **2011**, *5*, 4529–4536

[125] Kuai, L.; Geng, B. Y.; Chen, X. T.; Zhao, Y. Y.; Luo Y. C. *Langmuir* **2010**, *26*, 18723–18727.

[126] Lan, J. Y.; Zhou, X. M.; Liu, G.; Yu, J. G.; Zhang, J. C.; Zhi, L. J.; Nie, G. J. *Nanoscale* **2011**, *3*, 5161–5167.

[127] Sun, S. M.; Wang, W. Z.; Zhang, L.; Shang, M.; Wang, L. *Catal. Commun.* **2009**, *11*, 290–293.

[128] Chen, X.; Zhu, H.-Y.; Zhao, J.-C.; Zheng, Z.-F.; Gao X.-P. *Angew. Chem. Int. Ed.* **2008**, *47*, 5353–5356.

[129] Hughes, M. D.; Xu, Y.-J.; Jenkins, P.; McMorn, P.; Landon, P.; Enache, D. I.; Carley, A. F.; Attard, G. A.; Hutchings, G. J.; King, F.; Stitt, E. H.; Johnston, P.; Griffin, K.; Kiley, C. J. *Nature* **2005**, *437*, 1132–1135.

[130] Jin, Z.; Xiao, M. D.; Bao, Z. H.; Wang, P. *Angew. Chem. Int. Ed*. **2012**, *51*, 6404–6410.

[131] Su, R.; Tiruvalam, R.; He, Q.; Dimitratos, N.; Kesavan, L.; Hammond, C.; Lopez-Sanchez, J. A.; Bechstein, R.; Kiely, C. J.; Hutchings, G. J.; Besenbacher, F. *ACS Nano* **2012**, *6*, 6284–6292.

[132] Joseph, V.; Engelbrekt, C.; Zhang, J. D.; Gernert, U.; Ulstrup, J.; Kneipp, J. *Angew. Chem. Int. Ed*. **2012**, *51*, 7592–7596.

[133] Li, C. C.; Zheng, Y. P.; Wang, T. H. *J. Mater. Chem.* **2012**, *22*, 13216–13222.

[134] Kimura, K.; Naya, S.-i, Jin-nouchi, Y.; Tada, H. *J. Phys. Chem. C*. **2012**, *116*, 7111–7117.

[135] Kowalska, E.; Abe, R.; Ohtani, B. *Chem. Commun*. **2009**, 241–243.

[136] Kowalska, E.; Mahaney, O. O.; Abe, R.; Ohtani, B. *Phys. Chem. Chem. Phys*. **2010**, *12*, 2344–2355.

[137] Tanaka, A.; Hashimoto, K.; Kominami, H. *Chem. Commun*. **2011**, *47*, 10446–10448.

[138] Hallett-Tapley, G. L.; Silvero, M. J.; González-Béjar, M.; Grenier, M.; Netto-Ferreira, J. C.; Scaiano, J. C. *J. Phys. Chem. C*. **2011**, *115*, 10784–10790.

[139] Mori, K.; Kawashima, M.; Che, M.; Yamashita, H. *Angew. Chem. Int. Ed.* **2010**, *49*, 8598–8601.

[140] Wang, F.; Li, C. H.; Chen, H. J.; Jiang, R. B.; Sun, L.-D.; Li, Q. Wang, J. F.; Yu, J. C.; Yan, C.-H. *J. Am. Chem. Soc*. **2013**, *135*, 5588–5601.

[141] Fujishima, A.; Honda, K. *Nature*, **1972**, *238*, 37–38.

[142] Rosseler, O.; Shankar, M. V.; Du, M. K.-L. Schmidlin, L.; Keller, N.; Keller, V. *J. Catal.* **2010**, *269*, 179–190.

[143] Li, J. T.; Cushing, S. K.; Zheng, P.; Meng, F.; Chu, D.; Wu, N. Q. *Nat. Commun*. **2013**, *4*, 2651.

[144] Chen, H. M.; Chen, C. K.; Chen, C.-J.; Cheng, L.-C.; Wu, P. C.; Cheng, B. H.; Ho, Y. Z.; Tseng, M. L.; Hsu, Y.-Y.; Chan, T.-S.; Lee, J.-F.; Liu, R.-S.; Tsai, D. P. *ACS Nano* **2012**, *6*, 7362–7372.

[145] Liu, Z. W.; Hou, W. B.; Pavaskar, P.; Aykol, M.; Cronin, S. B. *Nano Lett*. **2011**, *11*, 1111–1116.

[146] Ingram, D. B.; Linic, S. *J. Am. Soc. Chem.* **2011**, *133*, 5202–5205.

[147] Pu, Y.-C.; Wang, G. M.; Chang, K.-D.; Ling, Y. C.; Lin, Y.-K.; Fitzmorris, B. C.; Liu, C.-M.; Lu, X. H.; Tong, Y. X.; Zhang, J. Z.; Hsu, Y.-J.; Li, Y. *Nano Lett*. **2013**, *13*, 3817–3823.

[148] Hou, W. B.; Cronin, S. B. *Adv. Funt. Mater*. **2013**, *23*, 1612–1619.

[149] Liu, E. Z.; Kang, L. M.; Yang, Y. H.; Sun, T.; Hu, X. Y.; Zhu, C. J.; Liu, H. C.; Wang, Q. P.; Li, X. H.; Fan, J. *Nanotechnology* **2014**, *25*, 165401.

[150] Oros-Ruiz, S.; Zanella, R.; López, R.; Hernández-Gordillo, A.; Gómez, R. *J. Hazardous Mater*. **2013**, *263*, 2–10.

[151] Zheng, Z. K.; Tachikawa, T.; Majima, T. *J. Am. Chem. Soc.* **2014**, *136*, 6870–6873.

[152] Zhang, L.; Blom, D. A.; Wang, H. *Chem. Mater.* **2011**, *23*, 4587–4598.

[153] Kuo, C.-H.; Hua, T.-E.; Huang, M. H. *J. Am. Chem. Soc.* **2009**, *131*, 17871–17878.

[154] Liu, D. Y.; Ding, S.-Y.; Liu, H.-X.; Liu, B.-J.; Ye, Z.-Z.; Fan, F.-R.; Ren, B.; Tian, Z.-Q. *J. Phys. Chem. C* **2012**, *116*, 4477–4483.

[155] Kong, L. N.; Chen, W.; Ma, D.; Yang, K. Y.; Liu, S. S.; Huang, S. M. *J. Mater. Chem.* **2012**, *22*, 719–724.

[156] Sun, Z. H.; Yang, Z.; Yeung, M. H.; Ni, W. H.; Wu, H. K.; Wang, J. F. *Angew. Chem. Int. Ed.* **2009**, *48*, 2881–2885.

[157] Meir, N.; Plante, I. J.; Flomin, K.; Chockler, E.; Moshofsky, B.; Diab, M.; Volokh, M.; Mokri, T. *J. Mater. Chem. A* **2013**, *1*, 1763–1769.

[158] Wang, H. H.; Sun, Z. H.; Lu, Q. H.; Zeng, F. W.; Su, D. S. *Small*, **2012**, *8*, 1167–1172.

[159] Seh, Z. W.; Liu, S. H.; Zhang, S.-Y.; Shah, K. W.; Han, M.-Y. *Chem. Commun.* **2011**, *47*, 6689–6691.

[160] Seh, Z. W.; Liu, S. H.; Zhang, S.-Y.; Bharathi, M. S.; Ramanarayan, H.; Low, M.; Shah, K. W.; Zhang, Y.-W.; Han, M.-Y. *Angew. Chem. Int. Ed.* **2011**, *50*, 10140–10143.

[161] Abdulla-Al-Mamun, M.; Kusumoto, Y.; Zannat, T.; Horie, Y.; Manaka, H. *RSC Adv.* **2013**, *3*, 7816–7827.

[162] Shen, J. H.; Zhu, Y. H.; Yang, X. L.; Zong, J.; Li, C. Z. *Langmuir* **2013**, *29*, 690–695.

[163] Wang, H.; Brandl, D. W.; Le, F.; Nordland, P.; Halas, N. J. *Nano Lett.* **2006**, *6*, 827–832.

[164] Tom, R. T.; Nair, A. S.; Singh, N.; Aslam, M.; Nagendra, C. L.; Philip, R.; Vijayamohanan, K.; Pradeep, T. *Langmuir*, 2003, 19. 3439–3445.

[165] Pastoriza-Santos, I.; Koktysh, D. S.; Mamedov, A. A.; Giersig, M.; Kotov, N.

A.; Liz-Marzán;L. M. *Langmuir* **2000**, *16*, 2731–2735.

[166] Wu, X.-F.; Song, H.-Y.; Yoon, J.-M.; Yu, Y.-T.; Chen, Y.-F. *Langmuir* **2009**, *25*, 6438–6447.

[167] Jiang, F. R.; Tian, Q. W.; Tang, M. H.; Chen, Z. G.; Yang, J. M.; Hu, J. Q. *CrystEngComm* **2011**, *13*, 7189–7193.

[168] Zhang, Y. X.; Ding, H. L.; Liu, Y. Y.; Pan, S. S.; Luo, Y. Y.; Li, G. H. *J. Mater. Chem.* **2012**, *22*, 10779–10786.

[169] Hirakawa, T.; Kamat, P. V. *J. Am. Chem. Soc.* **2005**, *127*, 3928–3934.

[170] Zhang, N.; Liu, S. Q.; Fu, X. Z.; Xu, Y.-J. *J. Phys. Chem. C* **2011**, *115*, 9136–9145.

[171] Zeng, J.; Tao, J.; Su, D.; Zhu, Y. M.; Qin, D.; Xia, Y. N. *Nano Lett.* **2011**, *11*, 3010–3012.

[172] Liu, B.; Ma, Z. F. *Small* **2011**, *7*, 1587–1592.

[173] Levard, C.; Hotze, E. M.; Colman, B. P.; Dale, A. L.; Truong, L.; Yang, X. Y.; Bone, A. J.; Jr., G. E. B.; Tanguay, R. L.; Giulio, R. T. D.; Bernhardt, E. S.; Meyer, J. N.; Wiesner, M. R.; Lowry, G. V. *Environ. Sci. Technol.* **2013**, *47*, 13440–13448.

[174] Sun, J.-L.; Zhu, J.-L.; Zhao, X. C.; Bao, Y. *Nanotechnology* **2011**, *22*, 035202.

[175] Fu, X. F.; Zou, H. M.; Zhou, L. *J. Nanoscience and Nanotechnology* **2010**, *10*, 5851–5856.

[176] Seo, D.; Yoo, C. I.; Jung, J.; Song, H. *J. Am. Chem. Soc.* **2008**, *130*, 2940–2941.

[177] Xu, L.; Yin, Z. Y.; Cao, S.-W.; Fan, Z. X.; Zhang, X.; Zhang, H.; Xue, C. *Chem. Eur. J.* **2014**, *20*, 2742–2745.

[178] Park, G.; Lee, C.; Seo, D.; Song, H. *Langmuir* **2012**, *28*, 9003–9009.

[179] Zhu, J. M.; Shen, Y. H.; Xie, A. J.; Zhu, L. *J. Mater. Chem.* **2009**, 19, 8871–8875.

[180] Liu, M. Z.; Guyot-Sionnest, P. *J. Mater. Chem.* **2006**, *16*, 3942–3945.

[181] Li, M.; Yu, X.-F.; Liang, S.; Peng, X.-N.; Yang, Z.-J.; Wang, Y.-L.; Wang, Q.-Q. *Adv. Funt. Mater.* **2011**, *21*, 1788–1794.

[182] She, Z. W.; Liu, S. H.; Low, M.; Zhang, S.-Y.; Liu, Z. L.; Mayah, A.; Han, M.-Y. *Adv. Mater.* **2012**, *24*, 2310–2314.

[183] Maaroof, A. I.; Cho, D.-G.; Kim, B.-J.; Kim, H.-T.; Hong, S. *J. Phys. Chem. C* **2013**, *117*, 19601–19605.

[184] Chen, H. J.; Shao, L.; Man, Y. C.; Zhao, C. M.; Wang, J. F.; Yang, B. C. *Small* **2012**, *8*, 1503–1509.

[185] Fan, J. A.; Bao, K.; Wu, C.; Bao, J. M.; Bardhan, R.; Halas, N. J.; Manoharan, V. N.; Shvets, G.; Nordlander, P.; Capasso, F. *Nano Lett.* **2010**, *10*, 4680–4685.

[186] Du, J.; Qi, J.; Wang, D.; Tang, Z. Y. *Energy Environ. Sci.* **2012**, *5*, 6914–6918.

[187] Chang, S.; Li, Q.; Xiao, X. D.; Wong, K. Y.; Chen, T. E*nergy Environ. Sci.* **2012**, *5*, 9444–9448.

[188] Dang, X. N.; Qi, J. F.; Klug, M. T.; Chen, P.-Y.; Yun, D. S.; Fang, N. X.; Hammond, P. T.; Belcher, A. M. *Nano Lett.* **2013**, *13*, 637–642.

[189] Standrige, S. D.; Schatz, G. C.; Hupp, J. T. *J. Am. Chem. Soc.* **2009**, *131*, 8407–8409.

[190] Wu, X.-F.; Song, H.-Y.; Yoon, J.-M.; Yu, Y.-T.; Chen, Y.-F. *Langmuir* **2009**, *25*, 6438–6447.

[191] Ye, M. M.; Zhou, H. H.; Zhang, T. Q.; Zhang, Y. P.; Shao, Y. *Chem. Eng. J.* **2013**, *226*, 209–216.

[192] Kim, Y.; Park, K. Y.; Jang, D. M.; Song, Y. M.; Kim, H. S.; Cho, Y. J.; Myung, Y.; Park, J. *J. Phys. Chem. C* **2010**, *114*, 22141–22146.

[193] Aguirre, M. E.; Rodríguez, H. B.; Román, E. S.; Feldhoff, A.; Grela, M. A. *J. Phys. Chem. C* **2011**, *115*, 24967–24974.

[194] Zhang, X. Q.; Zhu, Y. H.; Yang, X. L.; Wang, S. W.; Shen, J. H.; Lin, B. B.; Li, C. Z. *Nanoscale* **2013**, *5*, 3359–3366.

[195] Lee, J.; Mubeen, S.; Ji, X. L.; Stucky, G. D.; Moskovits, M. *Nano Lett.* **2012**, *12*, 5014–5109.

[196] Warren, S. C.; Thimsen, E. *Energy Environ. Sci.* **2012**, *5*, 5133–5146.

[197] Zhou, N.; Polavarapu, L.; Gao, N. Y.; Pan, Y. L.; Yuan, P. Y.; Wang, Q.; Xu,

Q.-H. *Nanoscale* **2013**, *5*, 4236–4241.

[198] Mubeen, S.; Lee, J.; Singh, N.; Krämer, S.; Stucky, G. D.; Moskovits, M. *Nat. Nanotechnol.* **2013**, *8*, 247–251.

Chapter 2

Growth of Noble Metal Nanocrystals and Characterization Techniques

The noble metal nanocrystals I used during my thesis study include both monometallic and bimetallic nanocrystals, such as Au nanorods with different longitudinal surface plasmon wavelengths (LSPWs), Au nanospheres, Ag nanocubes, porous and cubic Pd nanocrystals, porous Pt nanocrystals, (Au nanorod core)/(Pd shell) with continuous/discontinuous Pd, and (Au nanorod core)/(Pt shell) nanocrystals. I will introduce their detailed growth processes in *Section 2.1*. In *Section 2.2*, I will present the techniques that are used to characterize the morphology, structure, and plasmonic properties of the (metal core)/(semiconductor shell) nanostructures in this thesis, which are spectrophotometry, electron microscopes, and single-particle scattering imaging/spectroscopy. The fabrication and characterization techniques of dye-sensitized solar cells that are utilized to examine the plasmon-enhanced solar harvesting applications of our (Au core)/(TiO$_2$ shell) nanostructures will also be presented in this section. In addition, the simulation method involved in the sulfidation of Ag nanocubes will be introduced in *Section 2.2*.

2.1 Growth of Noble Metal Nanocrystals

Au nanorods and nanospheres

Au nanorod samples with various LSPWs were prepared through a seed-mediated method [1] together with anisotropic oxidation [2,3]. Specifically, the seed solution was made by injecting a freshly prepared, ice-cold aqueous NaBH$_4$ solution (0.01 M, 0.6 mL) into an aqueous mixture composed of HAuCl$_4$ (0.01 M, 0.25 mL) and

cetyltrimethylammonium bromide (CTAB, 0.1 M, 9.75 mL), followed by rapid inversion mixing for 2 min. The resultant seed solution was kept at room temperature for more than 2 h before use. The growth solution was prepared by sequential addition of aqueous $HAuCl_4$ (0.01 M, 2 mL), $AgNO_3$ (0.01 M, 0.4 mL), HCl (1.0 M, 0.8 mL), and ascorbic acid (AA, 0.1 M, 0.32 mL) into an aqueous CTAB solution (0.1 M, 40 mL). The resulting solution was mixed for 30 s, followed by quick injection of a certain amount of the seed solution. The reaction solution was gently inversion-mixed for 2 min and then left undisturbed overnight. By varying the added amount of the seed solution, Au nanorods with different LSPWs can be grown. For example, Au nanorods with their LSPW around 800 nm were grown by injecting 0.1 mL of the seed solution. Similarly, Au nanorods with their LSPW around 700, 750, 850, and 900 nm were obtained by changing the amount of the seed solution to 0.01, 0.015, 0.15, and 0.2 mL, respectively. Au nanorods with shorter LSPWs (<700 nm) can be obtained using anisotropic oxidation, which was realized by adding HCl (1.0 M, 0.2 mL) and H_2O_2 (30 wt%, 0.05 mL) into the starting pre-grown Au nanorod solution (40 mL). The mixture was thereafter kept at 65 °C to expedite the oxidation reaction. The LSPWs were monitored in real time. The nanorod samples were washed twice by centrifugation and then redispersed into CTAB (0.1 M) solutions to remove excess H_2O_2 and HCl.

The Au nanosphere sample was also prepared following a seed-mediated method [4]. Typically, the seeds were made by the addition of a freshly prepared, ice-cold $NaBH_4$ solution (0.01 M, 0.6 mL) into a mixture of $HAuCl_4$ (0.01 M, 0.25 mL) and CTAB (0.1 M, 7.5 mL). The resultant solution was mixed by rapid inversion for 30 s and then kept for 1 h before use at room temperature. The growth solution was prepared by the sequential addition of $HAuCl_4$ (0.01 M, 0.8 mL), CTAB (0.1 M, 6.4 mL), and AA (0.1 M, 3.8 mL) into water (32 mL). The seed solution (40 μL) was then added into the growth solution. The resultant mixture was mixed by gentle inversion for 10 s and left undisturbed overnight.

Ag nanocubes

The Ag nanocube sample was grown by following a previously reported procedure [5]. Typically, $CuCl_2$ (60 mM) and poly(vinylpyrrolidone) (PVP, molecular weight: 55000, 6 mM in terms of the polymer) solutions were first prepared separately by dissolving $CuCl_2$ and PVP in pentanediol completely through ultrasonication and vortexing. A silver precursor solution was made by dissolving $AgNO_3$ (1.2 mmol) in pentanediol (10 mL), followed by the addition of the pre-prepared $CuCl_2$ solution (20 μL). Another portion of pentanediol (20 mL) was then added into a 250 mL, three-necked, round-bottom flask and heated to 190 °C in an oil bath. The premade $AgNO_3$ and PVP solutions were alternatively injected into the flask at regular intervals, with the mixture solution in the flask kept at 190 °C. The $AgNO_3$ solution was quickly injected at 0.5 mL every minute, while the PVP solution was added dropwise at 0.25 mL every 30 s. When the addition process was completed, the reaction was quickly stopped by taking the flask out of the oil bath and placing it in an ice-cold water bath. The as-grown Ag nanocube sample was washed three times with an ethanol/water mixture (1:1 by volume) by centrifugation before further use.

Porous Pd nanocrystals

The porous Pd nanocrystal sample was made according to a reported method [6]. Briefly, the seed solution was made by rapidly injecting $NaBH_4$ (0.01 M, 0.6 mL) into the mixture of cetyltrimethylammonium chloride (CTAC, 25 wt%, 1.25 mL), water (7.5 mL), H_2PdCl_4 (0.01 M, 0.25 mL), and NaOH (0.1 M, 0.30 mL). For the growth solution, water (38.8 mL), CTAC (25 wt%, 0.24 mL), H_2PdCl_4 (0.01 M, 1.2 mL), and NaOH (0.1 M, 0.3 mL) were mixed. The seed solution (40 μL) was injected quickly, followed by the addition of AA (0.1 M, 0.4 mL). The resultant mixture was gently inversed for 30 s and left at room temperature for 8 h.

Cubic Pd nanocrystals

The cubic Pd nanocrystal sample was grown following the method described in a previous report [7]. Briefly, CTAB (0.1 M, 7.5 mL), water (52.5 mL), and H_2PdCl_4 (0.01 M, 3.0 mL) were mixed in a glass bottle. The mixture was kept at 80 °C with stirring for 5 min in an oil bath, following by quick injection of AA (0.1 M, 0.48 mL). After being kept under stirring for 2 h, the mixture was cooled to room temperature naturally.

Porous Pt nanocrystals

The porous Pt nanocrystal sample was prepared following the reported method [8]. The mixture of CTAB (0.1 M, 5.0 mL) and K_2PtCl_4 (0.01 M, 2.0 mL) was heated to 70 °C for about 10 min until the solution became clear. AA (0.02 M, 3.0 mL) was then added. The resultant mixture was kept at 70 °C for 8 h.

(Au nanorod)/(Pd shell) with continuous/discontinuous Pd shell nanostructures

The (Au nanorod)/(Pd shell) sample with continuous/discontinuous Pd shell was grown following a reported method [9]. For the growth of continuous Pd shell, the Au nanorod solution (10 mL) was centrifuged and redispersed into 10 mL water, followed by the sequential addition of CTAB (0.1 M, 10 mL), water (30 mL), H_2PdCl_4 (0.01 M, 0.5 mL), and AA (0.1 M, 0.25 mL). The mixture was left undisturbed overnight. The Au/Pd sample with discontinuous Pd shell was grown following the similar procedure by changing CTAB to CTAC (0.1 M, 10 mL).

(Au nanorod)/(Pt shell) nanocrystals

The (Au nanorod)/(Pt shell) nanocrystal sample was prepared by a method modified from the reported procedure [10]. The Au nanorod solution (10 mL) was centrifuged and redispersed into 10 mL water. Water (20 mL), CTAB (0.1 M, 0.4 mL), AA (0.1 M, 2.0 mL), and H_2PtCl_4 (0.01 M, 2.0 mL) were then sequentially added,

followed by gentle inversion for 30 s. The mixture was kept at 65 °C for 8 h.

Hollow TiO₂ Nanostructures

Hollow TiO₂ nanostructure sample was obtained from oxidative etching of the Au nanorod core of the (Au nanorod core)/(TiO₂ shell) nanostructures that were prepared following our method. Typically, the core/shell nanostructure sample (10 mL) was centrifuged once and redispersed into water (0.5 mL). The iodide-based liquid electrolyte (Dyesol, EL-HPE, 0.1 M LiI, 50 mM I₂, and 0.6 M 1,2-dimethyl-3-propylimidazolium iodide in acetonitrile/valeronitrile [85/15, v/v]) used in the fabrication of the DSSCs was employed as the etching solution. After the etching solution (20 μL) was introduced under shaking, the mixture was kept still for ~48 h to allow for the complete etching of the Au nanorod cores. The hollow TiO₂ nanostructures were washed with water by centrifugation at least four times before further use

2.2 Characterization and Simulation Techniques

Characterization techniques

The characterization techniques employed to investigate the optical properties and structure of (plasmonic metal core)/(semiconductor shell) nanostructures are described here. The optical properties of the nanostructures were studied by measuring the extinction of the ensemble samples or acquiring their single-particle scattering spectra. The extinction spectra were recorded on a Hitachi U-3501 UV–visible–NIR spectrophotometer. Specifically, the extinction can be determined by the measured transmissivity (T) that can be described by the following equation [11]:

$$T = \frac{I}{I_0} = \exp\left(-N\sigma_{\text{ext}}l\right)$$

where I and I_0 are the intensities of the transmitted and the incident light, N is the number density of the nanoparticles, σ_{ext} is the extinction cross-section of a single nanoparticle, and l is the optical path length. In my studies, l is set at 0.5 cm for all involved nanostructure solutions. The extinction E can be acquired directly on the Hitachi U-3501 spectrophotometer.

$$E = -\log\left(\frac{I}{I_0}\right) = -\log T = \frac{N\sigma_{ext}l}{\ln 10} = n\varepsilon l$$

where n is the molar concentration and ε is the molar extinction coefficient. The value of ε for some nanostructures have already been reported [3,12]. The molar concentrations of the nanoparticles can be estimated on the basis of their measured extinction spectra.

Single-particle dark-field scattering spectra of individual nanostructures were acquired on a dark-field optical microscope (Olympus BX60) that was integrated with a quartz–tungsten–halogen lamp (100 W), a monochromator (Acton SpectraPro 2300i), and a charge-coupled device camera (Princeton Instruments Pixis 512B). During the measurements, the camera was thermoelectrically cooled to –70 °C. A dark-field objective (50×, numerical aperture = 0.5) was employed for both illuminating the nanostructures with white light and collecting scattered light. The scattering spectrum from an individual nanostructure was corrected by first subtracting the background spectrum taken from the adjacent region without nanostructures and then dividing it with a calibrated response curve of the entire optical system.

The structure and morphology of the nanoparticles were characterized by electrons microscopes. Scanning electron microscopy imaging was carried out on an FEI Quanta 400 FEG microscope. Low-magnification transmission electron microscopy imaging was performed on an FEI Tecnai Spirit microscope and a FEI CM120 operating at 120 kV. The X-ray diffraction patterns were acquired on a Rigaku SmartLab diffractometer equipped with Cu Kα radiation. Elemental mapping, line

profiling, and high-angle annular dark-field scanning transmission electron microscopy imaging were carried out on an FEI Tecnai F20 microscope equipped with an Oxford EDX analysis system. X-ray photoelectron spectroscopy spectrum was performed on Thermo-VG scientific ESCALAB 250. Fluorescence spectra were carried out on a Hitachi F-4500 spectrofluorometer.

The performance of dye-sensitized solar cells was characterized by measuring the current–voltage curves, the (incident photon)-to-electron conversion efficiency (IPCE), dye loading, and the electrochemical impedance spectroscopy (EIS). The current–voltage curves of dye-sensitized solar cells were measured with a semiconductor characterization system (Keithley 236) at room temperature in air. The light illumination was from a solar simulator (Newport) with an AM 1.5G filter at 100 mW cm^{-2}. IPCE measurements were made on a Solar Cell QE/IPCE Measurement System (Zolix Solar Cell Scan 100) under the DC mode. Dye absorption spectra that were used to determine the dye loading amount were measured on a Hitachi U-3501 UV–visible–NIR spectrophotometer. EIS curves were recorded in dark by applying a bias of 700 mV over a frequency range of 0.1–10^5 Hz and at an AC amplitude of 10 mV. The solar-cell parameters were calculated with Z-View software (v2.1b, Scribner Associates, Inc.).

Simulation techniques

The finite-difference time-domain (FDTD) simulation technique that was used to reveal the nature of the plasmon modes of Ag nanocubes and the spectral evolution during the formation of Ag/Ag$_2$S nanocubes in Chapter 4 was described here. The FDTD simulation, performed in the time domain [13,14], is an explicit time marching algorithm used to solve Maxwell's curl equations on a discrete spatial grid. It can be used to investigate both the far- and near-field electromagnetic responses of homogeneous or heterogeneous materials with arbitrary geometries. The approach has successfully been applied to many nanoscale systems in the past [13,14,15–18].

During my thesis study in the sulfidation of Ag nanocubes, which will be described in Chapter 4, the simulations were performed using FDTD Solution 7.5 developed by Lumerical Solutions, Inc. An electromagnetic pulse in the wavelength range from 300 nm to 1000 nm was launched into a box containing the target nanostructure to simulate a propagating plane wave interacting with the nanostructure. The nanostructure and its surrounding medium inside the box were divided into meshes of 0.5 nm in size. The refractive index of the surrounding medium was set to be 1.33, which is the index of water. The dielectric functions used in the simulations were formulated using the previously reported data for Ag_2S and Johnson and Christy data for Ag [19]. The charge distributions were calculated from the electric field contours using the FDTD software. The size of the Ag nanocube was set to 93 nm according to the average size measured from the TEM images. The as-grown Ag nanocube was assumed to have sharp edges and vertices. The sulfidation process was modeled in two ways. First, the Ag nanocube was truncated gradually until it became a nanosphere, followed with decreases in diameter step-by-step. The radius for the truncation of the edges and vertices was increased at 6 nm per step. After the Ag core was truncated into a nanosphere, its diameter was reduced at 12 nm per step until the Ag core was completely consumed. Second, the Ag nanocube was modeled to keep its original cubic shape, with its edge length being shrunk at 6 nm. Throughout the sulfidation process, the reacted volume of the Ag nanocube was replaced with Ag_2S. The entire nanostructure was kept as a cube.

References

[1] Ming, T.; Kou, X. S.; Chen, H. J.; Wang, T.; Tam, H.-L.; Cheah, K.-W.; Chen, J.-Y.; Wang, J. F. *Angew. Chem. Int. Ed.* **2008**, *47*, 9685–9690.

[2] Tsung, C.-K.; Kou, X. S.; Shi, Q. H.; Zhang, J. P.; Yeung, M. H.; Wang, J. F.; Stucky, G. D. *J. Am. Chem. Soc.* **2006**, *128*, 5352–5353.

[3] Ni, W. H., Kou, X. S.; Yang, Z.; Wang, J. F. *ACS Nano* **2008**, *2*, 677–686.

[4] Chen, H. J.; Shao, L.; Man, Y. C.; Zhao, C. M.; Wang, J. F.; Yang, B. C. *Small* **2012**, *8*, 1503–1509..

[5] Tao, A.; Sinsermsuksakul, P.; Yang, P. D. *Angew. Chem. Int. Ed.* **2006**, *45*, 4597–4601.

[6] Wang, F.; Li, C. H.; Sun, L.-D.; Xu, C.-H., Wang, J. F.; Yu, J. C.; Yan, C.-H. *Angew. Chem. Int. Ed.* **2012**, *51*, 4872–4876.

[7] Wang, F.; Sun, L.-D.; Fang, W.; Chen, H. J.; Yeung, M. H.; Wang, J. F.; Yan, C.-H. *Small* **2010**, *6*, 2566–2575.

[8] Lee, H.; Habas, S. E.; Kweskin, S.; Butcher, D.; Somorjai, G. A.; Yang, P. D. *Angew. Chem. Int. Ed.* **2006**, *45*, 7824–7828.

[9] Chen, H. J.; Wang, F.; Li, K.; Woo, K. C.; Wang, J. F.; Li, Q.; Sun, L.-D.; Zhang, X. X.; Lin, H.-Q.; Yan, C.-H. *ACS Nano* **2012**, *6*, 7162–7171.

[10] Kim, Y.; Hong, J. W.; Lee, Y. W.; Kim, M.; Kim, D.; Yun, W. S.; Han, S. W. *Angew. Chem. Int. Ed.* **2010**, *49*, 10197–10201.

[11] Ni, W. H. Plasmonic spectroscopy of metallic nanostructures. Ph. D Thesis, Department of Physics, The Chinese University of Hong Kong. 2008

[12] Orendorff, C. J.; Murphy, C. J. *J. Phys. Chem. B* **2006**, *110*, 3990–3994.

[13] Oubre, C.; Nordlander, P. *J. Phys. Chem. B* **2004**, *108*, 17740–17744.

[14] Taflove, A. *Computational Electrodynamics: the Finite-Difference Time-domain Method.* Artech House Boston, 1995.

[15] Ni, W. H.; Kou, X. S.; Yang, Z.; Wang, J. F. *ACS Nano* **2008**, *2*, 677–686.

[16] Liu, Y.; Cheng, H.; Liao, L.; Zhou, H. L.; Bai, J. W.; Liu, G.; Liu, L. X.; Huang,

Y.; Duan, X. F. *Nat. Commun.* **2011**, *2*, 579.

[17] Hao, F.; Nordlander, P. *Chem. Phys. Lett.* **2007**, *446*, 115–118.

[18] Falk, A. L.; Koppens, F. H. L.; Yu, C. L.; Kang, K.; de Leon Snapp, N.; Akimov, A. V.; Jo, M.-H.; Lukin, M. D.; Park, H. *Nat. Phys.* **2009**, *5*, 475–479.

[19] Bennett, J. M.; Stanford, J. L.; Ashley, E. J. *J. Opt. Soc. Am.* **1970**, *60*, 224–232.

Chapter 3

Sulfidation of Ag Nanocubes

As I mentioned in Chapter 1, metal/semiconductor nanostructures have been widely utilized in light harvesting applications. Investigation of such nanoscale systems will undoubtedly benefit their applications. In this chapter, I will describe in detail my research work on Ag/Ag_2S nanocubes which were obtained by the sulfidation of Ag nanocubes. I chose nanoscale Ag/Ag_2S system for the following reasons. First, Ag nanocrystals are a typical type of plasmonic metals. Its localized surface plasmon is highly dependent on their surrounding dielectric environment. The refractive index sensitivities of Ag or other plasmonic nanocrystals have been investigated intensively [1–3]. Refractive index sensitivities exceeding 1000 nm/RIU have been reported for Ag nanoplates [4] and figures-of-merit exceeding 100 have also been demonstrated from the Fano resonances of lithographically patterned substrates [5]. In the visible region, Ag nanocrystals have been shown to be twice as sensitive to dielectric changes as Au nanocrystals when both metal nanocrystals with similar plasmon resonances and sizes are compared [6]. Even though Ag nanocrystals are superior for sensing, their applications are limited by their instability [7,8]. Second, Ag_2S is an intriguing narrow-bandgap (~1 eV) semiconductor with many outstanding properties, such as high light absorption, good chemical stability, and efficient photoluminescence. They have therefore been used as photocatalysts [9,10], in solar cells [11–13], and as bioimaging agents [15–19]. Ag_2S has also been used in a variety of devices, including IR detectors [20], photoconductors [21], and super-ionic conductors [22–24]. Third, the integration of Ag nanocrystals with Ag_2S, forming metal/semiconductor nanostructures, brings about improved application performances. For example, Ag/Ag_2S nanotubes have been found to exhibit excellent photocatalytic activity for the reduction of aqueous Cr(VI) and degradation of methyl orange [25]. A DNA detection limit of 1 pM has been realized using Ag/Ag_2S hybrid nanoprisms,

highlighting this hybrid to be a promising agent for biosensing applications [26]. Enhanced antibacterial properties under UV illumination have also been reported using Ag/Ag$_2$S heterodimers [27]. Moreover, Ag/Ag$_2$S nanostructures prepared through a variety of synthetic methods has been utilized to improve the stability of Ag nanocrystals. Ag$_2$S-incorporated Ag nanocubes and nanoprisms have been demonstrated to enhance both the thermal and structural stability of Ag nanocrystals [28]. The formation of Ag$_2$S shell on Ag nanocrystals changes the surrounding dielectric environment of the metal core, which therefore also serves as an effective way for tuning the plasmon resonance to be continuously across the entire visible range [29].

Sulfidation of Ag nanocrystals is an attractive synthetic way to the preparation of (Ag core)/(Ag$_2$S shell) nanostructures with different morphologies. Direct sulfidation can occur without introducing significant changes to the original morphology of Ag nanocrystals, as shown in the cases of Ag nanoprisms and nanocubes [28]. Through this synthetic method, the structural diversities of Ag/Ag$_2$S nanostructures have been enriched. While being an intriguing synthetic route, the mechanism of direct Ag sulfidation has rarely been studied, except that the reaction is initiated from the sharp tips of Ag nanocrystals in prisms and cubes [28]. It is also reported in this work [28] that sulfidation progresses towards the center of Ag nanocrystals, which is accompanied with a general red shift of the plasmon resonance peak. However, there is a lack of correlation between the exact structural changes occurring over the course of sulfidation with the changes in the plasmon resonances of Ag nanocrystals. Achieving an understanding of the sulfidation process is important, as this will enable fine tuning of the structural composition as well as the plasmonic properties of Ag/Ag$_2$S hybrid nanostructures.

In this work, I therefore make use of the high dependence of localized surface plasmon resonance on the morphology and surrounding dielectric environment of a metal nanocrystal to investigate the sulfidation process. Ag nanocubes were chosen as

starting nanocrystals to carry out the sulfidation reaction, because they exhibit multiple plasmon resonance modes, providing a wealth of information that can be correlated to the structural changes during sulfidation. The plasmonic properties, including the plasmon peaks and the corresponding nature of each plasmon resonance, of Ag nanocubes with sharp vertices are investigated both experimentally and by simulations using the finite-difference time-domain (FDTD) method. The related work will be presented in *Section 3.1*. In *Section 3.2*, I will discuss the spectral, plasmonic, and structural variations during the sulfidation process observed in my experiments and simulations. From the experimental and simulated results, the mechanism of sulfidation is found to occur *via* different pathways in the ensemble measurements as well as at the single-particle level (*Section 3.3*). At the end of this chapter, I will give a summary in *Section 3.4*. All of the contents in this chapter have been reported in *ACS Nano* in 2013 [30].

3.1 Plasmonic Properties of Ag Nanocubes

Ag nanocubes were prepared using the reported polyol reduction method, where the metal salt is reduced by pentanediol at 190 °C in the presence of poly(vinylpyrrolidone) (PVP) [31]. The detailed preparation process in my experiments is described in Chapter 2. After centrifugation to remove pentanediol and excess PVP, the Ag nanocubes are characterized using electron microscopes. Scanning electron microscopy (SEM) and transmission electron microscopy (TEM) imaging confirms that the Ag nanocubes exhibit well-defined facets (Figure 3.1a and b) with a high number yield up to 98%. In addition, the Ag nanocubes are highly monodisperse and uniform in shape, with the average edge length measured to be 93 ± 3 nm from the TEM images. It is also noted that the synthesized Ag nanocubes have sharp vertices.
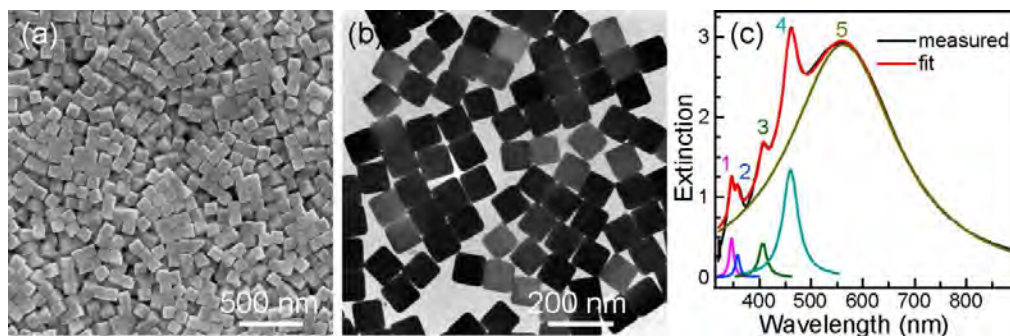
Figure 3.1 Prepared Ag nanocubes. (a,b) SEM and TEM images of the pre-grown Ag nanocubes, respectively. (c) Measured extinction spectrum of the Ag nanocubes. The spectrum is fitted with five Lorentzian peaks, which are individually plotted in different colors. The value of R^2 for the multiple peak fitting is equal to 0.9992.

Figure 3.1c depicts the extinction spectrum of the ensemble Ag nanocubes that were measured by dispersing the sample in water. Clearly, five plasmon resonance peaks are observed. Their peak wavelengths are determined from curve fitting to be 346 nm, 358 nm, 407 nm, 460 nm, and 562 nm. I labeled these peaks as peaks 1 to 5, respectively. The number of observable peaks on the ensemble spectrum and their spectral positions are closely dependent on the nanocube morphology, in particular, the sharpness of the corners and vertices and the nanocube size [32]. Although five plasmon resonance peaks have also been observed previously for ensemble Ag nanocube samples [31], the nature of the corresponding plasmon resonance modes has remained unidentified. FDTD simulations were therefore carried out using FDTD Solution 7.5 developed by Lumerical Solutions, Inc. to unravel the nature of the five plasmon modes. During simulations, the Ag nanocrystal was set as a cube with sharp edges and vertices and with an edge length of 93 nm according to the experimentally measured average size. The excitation direction was along one edge of the nanocube. The refractive index of the surrounding medium was 1.33, which is the index of water used to disperse the Ag nanocube sample in the experiment. Figure 3.2a shows the simulated extinction spectrum. Overall, the calculated spectrum is in good agreement with the measured extinction spectrum. On the simulated spectrum, six peaks are seen. An extra peak is detected in comparison to the experimental result. Their peak

wavelengths are found from curve fitting to be 343 nm, 366 nm, 402 nm, 430 nm, 515 nm, and 613 nm, respectively. During the FDTD simulation process, the dielectric function of silver was generated automatically by the software through fitting the input experimental data points. I believed that the peak at 402 nm is brought about by the slight deviation in the spectral region from 370 nm to 420 nm between the fitted dielectric function for silver and the experimental data. It is therefore not considered in this study.
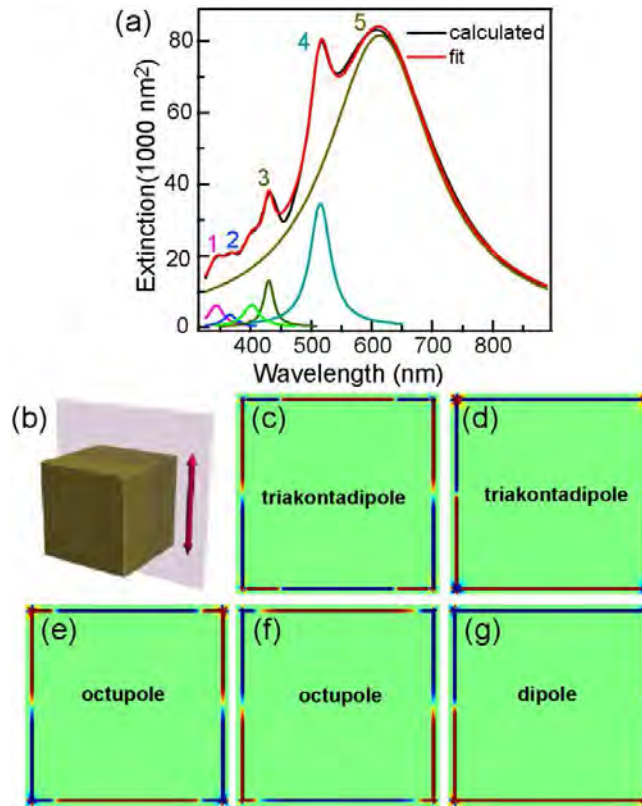
Figure 3.2 Nature of the plasmon modes of the Ag nanocube. (a) Calculated extinction spectrum of a single Ag nanocube. The spectrum is fitted with six Lorentzian peaks, which are individually plotted in different colors. The value of R^2 for the multiple peak fitting is equal to 0.9988. (b) Schematic showing the cross section through the center of a Ag nanocube. The double-arrowed line refers to the excitation polarization direction. (c–g) Charge distribution contours (red: positive; blue: negative) on the cross section as shown in (b) for the five plasmon resonance peaks labeled on the extinction spectra as 1 to 5, respectively. The nature of each plasmon resonance mode

is indicated on each charge distribution contour.

The five peaks observed on the measured spectrum of the Ag nanocube sample can be assigned on the basis of their peak wavelengths and intensities to the five plasmon resonance modes. It should be noted that there is a wavelength difference of ~50 nm for the smallest-energy peak between the FDTD simulations and measurements. Such deviation has been common in the numerical simulations of the extinction spectra of Ag nanocrystals with sharp edges and vertices [31,33]. To identify the nature of the plasmon resonance modes, the charge distribution contours of the five peaks were simulated (Figure 3.2b–g). The corresponding charge distribution contours of the five plasmon modes are shown in Figures 3.2c–g for peaks 1 to 5, respectively. Peaks 1 to 5 can be ascribed to triakontadipolar, triakontadipolar, octupolar, octupolar, and dipolar plasmon modes, respectively. The charges of peaks 1 and 4 are mainly distributed on the surfaces of the Ag nanocube (Figure 3.2c and f), while those of peaks 2 and 3 are distributed on both the surfaces and edges (Figure 3.2d and e). The charge distribution indicates the importance of the sharp edges in the appearance of peaks 2 and 3. Furthermore, slight truncation of edges leads to the disappearance of peaks 2 and 3, which is confirmed by the sulfidation experiments, as described below. Therefore, understanding the underlying nature of each plasmon resonance mode of metal nanocrystals can assist in correlating the spectral evolution with the structural variation of metal nanocrystals that are subjected to chemical reactions.

3.2 Spectral, Plasmonic, and Structural Variations during the Sulfidation of Ag Nanocubes

The study in this part was carried out both in experiments and simulations. In the experiment, I investigated the spectral, plasmonic, and structural evolutions at both the ensemble and single-particle levels. In general, sulfidation of the Ag nanocubes was realized by employing an aqueous Na_2S solution as the sulfur source which reacted with the washed Ag nanocubes to form Ag/Ag_2S nanostructures at room

temperature.

3.2.1 Ensemble Ag Nanocube Solution

For ensemble sulfidation, the as-grown Ag nanocube solution (0.3 mL) was first washed by the mixture of ethanol and water for three times. The washed Ag nanocube sample was redispersed into ethanol (0.1 mL), followed by adding an aqueous poly(vinylpyrrolidone) (PVP) solution (2.5 mL, 0.002 g mL^{-1}). A Na$_2$S solution (0.2 mL) with its concentration varied was dropped into the Ag nanocube solution. The final concentration of Na$_2$S in the reaction solution was controlled at 1 mM, 0.6 mM, and 0.2 mM, respectively. The concentration of the Ag nanocubes was estimated to be approximately 0.15 nM. The sulfidation reaction was kept under stirring and monitored by recording the extinction spectra as a function of the reaction time. The stop-clock was started as soon as the addition of Na$_2$S was complete. The measurements were stopped until both the peak positions and intensities showed no changes. Sulfidation of the Ag nanocubes can be described by the following equation [26]:

$$4Ag + O_2 + 2H_2O + 2Na_2S = 2Ag_2S + 4NaOH$$

The standard change of reaction in Gibbs free energy, $\Delta_rG°$, for this reaction is –491.8 kJ. Therefore, sulfidation of the Ag nanocubes will proceed spontaneously as soon as an aqueous Na$_2$S solution is added to the Ag nanocube solution.
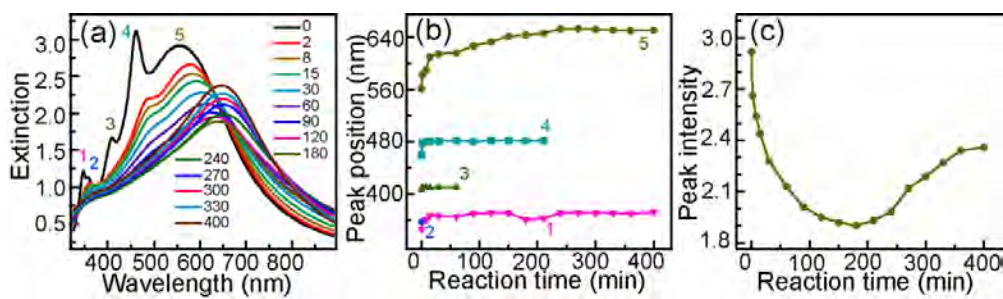
Figure 3.3 Time-dependent spectral evolutions as functions of the reaction time over

the sulfidation of the ensemble Ag nanocubes in the presence of 1 mM Na_2S. (a) Representative extinction spectra of the reaction mixture that were tracked as a function of the reaction time. The unit of the annotation is minute. The optical path length is 0.5 cm. (b) Evolutions of the peak positions as a function of the reaction time. (c) Variation of the extinction intensity of peak 5 as a function of the reaction time.

Over the course of sulfidation, spectral changes in the extinction spectrum of the reaction solution were tracked as the function of the reaction time. Figure 3.3a shows the extinction spectra acquired for the sulfidation reaction with 1 mM Na_2S. Distinct changes are observable on the extinction spectra. To reveal more clearly the spectral changes during the sulfidation process, the positions of the five peaks and the extinction intensity of peak 5 are plotted in Figure 3.3b and c as functions of the reaction time. The spectral variations can be generally divided roughly into two stages. The first stage is from the start to ~10 min. At this stage, the positions of the five peaks change dramatically. Peak 2 disappears within ~2 min. Peaks 1, 4, and 5 show large red shifts and reach plateaus by the end of the first stage. The second stage covers from ~10 min to ~400 min. The spectral positions of peaks 1, 3, 4, and 5 only slightly change. Peak 3 cannot be observed after ~60 min, and peak 4 vanishes after sulfidation for ~210 min. Herein, only the extinction intensity of peak 5, arising from a dipolar plasmon resonance mode, is plotted as the function of the reaction time (Figure 3.3c). This is because the other peaks either vanish or are very weak during the sulfidation reaction. Clearly, peak 5 exhibits a rapid decrease in extinction intensity within ~30 min after the sulfidation reaction is originated. The extinction intensity reaches a minimum around 180 min, with the intensity at the minimum being 65% of that at the start. After the minimum, the extinction intensity of peak 5 starts to increase slowly. After the sulfidation is started for 400 min, no further change in the spectral position of the five plasmon peaks and intensity of peak 5 is observable. The extinction spectral monitoring was therefore stopped. At this reaction time, the extinction intensity becomes 80% of that at the start, and the peak wavelength is 651 nm, being red-shifted by 90 nm in comparison to that at the start.
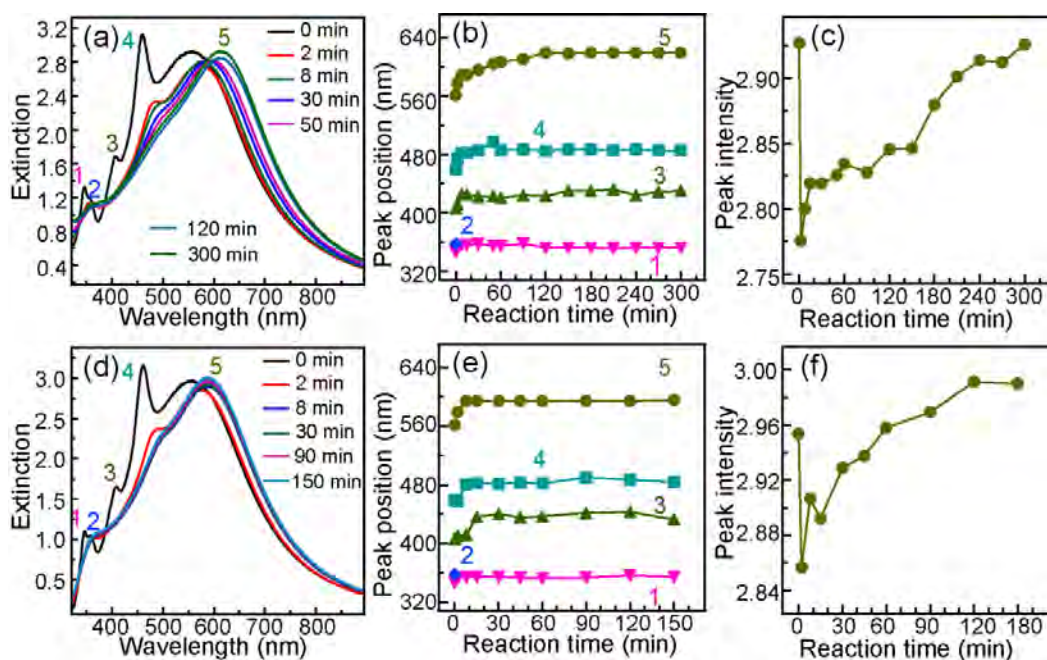
Figure 3.4 Time-dependent spectral evolutions as functions of the reaction time over the sulfidation of the ensemble Ag nanocubes in the presence of 0.6 mM (top row) and 0.2 mM Na_2S (bottom row). (a,d) Representative time-dependent extinction spectra of the reaction mixture. The unit of the annotation is minute. The optical path length is 0.5 cm. (b,e) Evolutions of the peak positions as functions of the reaction time. (c,f) Variations of the extinction intensity of peak 5 as a function of the reaction time.

Similar spectral evolutions were also observed when sulfidation was carried out at lower Na_2S concentrations of 0.6 mM and 0.2 mM (Figure 3.4a–f). Peak 2 vanishes almost instantly upon sulfidation. The other four peaks show rapid red shifts within first ~10 min after the reaction. After that, their peak positions stay almost unchanged as the sulfidation process proceeds. With the addition of Na_2S at low concentrations, smaller net red shifts of peak 5 from the start to the end of the monitoring process are observed. The red shifts of peak 5 for sulfidation in the presence of 0.6 mM and 0.2 mM Na_2S are 58 nm and 34 nm, respectively. At the lower concentrations of Na_2S, the octupolar plasmon modes, peaks 3 and 4, remain longer in the course of sulfidation. In addition, the extinction intensity of peak 5 drops to a minimum within

2 min of the reaction for both lower concentrations of Na_2S. The intensity reductions relative to those at the start are small, 5% and 3% for 0.6 mM and 0.2 mM Na_2S, respectively. This behavior is different from that observed for 1 mM Na_2S. Because the plasmonic spectral properties of metal nanocrystals are determined by the nanocrystal size, shape, and surrounding environment, the spectral variations observed during the sulfidation with different concentrations of Na_2S demonstrate that the sulfidation behavior at the early stage is similar under different concentrations of Na_2S, while the sulfidation behavior varies with the concentration of Na_2S at the late stage. Besides, the sulfidation reactions with higher concentration of Na_2S at 1.5 mM or above were also performed. The high ionic strength caused the quick aggregation of the Ag nanocubes, which prevented the investigation of the time-dependent sulfidation process.
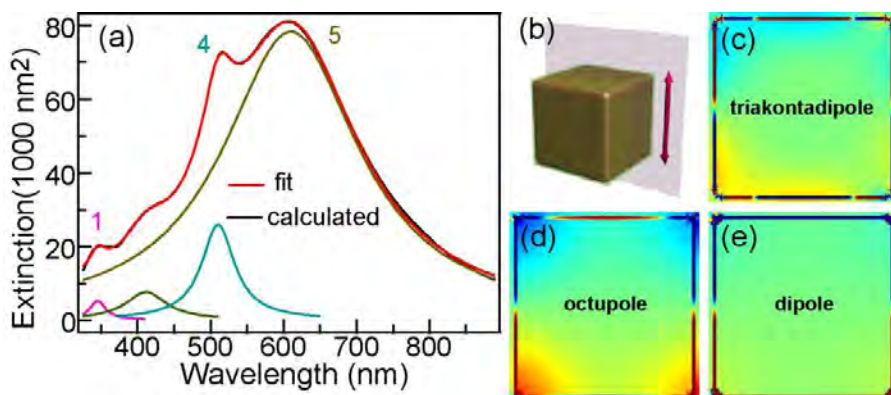
Figure 3.5 Plasmonic properties of the slightly truncated Ag nanocube with a 3-nm radius of curvature for all of the edges by Ag_2S. (a) Simulated extinction spectrum. The spectrum is fitted with Lorentzian peaks, which are individually plotted and labeled. The value of R^2 for the multiple peak fitting is equal to 0.9995. (b) Schematic describing the truncated Ag nanocube and the cross section through the center of the cube. The double arrow refers to the excitation polarization direction. (c–e) Charge distribution contours (red: positive; blue: negative) on the cross section as shown in (b) for the three plasmon resonance peaks labeled on the extinction spectrum as 1, 4, and 5, respectively. The nature of each plasmon resonance mode is indicated on each charge distribution contour.

Sulfidation has been reported to start at the sharp tips of Ag nanoprisms and nanocubes [31]. This also occurs with the ensemble Ag nanocube sample in my experiments. At the sharp edges and vertices, the Ag atoms are less capped by the stabilizing molecules and have fewer neighboring atoms [34,35]. They are therefore prone to be attacked by the sulfur-containing species in the solution. From the perspective of surface chemistry, the edges and vertices are the initiation sites on the Ag nanocubes for sulfidation. Since the electric charges associated with peak 2, a triakontadipolar plasmon mode, are mainly located at the surfaces and edges of the Ag nanocube, the nearly instant disappearance of peak 2 upon sulfidation can be ascribed to the preferential truncation of the vertices and edges of the Ag nanocube. To ascertain this ascription, FDTD simulations were performed on a 93-nm Ag nanocube that was truncated at all of the edges. The truncation radius was 3 nm and the truncated regions were replaced with Ag_2S. Figure 3.5a gives the simulated extinction spectrum, which is in good agreement with the experimental one that were acquired at 2 min after the reaction was initiated (Figure 3.3a). Four peaks at 345 nm, 410 nm, 512 nm, and 610 nm are observable in the simulated extinction spectrum. The peak at 410 nm is ignored, because it might be jointly caused by the deviation brought about by FDTD simulations and the octupolar plasmon mode, as mentioned above. According to their charge distributions, the other three peaks can be taken as corresponding to peaks 1, 4, and 5 of the original perfect Ag nanocube, which are triakontadipolar, octupolar, and dipolar plasmon modes, respectively (Figure 3.3b–e), Peak 2, a trikontadipolar plasmon mode, is not observable. The FDTD simulations therefore confirm that the disappearance of peak 2 right after the start of the reaction is caused by the edge truncation of the Ag nanocube through sulfidation, and in turn that sulfidation starts at the vertices and edges of the Ag nanocube. These results suggest preliminarily that the sulfidation process of the Ag nanocubes can be tracked by monitoring the spectral evolutions of the plasmon resonance modes.
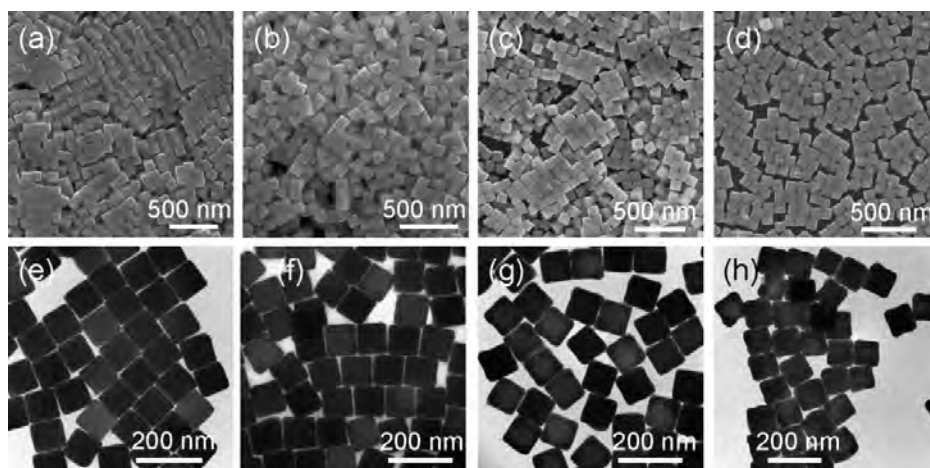
Figure 3.6 Electron microscopy characterizations of the intermediates. (a–d) SEM and (e–h) TEM images of the intermediate products collected at 2 min, 30 min, 150 min, and 400 min, respectively.
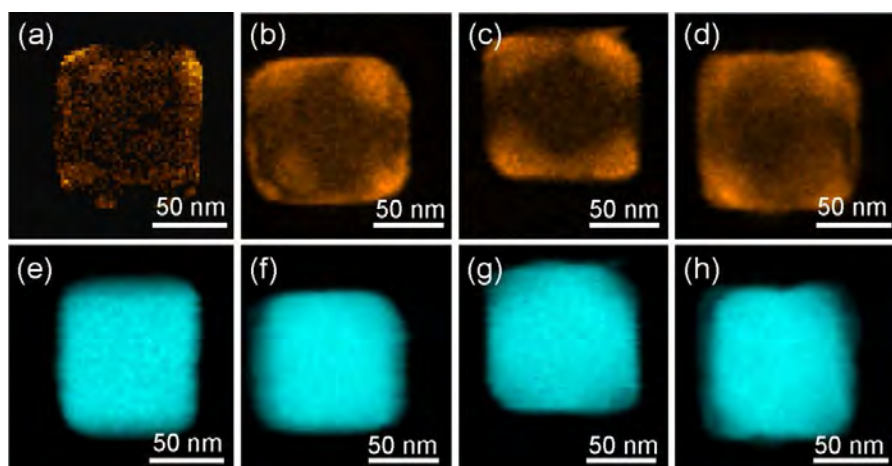
Figure 3.7 Elemental mapping of the sulfidation products collected after different periods of the reaction time. The top row shows the maps of S, and the bottom row shows the maps of Ag. (a,e) 2 min. (b,f) 30 min. (c,g) 150 min. (d,h) 400 min.

Structural characterizations were preformed on the sulfidation products that were collected at 2 min, 30 min, 150 min, and 400 min of the reaction with 1 mM Na_2S. Figure 3.6a–d shows the SEM images of the nanostructures. Clear, the nanostructures remain cubic with smooth facets over the course of sulfidation. At 400 min, small bumps appear on the surfaces of the nanostructures. They are caused by electron-beam irradiation during SEM imaging. A considerable amount of Ag in each

nanostructure is converted into Ag_2S at this reaction time. As reported previously, electron-beam irradiation can decompose Ag_2S to generate Ag nanoparticles on the surface of Ag_2S nanostructures [36]. The TEM images (Figure 3.6e–h) taken on the same products, as seen under SEM imaging, confirm the cubic shape and smooth facets. From the TEM images, the average edge lengths of the four intermediate products are found to be slightly enlarged to 95 ± 2 nm, 96 ± 2 nm, 99 ± 4 nm, and 108 ± 5 nm. There is also contrast difference between the edges and center of the cubic products from the TEM images. The contrast difference becomes clearer as the sulfidation reaction proceeds, suggesting that Ag is gradually converted into sulfide. Elemental mapping was therefore carried out to reveal the composition evolution during sulfidation (Figure 3.7a–h). Sulfur is clearly detected at the edges when the reaction was initiated for 2 min, confirming again that sulfidation is initiated at the edges and vertices of the Ag nanocubes. As thesulfidation reaction proceeds, the region representing S on the elemental map is enlarged and expanded towards the center. However, no S but Ag is detected from the central region of the cubic nanostructures even at 400 min after reaction. The absence of the S signal in the central region suggests that the Ag nanocubes are not completely converted into sulfides. Incomplete sulfidation is also corroborated by energy-dispersive X-ray (EDX) analysis and X-ray diffraction (XRD) measurements. EDX measurements (Figure 3.8a–d) indicate the average molar percentages of S are increased to be (5.3 ± 0.7)%, (8.2 ± 1.6)%, (513.8 ± 1.0)%, and (18.7 ± 1.0)% for the four sulfidation products, respectively. The XRD patterns (Figure 3.9a–e) of the sulfidation products can be indexed according to the face-centered-cubic structure of Ag (JCPDS 89–3722) and the monoclinic structure of Ag_2S (JCPDS 14–72), indicating the conversion of Ag into Ag_2S during the sulfidation process. The time-dependent XRD patterns also exhibit an increase in the amount of Ag_2S with the reaction time. The S molar percentage in Ag_2S is 33%, much larger than the value of 18.7% at 400 min, confirming again incomplete sulfidation. Incomplete sulfidation can be ascribed to the following two reasons. First, the amount of Na_2S at 1 mM is slightly deficient by

comparing the estimated amounts of Ag and Na$_2$S in our experiments according to the stoichiometric reaction given above. Second, it is difficult for S^{2-} to diffuse into the center of the nanocube because of the relatively large size. In addition, the edge length increase can be explained by the smaller density of Ag$_2$S (7.2 g cm^{-3}) compared to that of Ag (10.505 g cm^{-3}). Complete sulfidation would give a final edge length of 110 nm for the Ag$_2$S nanocube. This size is slightly larger than the average one measured at 400 min after reaction, which might be due to the measurement deviations and/or that the density of Ag$_2$S obtained in our experiments is smaller than the density in theory.
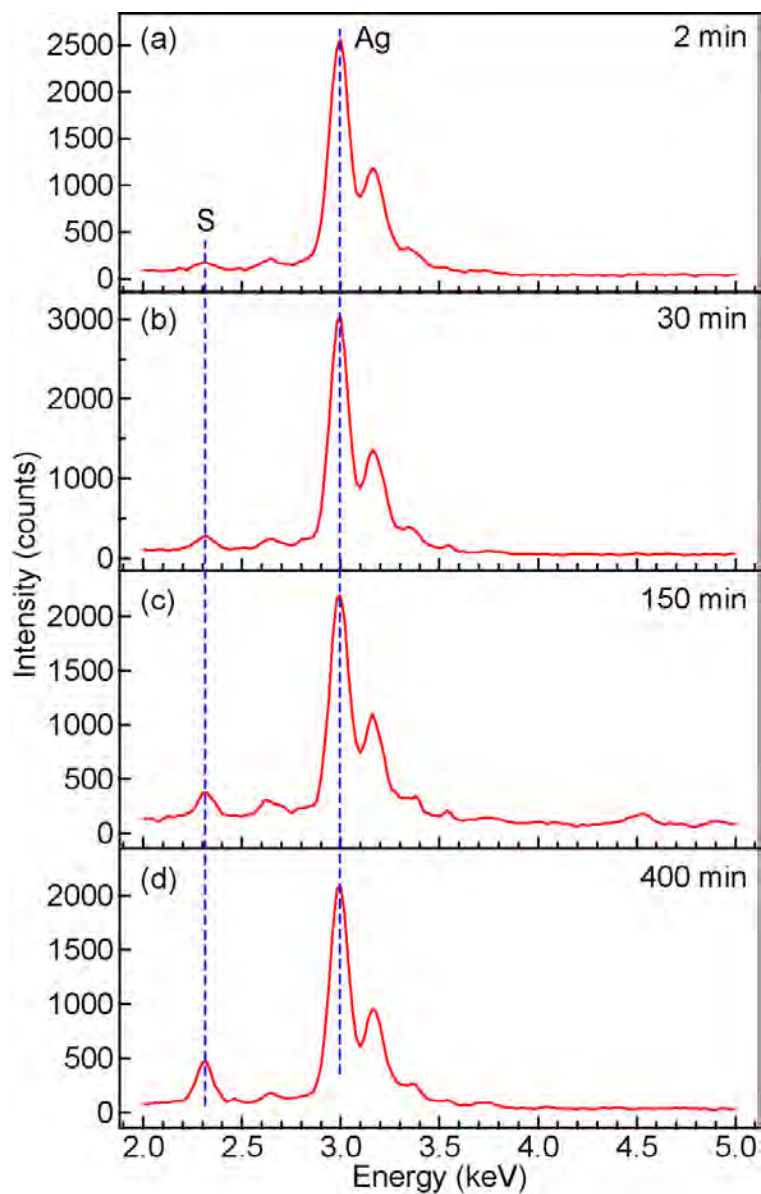
Figure 3.8 Representative EDX spectra that were acquired from the intermediate products during the sulfidation reaction that were collected at varying periods of the reaction time. (a) 2 min. (b) 30 min. (c) 150 min. (d) 400 min. For each sample, more than eight areas were measured.
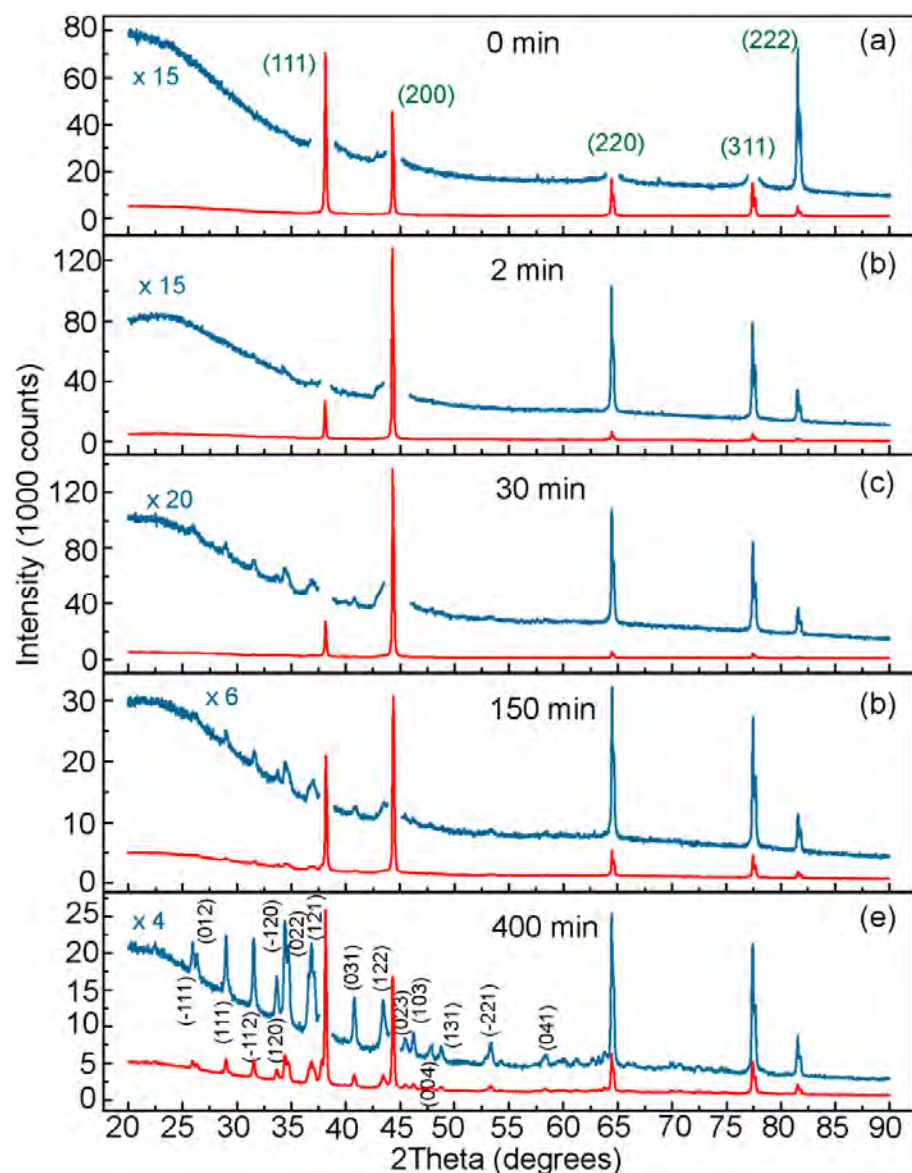
Figure 3.9 XRD patterns of the intermediate products during sulfidation collected at varying periods of the reaction time. (a) 0 min. (b) 2 min. (c) 30 min. (d) 150 min. (e) 400 min. For better showing the weak peaks, the patterns are magnified. The diffraction peaks are indexed according to the face-centered-cubic structure of Ag (green numbers) and the monoclinic structure of Ag_2S (black numbers)

Taken together, the structural characterizations show that the sulfidation of the Ag nanocubes starts from the highly reactive edges and vertices, and proceeds to form a shell of Ag_2S around each Ag nanocube. The conversion of the edges and vertices into Ag_2S causes the vanishing of peak 2, a triakontadipolar plasmon mode.

Continuous sulfidation gradually reduces the size of the Ag core and simultaneously increases the thickness of the Ag_2S shell, which is reflected on the extinction spectra as the continuous red shifts and intensity variations of peak 5, a dipolar plasmon mode. The spectral changes of peak 5 are mainly caused by the formation of Ag_2S shell, which increases in thickness and has a larger refractive index than water. These results indicate that the structural change and the plasmonic evolution are closely correlated with each other. The latter can be employed to help in tracking and elucidating the sulfidation progress.

3.2.2 Single Ag Nanocubes

To eliminate the averaging effect associated with the ensemble measurements as well as highlight the plasmonic sensitivity of the sulfidation products to the structural and environmental changes, the sulfidation reactions at the single-particle level were carried out. The measurements employed a microfluidic chip made of poly(dimethylsiloxane) (PDMS) together with an optical microscope that was capable of single-particle dark-field scattering imaging/spectroscopy [37], which is shown in Figure 3.10. In detail, the microfluidic chip was fabricated to ensure the continuous injection of Na_2S solution. Ag nanocubes were first deposited on a cleaned cover glass by immersing the slides in the washed nanocube dispersion for about 30 s and then blowing them dry with nitrogen. The microfluidic chip was fabricated using standard lithography techniques with PDMS. Typically, the mixture of the prepolymer component A (6.0 g, GE, RTV615) and component B (0.6 g), the crosslinker, was cast on a mould and subjected to polymerization at 65 °C for 1 h. After the PDMS surface was treated with oxygen plasma (18 W, Harrick Scientific, PDC-32G) for about 50 s, it was bound with the pre-made nanocube-deposited glass slide. Deionized water was first pumped into the microchannel through a plastic tube that was inserted into a hole using a syringe pump. An aqueous Na_2S solution at the concentration of 1 mM was continuously pumped into the microchannel using a syringe pump with a flow rate of

the solution at ~0.1 mL min⁻¹. Single-particle darkfield scattering spectra were collected as a function of time over the course of sulfidation.
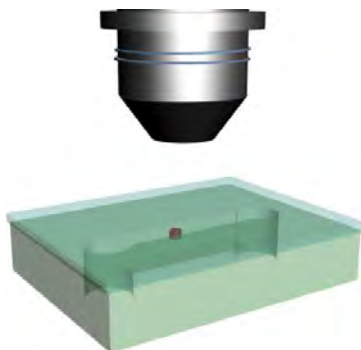
Figure 3.10 Schematic illustrating the setup used to measure the single-particle scattering spectra during sulfidation. The aqueous Na_2S solution was pumped into the microchannel with a syringe pump.

Figure 3.11a shows the time-dependent scattering spectra recorded on a representative Ag nanocube. Only one broad peak is observed on the scattering spectrum before sulfidation (black curve). This peak can be attributed to the dipolar plasmon mode (peak 5) of the nanocube, as discussed above. The absence of the other plasmon peaks on the single-particle scattering spectra is caused by the limit of our optical system in the spectral detection range and the nonradiative nature of the higher-order plasmon modes, which are difficult to be detected through far-field scattering detection. The dipolar plasmon peak is located at 608 nm in water before Na_2S is introduced, while the corresponding one for the ensemble sample is at 562 nm. The difference in the peak wavelength is due to the nanocube size distribution and the higher refractive index of the glass substrate. During sulfidation, the scattering peak red-shifts and gets weaker. The peak position and intensity are extracted and plotted in Figure 3.11b and c. Similar to the evolution of peak 5 during the ensemble sulfidation process, the variation of the dipolar plasmon peak during the single-particle sulfidation reaction also exhibits two stages. The peak red-shifts rapidly from 608 nm to ~850 nm at the first stage from 0 min to ~80 min. It reaches a plateau and then red-shifts slightly to ~870 nm at the second stage from ~80 min to ~180 min. The overall red shift of ~260 nm observed in the single-particle sulfidation

process is much larger than that (~90 nm) in the ensemble sulfidation process. The peak scattering intensity undergoes a gradual reduction throughout the sulfidation process, with an overall decrease of ~85%. This is different from the intensity variation observed in the ensemble sulfidation experiment, where the extinction intensity of peak 5 first decreases, reaches a minimum, and then increases, with the overall intensity reduction being 20%. Moreover, a new broad peak is detected in the spectral region below 500 nm at the later stage of sulfidation, while it is not observed during the ensemble sulfidation process. The wavelength of this new peak cannot be determined exactly because of the limit in the spectral detection range.
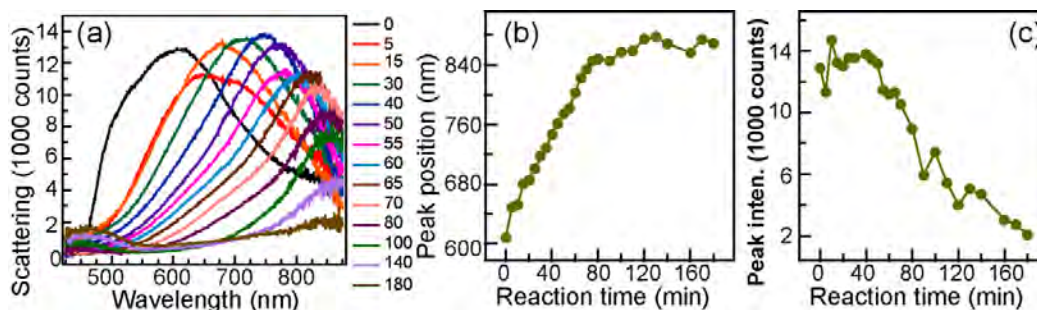
Figure 3.11 Time-dependent spectral variations as functions of the reaction time over the single-particle sulfidation process of the Ag nanocubes in the presence of 1 mM aqueous Na_2S solution. (a) Representative scattering spectra recorded during sulfidation. The unit of the annotation is minute. (b) Peak position evolutions of peak 5 as a function of the reaction time. (c) Variation of the peak intensity (peak 5) as a function of the reaction time.

3.2.3 Simulation Results

FDTD simulations were performed to unravel the reasons for the different spectral evolutions observed during the ensemble and single-particle sulfidation experiments. Two major structural variations are observed experimentally during the sulfidation process from the ensemble sulfidation products. One is that the chemical composition is changed from Ag to Ag_2S, leading to the concomitant decrease in the Ag core size,

while the overall shape of the hybrid particle remains to be cubic. The other is the overall increase in the edge length of the cubic hybrid particle. The reduction in the Ag core during sulfidation is simulated by first rounding the sharp edges and vertices, with the rounding radius increasing at 6 nm per step (Figure 3.12a). After eight steps of rounding, a Ag nanosphere with its diameter equal to the edge length of the starting Ag nanocube is obtained. After that, the Ag nanosphere is reduced in diameter at 12 nm per step until the Ag core is completely consumed. Throughout the sulfidation process, the volume that is released from rounding and size reduction is filled with Ag_2S, and the overall shape is maintained to be cubic. For comparison, simulations were also performed by retaining the cubic shape of the Ag core throughout the sulfidation process, with the edge length being shrunk at 6 nm per step until the Ag core is consumed (Figure 3.13a). In both cases, the edge length of the entire cubic particle is fixed at 93 nm, with no change over the course of sulfidation. Fixing the edge length allows for identifying the role played individually by the complex simultaneous structural changes on the plasmon resonances of the sulfidation products. The dielectric functions in the simulations were formulated using Johnson and Christy data for Ag and the data from a previous report for Ag_2S [38].
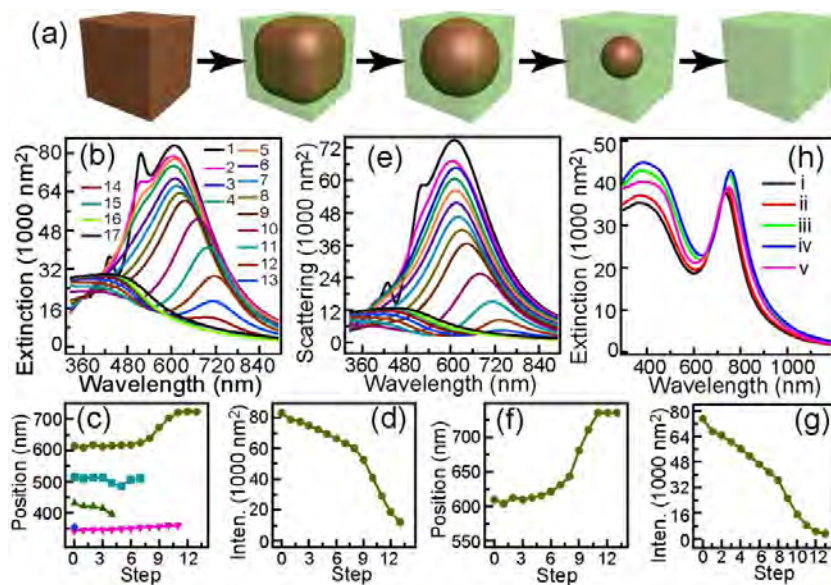
Figure 3.12 Simulated spectral variations during the sulfidation of a Ag nanocube. (a) Schematic describing the sulfidation process of the Ag nanocube. The sharp edges

and vertices of the Ag nanocube are truncated. The Ag core is transformed into a nanosphere, with its diameter gradually reduced. The Ag core is finally completely reacted. Ag is converted into Ag_2S through the sulfidation reaction. The entire nanostructure keeps its cubic shape with a edge length fixed at 93 nm. (b) FDTD calculated extinction spectra at different sulfidation steps. (c,d) Peak wavelength evolutions of the five plasmon modes and the peak intensity variations *versus* the sulfidation step number extracted from the extinction spectra in (b). (e) Corresponding scattering spectra. (f,g) Position and intensity variations of peak 5 obtained from (e). (h) Calculated extinction spectra obtained by fixing the size of the Ag core while increasing the thickness of the Ag_2S shell. The diameter of the spherical Ag core is fixed at 60 nm. The edge lengths of the entire cubic particle are (i) 100 nm, (ii) 102 nm, (iii) 106 nm, (iv) 108 nm, and (v) 110 nm, respectively.

The simulated extinction spectra and spectral evolutions of the five plasmon resonance peaks during the transformation of the Ag nanocube into a nanosphere and subsequent consumption of the Ag core are presented in Figure 3.12b and c, respectively. Peaks 2 and 3 vanish rapidly. Peaks 1 and 4 stay longer and red-shift slightly during sulfidation. In particular, peak 4 vanishes when the Ag core becomes a nanosphere. Peak 5 shows a slight red shift of ~5 nm before the Ag core is rounded to become a nanosphere. It thereafter exhibits a more distinct red shift of ~105 nm from ~620 nm to ~725 nm as the Ag core nanosphere is gradually consumed. The extinction intensity of peak 5 first shows a slower decrease and then a rapid decrease, with the transition occurring at the same step as that for the peak position evolution (Figure 3.12d). The intensity is reduced by 85%. Meanwhile, a new broad peak shows up around 420 nm and gets stronger after the Ag core becomes a nanosphere. The corresponding scattering spectra for the same sulfidation process were also obtained (Figure 3.12e). Figure 3.12f and g exhibit the evolutions of the position and scattering intensity of peak 5 plotted according to the calculated scattering spectra, respectively. From the scattering spectra, peak 5 shows a red shifts of 125 nm from ~610 nm to ~735 nm and a decrease in intensity of 95% throughout the whole sulfidation process.

Generally, the variation trends of the dipolar plasmon peak (peak 5) position and intensity obtained from the simulated scattering spectra are in agreement with those observed from the single-particle scattering measurements. Moreover, at the beginning stage of sulfidation, during which the starting Ag nanocube is gradually truncated into a nanosphere, the general evolution trends of the plasmon peak positions and the extinction intensity of peak 5 agrees with those observed from the ensemble sulfidation experiments. There are discrepancies in the spectral evolutions between the experiments and simulations. The discrepancies are believed to arise from the following factors. First, the experimental spectra were taken as a function of the reaction time, while the simulated spectra were obtained as a function of the sulfidation step. It is difficult to correlate the reaction time with the simulation step, especially at the initial sulfidation stage, during which the truncation of the vertices and edges of the Ag nanocube occurs, because the plasmon modes are very sensitive to the truncation degree. Second, there are fluctuations in both the size of the Ag nanocube and the sulfidation process of each nanocube, which affects the comparison between the ensemble sulfidation measurements and the simulations as well as that between the single-particle scattering measurements and the simulations, because the simulations were performed on an averagely-sized Ag nanocube. Third, because Ag_2S has a smaller density than Ag, the conversion of Ag into Ag_2S must be accompanied by the volume expansion. Since it is difficult to account for these two processes simultaneously, the size of the entire hybrid cubic particles was fixed during our simulations.

On the other hand, two clear discrepancies are seen at the later sulfidation stage between the simulations and ensemble experiments. One is the extinction intensity change of peak 5. It increases in the ensemble sulfidation experiments (Figure 3.3a), but decreases in the simulations (Figure 3.12d). The other is the appearance of a broad peak around 420 nm in the simulations (Figure 3.12a), while this peak is absent in the ensemble experiments (Figure 3.3a). Both can be ascribed to the incomplete sulfidation of the Ag nanocubes in the ensemble experiments. The incomplete

sulfidation has been verified by the structural characterizations described above. To ascertain the reason for the increase in the extinction intensity of peak 5 at the later ensemble sulfidation stage, FDTD simulations were carried out on a hybrid nanocube composed of a 60-nm Ag sphere and a Ag_2S shell. The edge length of the nanocube was increased step-by-step from 100 nm to 110 nm, while the Ag core diameter was fixed. The simulated extinction spectra (Figure 3.12h) display a slight red shift and an increase in the peak intensity by 14%. Therefore, the sulfidation-caused enlargement of the hybrid nanocubes can account for the extinction intensity increase at the later ensemble sulfidation stage. The broad peak around 420 nm can be ascribed to the absorption and scattering of the Ag_2S shell, because it is also observable on the simulated scattering spectra (Figure 3.12e) and its extinction intensity is large than its scattering intensity. The simulated extinction and scattering spectra (Figure 3.12b and e) show that both the extinction and scattering intensities increase with the relative amount of Ag_2S in the hybrid nanocube. The occurrence of this peak is determined by its intensity relative to that of the dipolar plasmon peak of the Ag core, which in turn depends on the relative amounts between Ag and Ag_2S. From the discussion above and according to the observations that the scattering intensity of peak 5 continuously decreases and that a broad scattering peak appears around 420 nm at the later stage in the single-particle measurements, we can reason that the Ag nanocube is completely converted into Ag_2S under the single-particle measurement conditions. The complete sulfidation is understandable, because the Na_2S solution was continuously supplied into the microchannel during the single-particle measurements.
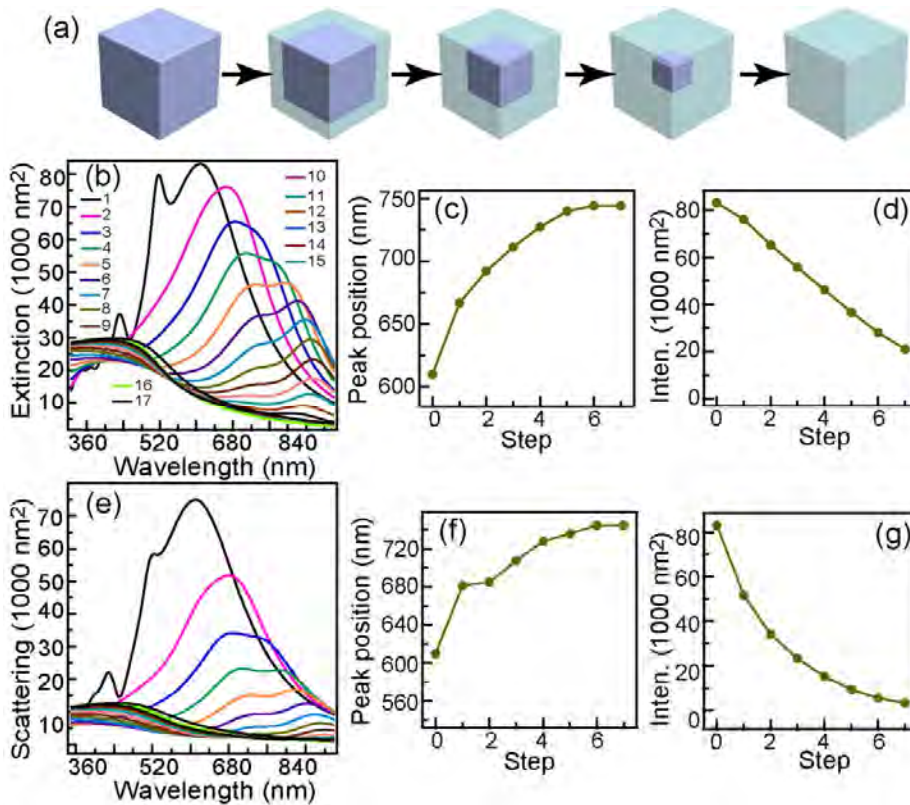
Figure 3.13 FDTD simulations of the sulfidation process, where the Ag nanocube is assumed to maintain the cubic shape. The edge length is reduced gradually. (a) Schematic illustrating the sulfidation process. The shape of the entire particle and the Ag core are assumed to remain its cubic shape. The edge length of the entire particle is assumed to be fixed at 93 nm. (b) Calculated extinction spectra. The annotations refer to the sulfidation steps. The edge length of the cubic Ag core is reduced by 6 nm for each step. (c) Evolution of the dipolar plasmon peak positions obtained from (b). (d) Variation of the dipolar plasmon peak intensities obtained from (b). (e) Corresponding simulated scattering spectra. (f) Variation of the dipolar plasmon peak positions obtained from (e). (g) Evolution of the dipolar plasmon peak intensities obtained from (e). Two peaks appear above 600 nm as sulfidation goes on. The peak positions and intensities plotted in (c), (d), (f), and (g) refer to those of the shorter-wavelength peak.

The retaining of a cubic shape for the Ag core over the course of sulfidation is unlikely, as revealed by the simulated extinction and scattering spectra and the

extracted position and intensity changes (Figure 3.13b–g). Although the general trends are qualitatively similar to those observed in the single-particle experiments, the spectral shape is very different from the experimental ones. Two distinct differences are noticed. First, the higher order plasmon modes, in particular, the octupolar one, cannot be discerned at the beginning sulfidation stage on the extinction spectra, which is in contrast to the ensemble sulfidation experiments. Second, both the extinction and scattering spectra display two peaks above 600 nm as sulfidation goes on. This double-peak feature is neither observed on the ensemble nor single-particle sulfidation experiments. Clearly, the simulation results obtained on the assumption that the cubic shape of the Ag core is retained are not in agreement with the ensemble or single-particle experiments. The Ag nanocubes must undergo shape transformation during the sulfidation process, with it being increasingly truncated over time.
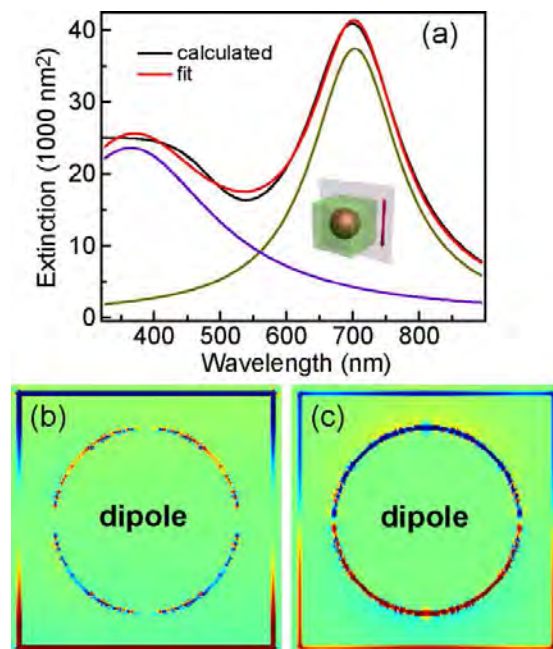
Figure 3.14 Simulated extinction spectrum and plasmon modes of the (Ag nanosphere core)/(Ag$_2$S shell) cubic hybrid nanostructure. The edge length of the entire edge length is set to be 93 nm, while the diameter of the spherical Ag core is 70 nm. (a) Extinction spectrum of the nanostructure obtained from FDTD simulation. The spectrum is fitted with two Lorentzian peaks. The coefficient of determination for the

fitting is $R^2 = 0.9930$. The inset is the schematic of the nanostructure and the cross section that passes through the center of the nanostructure for showing charge distributions. The double-arrowed line represents the excitation polarization direction. (b) Charge distribution (red: positive, blue: negative) of the 365-nm peak. (c) Charge distribution of the 703-nm peak.

Additionally, FDTD simulations were performed on the (Ag nanosphere core)/(Ag$_2$S shell) nanostructure with a cubic shape that is formed at the intermediate sulfidation stage to ascertain its plasmon modes. Two peaks are seen on the extinction spectrum (Figure 3.14a), which are fitted to be located at 365 nm and 703 nm, respectively. Figure 3.14b and c provide their corresponding charge distributions for the two plasmon resonance peaks. At the 365 nm peak, a small amount of charges is present on the spherical Ag core. The charge distribution shows a mixture of dipolar and higher-order oscillation characteristics. A large amount of charges is present on the outer surface of the Ag$_2$S shell, with the charge distribution indicating a dipolar plasmon mode. The much smaller amount of charges on the Ag core suggests that this peak is dominantly contributed by the charge oscillations in the Ag$_2$S shell. This observation is in agreement with the reasoning above that the broad peak around 420 nm is mainly contributed by the absorption and scattering of the Ag$_2$S shell. For comparison, the charge distributions on the Ag core and Ag$_2$S shell are both dipolar, with the charge intensities being comparable to each other for the 703 nm peak. This result implies that the Ag core maintains the dipolar oscillation in the sulfidation process, even though the dipolar plasmon resonance intensity becomes weaker.

3.3 Proposed Sulfidation Process

Based on the experimental sulfidation, structure characterization, and FDTD simulation results, the sulfidation processes of the Ag nanocubes under both the ensemble and single-particle conditions are proposed (Figure 3.15). In both conditions, sulfidation starts from the sharp edges and vertices, and progresses towards the center,

with a Ag_2S shell formed around the Ag core. The continuous truncation of the Ag nanocube leads to the transformation from a nanocube into a nanosphere. After that, the diameter of the Ag core gets smaller and smaller. At this stage, the sulfidation processes start to differ between the ensemble and single-particle experiments. Under the ensemble conditions, the sulfidation process stops at a certain point, forming (Ag core)/(Ag_2S shell) hybrid nanostructures, owing to the insufficient supply of Na_2S (Figure 3.15a). Under the single-particle conditions, the continuous supply of Na_2S leads to the complete sulfidation of the Ag nanocube, producing a Ag_2S nanoparticle (Figure 3.15b). Under both conditions, throughout the sulfidation processes, the Ag/Ag_2S hybrid nanoparticles maintain the cubic shape with an increase in size due to the smaller density of Ag_2S than that of Ag.
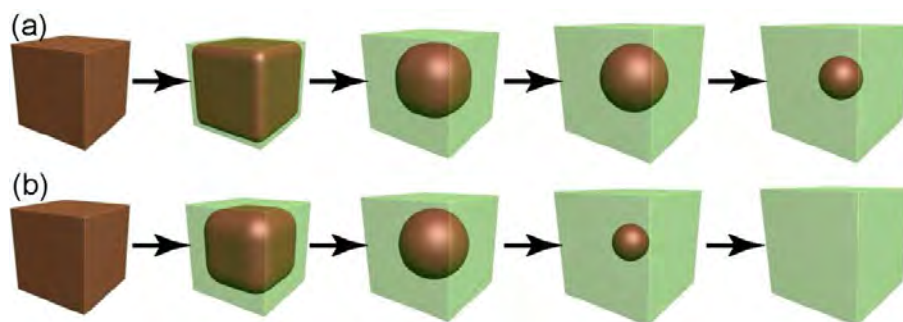
Figure 3.15 Schematics illustrating the sulfidation process under the ensemble (a) and single-particle (b) situations.

3.4 Summary

In this chapter, I studied the sulfidation process of Ag nanocubes by combining experimental ensemble and single-particle spectral measurements, structural characterizations of the intermediate sulfidation products, and FDTD simulations. This study replies on the high dependence of the strong and rich localized surface plasmon resonance modes of Ag nanocubes on the shape, size, and surrounding environment. The starting Ag nanocubes possess five plasmon modes, with their natures identified to be triakontadipolar, triakontadipolar, octupolar, octupolar, and dipolar oscillations in the order from high to low energies. The cubic shape is

maintained throughout sulfidation, with an increase in the overall edge length. The quick disappearance of the higher-order plasmon modes with charges mainly localized at the sharp vertices and edges of the nanocube evidences that sulfidation starts at the vertices and edges. The progressive red shifts and intensity evolutions of the other plasmon modes are correlated with the structural changes during the sulfidation process with the assistance of extensive FDTD simulations. The experiments and simulations together show that during sulfidation, the Ag nanocube is continuously truncated until it becomes a nanosphere, which is embedded within a Ag_2S shell. After that, the Ag core continuously decreases in diameter. Under the ensemble conditions, sulfidation stops at an intermediated stage, with a Ag nanosphere core remaining. Under the single-particle conditions, sulfidation is complete, with Ag being completely converted into Ag_2S. To the best of my knowledge, the concepts and experimental data presented here is the first to make use of the sensitivities of localized surface plasmon resonance to unravel the mechanism of a chemical reaction. It is also the first time that FDTD is extensively used to model dynamic structural changes occurring during the sulfidation of Ag nanocubes. Therefore, I believed that this study provides an elegant example for employing localized surface plasmon resonance to monitor and guide the chemical transformation of colloidal metal nanocrystals into more complicated hybrid nanostructures with desired plasmonic properties. In particular, the results gained from our study will be useful for preparing Ag/Ag_2S hybrid nanostructures with interesting plasmonic properties from various colloidal Ag nanocrystals.

References

[1] Stewart, M. E.; Anderton, C. R.; Thompson, L. B.; Maria, J.; Gray, S. K.; Rogers, J. A.; Nuzzo, R. G. *Chem. Rev.* **2008**, *108*, 494–521.

[2] Anker, J. N.; Hall, W. P.; Lyandres, O.; Shah, N. C.; Zhao, J.; Van Duyne, R. P. *Nat. Mater.* **2008**, *7*, 442–453.

[3] Chen, H. J.; Ming, T.; Zhao, L.; Wang, F.; Sun, L.-D.; Wang, J. F.; Yan, C.-H. *Nano Today* **2010**, *5*, 494–505.

[4] Charles, D. E.; Aherne, D.; Gara, M.; Ledwith, D. M.; Gun'ko, Y. K.; Kelly, J. M.; Blau, W. J.; Brennan-Fournet, M. E. *ACS Nano* **2010**, *4*, 55–64.

[5] Yanik, A. A.; Cetin, A. E.; Huang, M.; Artar, A.; Mousavi, S. H.; Khanikaev, A.; Connor, J. H.; Shvets, G.; Altug, H. *Proc. Natl. Acad. Sci. U.S.A.* **2011**, *108*, 11784–11789.

[6] Lee, Y. H.; Chen, H. J.; Xu, Q.-H.; Wang, J. F. *J. Phys. Chem. C*. **2011**, *115*, 7997–8004.

[7] Zhang, Q.; Ge, J. P.; Pham, T.; Goebl, J.; Hu, Y. X.; Lu, Z. D.; Yin, Y. D. *Angew. Chem. Int. Ed*. **2009**, *48*, 3516–3519.

[8] Goebl, J.; Zhang, Q.; He, L.; Yin, Y. D. *Angew. Chem. Int. Ed*. **2012**, *51*, 552–555.

[9] Meng, Z.-D.; Ghosh, T.; Zhu, L.; Choi, J.-G.; Park, C.-Y.; Oh, W.-C. *J. Mater. Chem.* **2012**, *22*, 16127–16135.

[10] Nagasuna, K.; Akita, T.; Fujishima, M.; Tada, H. *Langmuir* **2011**, *27*, 7294–7300.

[11] Yan, L.; Jia, H. M.; He, W. W.; Zhang, Y. G.; Mi, L. W.; Hou, H. W.; Zhu, G. S.; Zheng, Z. *J. Am. Chem. Soc.* **2012**, *134*, 17392–17395.

[12] Chang, S.; Li, Q.; Xiao, X. D.; Wong, K. Y.; Chen, T. *Energy Environ. Sci.* **2012**, *5*, 9444–9448.

[13] Wu, J.-J.; Chang, R.-C.; Chen, D.-W.; Wu, C.-T. *Nanoscale* **2012**, *4*, 1368–1372.

[14] Shao, L.; Woo, K. C.; Chen, H. J.; Jin, Z.; Wang, J. F.; Lin, H.-Q. *ACS Nano* **2010**, *4*, 3053–3062.

[15] Zhang, Y.; Hong, G. S.; Zhang, Y. J.; Chen, G. C.; Li, F.; Dai, H. J.; Wang, Q. B. *ACS Nano* **2012**, *5*, 3695–3702.

[16] Hong, G. S.; Robinson, J. T.; Zhang, Y. J.; Diao, S.; Antaris, A. L.; Wang, Q. B.; Dai, H. J. *Angew. Chem. Int. Ed.* **2012**, *51*, 9818–9821.

[17] Jiang, P.; Tian, Z.-Q.; Zhu, C.-N.; Zhang, Z.-L.; Pang, D.-W. *Chem. Mater.* **2012**, *24*, 3–5.

[18] Wang, C. X.; Wang, Y.; Xu, L.; Zhang, D.; Liu, M. X.; Li, X. W.; Sun, H. C.; Lin, Q.; Yang, B. *Small* **2012**, *8*, 3137–3142.

[19] Du, Y. P.; Xu, B.; Fu, T.; Cai, M.; Li, F., Zhang, Y.; Wang, Q. B. *J. Am. Chem. Soc*. **2010**, *132*, 1470–1471.

[20] Hodes, G.; Manassen, J.; Cahen, D. *Nature* **1976**, *261*, 403–404.

[21] Morales-Masis, M.; van der Molen, S. J.; Hasegawa, T.; van Ruitenbeek, J. M. *Phys. Rev. B* **2011**, *84*, 115310.

[22] Liang, C. H.; Terabe, K.; Hasegawa, T.; Negishi, R.; Tamura, T.; Aono, M. *Small* **2005**, *1*, 971–975.

[23] Xu, Z.; Bando, Y.; Wang, W. L.; Bai, X. D.; Golberg, D. *ACS Nano* **2010**, *4*, 2515–2522.

[24] Wang, R. Y.; Tangirala, R.; Raoux, S.; Jordan-Sweet, J. L.; Milliron, D. J. *Adv. Mater. Chem. Int. Ed.* **2012**, *51*, 11501–11504.

[26] Liu, B.; Ma, Z. F. *Small* **2011**, *7*, 1587–1592.

[27] Pang, M. L.; Hu, J. Y.; Zeng, H. C. *J. Am. Chem. Soc.* **2010**, *132*, 10771–10785.

[28] Zeng, J.; Tao, J.; Su, D.; Zhu, Y. M.; Qin, D.; Xia, Y. N. *Nano Lett*. **2011**, *11*, 3010–3012.

[29] Park, G.; Lee, C.; Seo, D.; Song, H. *Langmuir* **2012**, *28*, 9003–9009.

[30] Fang, C. H.; Lee, Y. H.; Shao, L.; Jiang, R. B.; Wang, J. F.; Xu, Q.-H. *ACS Nano* **2013**, *7*, 9354–9365.

[31] Tao, A.; Sinsermsuksakul, P.; Yang, P. D. *Angew. Chem. Int. Ed.* **2006**, *45*, 4597–4601.

[32] Zhang, Q.; Li, W. Y.; Moran, C.; Zeng, J.; Chen, J. Y.; Wen, L.-P.; Xia, Y. N. *J.*

Am. Chem. Soc. **2010**, *132*, 11372–11378.

[33] Jiang, R. B.; Chen, H. J.; Shao, L.; Li, Q.; Wang, J. F. *Adv. Mater.* **2012**, *24*, OP200–OP207.

[34] Nørskov, J. K.; Bligaard, T.; Hvolbæk, B.; Abild-Pedersen, F.; Chorkendorff, I.; Christensen, C. H. *Chem. Soc. Rev.* **2008**, *37*, 2163–2171.

[35] Kou, X. S.; Sun, Z. H.; Yang, Z.; Chen, H. J.; Wang, J. F. *Langmuir* **2009**, *25*, 1692–1698.

[36] Liang, C. H.; Terabe, K.; Hasegawa, T.; Aono, M. *Nanotechnology* **2007**, *18*, 485202.

[37] Shao, L.; Fang, C. H.; Chen, H. J.; Man, Y. C.; Wang, J. F.; Lin, H.-Q. *Nano Lett.* **2012**, *12*, 1424–1430.

[38] Bennett, J. M.; Stanford, J. L.; Ashley, E. J. *J. Opt. Soc. Am.* **1970**, *60*, 224–232.

Chapter 4

(Au Core)/(TiO$_2$ Shell) Nanostructures for Plasmon-Enhanced Light Harvesting and Reactive Oxygen Species Generation under Visible Light

In Chapter 3, I described my work on the metal/semiconductor nanostructures that are the integration of narrow-band-gap Ag$_2$S and Ag nanocubes. Another important plasmonic metal/semiconductor nanoscale system that I studied is a hybrid between wide-band-gap TiO$_2$ and Au nanocrystals. Herein, I will present this work in this chapter. TiO$_2$, one component of this hybrid, is one of the most important semiconductors with a band gap of around 3.2 eV. It has been extensively studied for a variety of applications ranging from photocatalysis, photovoltaic cells, and electrochromic devices to biological sciences by virtue of its low toxicity, biological compatibility, chemical and thermal stability, resistance to photocorrosion, and relative abundance [1]. However, the photocatalytic activity of TiO$_2$ is limited to the UV region because of its wide band gap. To improve the photocatalytic activity of TiO$_2$, a number of methods have been developed to enable it to harvest visible light, including doping with metal or non-metal ions, sensitizing with organic dyes or metal complexes, and coupling with other semiconductor nanostructures [2]. Localized surface plasmon resonance (LSPR) offers new opportunities for harvesting visible-to-near-infrared light [3]. The reasons have been described in detail in Chapter 1. In general, the LSPR wavelengths of metal nanocrystals can be synthetically tailored over a wide spectral range from the UV through visible to near-infrared region by changing the material, shape, and size. At the LSPR wavelength, metal nanocrystals possess extremely large absorption and scattering cross-sections. Moreover, they can focus light tightly in the nanoscale region around their surface [4].

These capabilities make them highly attractive for enhancing the photon harvesting of adjacent semiconductor nanocrystals over a broad spectral range. Several enhancement mechanisms have been proposed in previous studies [5–7], which has also been systematically described in Chapter 1. As a result, plasmonic metal nanocrystals are ideal candidates for enhancing the photon harvesting of TiO_2 in photovoltaics and photocatalysis through the formation of metal/semiconductor hybrid nanostructures [8,9].

Au nanocrystals with fascinating LSPR properties have been flourishing in nanoscience and nanotechnology. One remarkable feature of Au nanocrystals is that the synthetic methods for tuning their LSPR properties have been well developed and are highly reproducible. In addition, Au nanocrystals are chemically more stable than other metal nanocrystals, for example, Ag nanocrystals that are employed in Chapter 3. Hybridization of Au nanocrystals with TiO_2 nanostructures has been demonstrated in a number of experiments either by the co-precipitation of the oxide and Au precursors or anchoring pre-grown Au nanocrystals on the surface of TiO_2 nanostructures [10,11]. Although superior photocatalytic activities have been demonstrated with these hybrid Au/TiO_2 nanomaterials, the incorporated Au nanocrystals are usually exposed to the surrounding environment. They tend to aggregate, reshape, or grow into large particles, leading to a loss of their original plasmonic properties. When Au nanocrystals are directly grown on TiO_2 nanostructures, their shapes and sizes are difficult to be made uniform. In contrast, coating TiO_2 on pre-grown Au nanocrystals to form (Au core)/(TiO_2 shell) nanostructures can circumvent the aforementioned problems. Moreover, the core/shell nanostructure increases the active interfacial area between the two materials, which is beneficial for plasmon-enhanced light absorption and plasmon-induced hot-electron injection.

Although the coating of SiO_2 on pre-grown metal nanocrystals has been realized in a number of studies [12–15], the extension to TiO_2 has been difficult and challenging.

To date, the coating of TiO_2 on Au nanocrystals has only been demonstrated in a few experiments and has been limited with Au nanospheres or nanooctahedrons, which have LSPR bands located at ~540 nm [16–18]. For example, a sol-gel-based protocol has been developed to prepare (Au nanosphere core)/(TiO_2 shell) and (SiO_2 nanosphere core)/(Au nanoparticle shell)/(TiO_2 shell) nanostructures by employing SiO_2 as a sacrificial layer or template [19,20]. Compared with Au nanospheres, Au nanorods offer more attractive plasmonic features. The anisotropic nature of Au nanorods brings about stronger electric field enhancements and can trap more light, in comparison to Au nanospheres with the same particle volume [5]. In addition, because the longitudinal plasmon wavelength of Au nanorods can be synthetically tailored over the visible to near-infrared region by changing the aspect ratio [21], the use of Au nanorods can extend the photon-response of TiO_2 to the visible and even near-infrared regions, hence largely improving its light harvesting capability [22]. For example, TiO_2 electrodes that are decorated with Au nanorods have recently been shown to give a higher water-splitting efficiency than those decorated with Au nanospheres [23]. However, coating TiO_2 on Au nanorods has rarely been demonstrated and therefore is still a challenge [24].

During my PhD study, I have developed a general method to prepare (Au nanorod core)/(TiO_2 shell) nanostructures using the "seeded growth" method. The nanostructures with various Au nanorod core sizes and TiO_2 shell thicknesses have been successfully prepared. The same method has also been employed to successfully grow TiO_2 shell onto other monometallic and bimetallic Pd, Pt, and Au nanocrystals. The detailed preparation and characterizations of the (metal core)/(TiO_2 shell) nanostructures will be presented in *Section 4.1*. The superior plasmonic properties and the synergistic effects between the metal core and the TiO_2 shell make the (Au core)/(TiO_2 shell) nanostructure a multifunctional nanomaterial. I therefore investigated its applications in dye-sensitized solar cells (DSSCs) and reactive oxygen species (ROS) generation (*Section 4.2*). The (Au nanorod core)/(TiO_2 shell) nanostructures were utilized as a scattering layer in DSSCs. The plasmon-enhanced

ROS generation, including singlet oxygen ($^1O_2$) and hydroxyl radicals ($\cdot$OH), with the presence of (Au nanorod core)/(TiO$_2$ shell) nanostructures were also examined.

4.1 Preparation and Characterization of the Nanostructures

During my study, I first examined this method by coating TiO$_2$ on pre-grown Au nanocrystals, including Au nanospheres and Au nanorods with various sizes. This method can also be applied to other noble metal nanocrystals. In this section, I will therefore introduce the preparation and characterization of the (metal core)/(TiO$_2$ shell) nanostructures in two parts, which are (Au nanocrystal core)/(TiO$_2$ shell) nanostructures in *Section 4.1.1* and core/shell nanostructures using Pd, Pt, and Au-based bimetallic nanocrystals as the cores in *Section 4.1.2*.

4.1.1 (Au Nanocrystal Core)/(TiO$_2$ Shell) Nanostructures

The (Au nanocrystal core)/(TiO$_2$ shell) nanostructures were produced by coating TiO$_2$ on pre-grown gold nanocrystals. Monometallic Au nanospheres and nanorods were pre-grown with cationic cetyltrimethylammonium bromide (CTAB) as a stabilizing surfactant. The use of pre-grown Au nanocrystals allows their shapes, sizes, and hence their plasmonic properties to be rationally controlled. Au nanocrystals were first encapsulated with an anionic poly(sodium 4-styrenesulfonate) (PSS, MW 7×10^4 g mol^{-1}) layer according to a modified layer-by-layer assembly method [25]. The negatively charged PSS layer facilitates the adsorption of the positively charged Ti^{3+} species, which are subsequently oxidized into TiO$_2$ in aqueous solutions in air at room temperature [28–30]. The electrostatic adsorption enabled by the conversion from positive to negative charges on the nanocrystal surface through PSS encapsulation promotes the successful deposition of TiO$_2$. The general process is illustrated in Figure 4.1 using the (Au nanorod core)/(TiO$_2$ shell) nanostructure as an example.
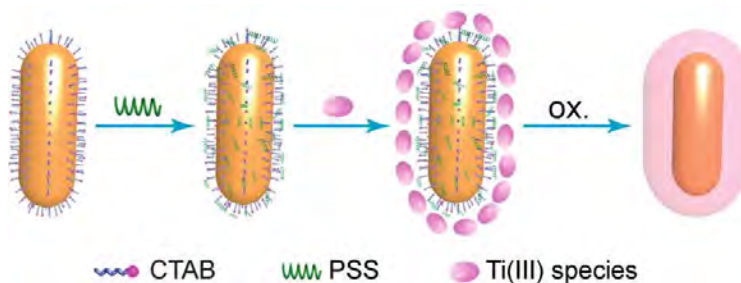
Figure 4.1 Schematic describing the coating of TiO_2 onto a Au nanorod to produce a (Au nanorod core)/(TiO_2 shell) nanostructure.

For a typical preparation process, the noble metal nanocrystal samples were made according to the detailed procedures that were presented in Chapter 2. The metal nanocrystals were first wrapped with PSS molecules. The as-grown metal nanocrystal sample in the solution (10 mL) that was stabilized with either CTAB or cetyltrimethylammonium chloride (CTAC) was washed once by centrifugation to remove the excess surfactant and then redispersed into water (10 mL). The resultant metal nanocrystal solution was added dropwise under vigorous stirring to an aqueous PSS solution (10 mL, 2 g L^{-1}, containing 6 mM NaCl). PSS adsorption was allowed for at least 4 h at room temperature. After the excess PSS molecules were removed by centrifugation, the PSS-encapsulated metal nanocrystals were redispersed into water (200 μL). The concentration of the PSS molecules remaining in the obtained metal nanocrystal solution was estimated to be ~0.05 g L^{-1}. It should be noticed that the concentration of the PSS molecules remaining in the nanocrystal solution should be below ~0.20 g L^{-1} to avoid the self-growth of TiO_2. For the preparation of the (metal core)/(TiO_2 shell) nanostructures, $TiCl_3$ solution (200 μL, 17.1 wt%, containing 20–30 wt% HCl) and water (6 mL) were first added into a glass bottle. $NaHCO_3$ solution (0.93 M, 1.2 mL) was then dropped, followed by the immediate addition of the PSS-encapsulated metal nanocrystal solution under stirring. After the mixture solution was stirred for 30 min at room temperature, the product was washed by centrifugation twice and redispersed in water (10 mL) before further use.
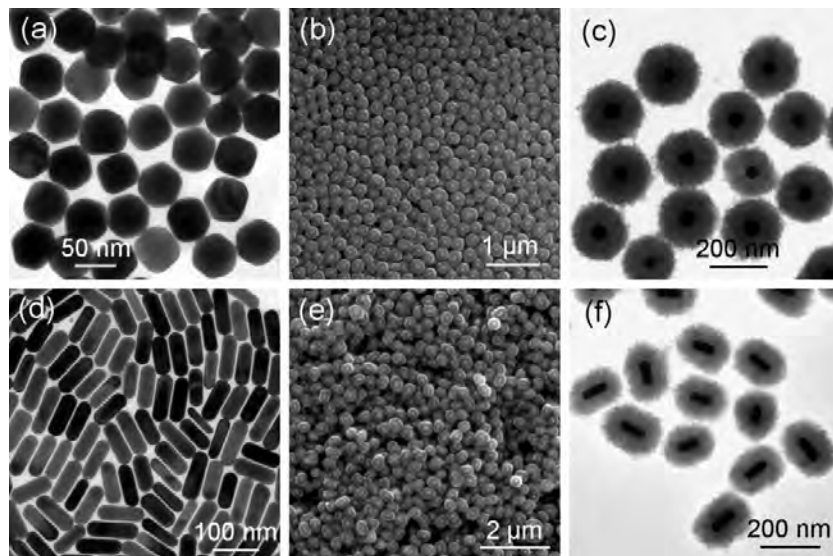
Figure 4.2 (Au nanosphere core)/(TiO$_2$ shell) and (Aunanorod core)/(TiO$_2$ shell) nanostructures. (a) TEM image of the uncoated Au nanosphere sample. (b,c) SEM and TEM images of the (Au nanosphere core)/(TiO$_2$ shell) nanostructures, respectively. (d) TEM image of the uncoated Au nanorod sample. (e,f) SEM and TEM images of the (Au nanorod core)/(TiO$_2$ shell) nanostructures, respectively.

The core/shell nanostructures produced from the TiO$_2$ coating on nearly monodisperse Au nanospheres and nanorods are displayed in Figure 4.2. The Au nanosphere sample has an average diameter of 58 ± 5 nm (Figure 4.2a), and the Au nanorod sample has an average size of 91 ± 8 nm by 32 ± 4 nm (Figure 4.2d). Their particle concentrations are estimated to be 0.12 nM and 0.14 nM, respectively. As shown by scanning electron microscopy (SEM) and transmission electron microscopy (TEM) imaging, when Au nanospheres are used as the cores, the resultant core/shell nanostructures are in a spherical shape, with TiO$_2$ being uniformly coated at a thickness of 64 ± 9 nm (Figure 4.2b and c). When Au nanorods are employed as the cores, the produced core/shell nanostructures are rod-like with narrow size distributions (Figure 4.2e). Compared with the uncoated Au nanorods, the (Au nanorod core)/(TiO$_2$ shell) nanostructures show distinct contrast between the core and peripheral shell regions under TEM imaging (Figure 4.2f), which is typical for nanomaterials with a core/shell structure. The darker core is expected to be a Au

- 104 -

nanorod, while the shell made of TiO_2 appears lighter. The TiO_2 shell is seen to be relatively uniform in thickness around the core in each nanostructure as well as on different nanostructures. The average shell thickness is measured to be 53 ± 6 nm. The shell is in close contact with the Au core and appears rough on the outer surface. It is probably composed of TiO_2 nanoparticles that are aggregated together tightly. The formation of the core/shell nanostructures is further verified by high-angle annular dark-field scanning transmission microscopy (HAADF-STEM) imaging (Figure 4.3a), energy-dispersive X ray (EDX) elemental mapping (Figure 4.3b–d) and line profiling (Figure 2e). EDX elemental mapping reveals that the core is made of Au and the shell is composed of Ti and O. From the line profiles, Both Ti and O have two peaks and a valley between them, while Au has only one peak, which spatially overlaps with the valleys on the Ti and O profiles. These features suggest strongly the formation of a core/shell nanostructure. The similar features are also observed from EDX elemental mapping and line profiling on the (Au nanosphere core)/(TiO2 shell) nanostructures (Figure 4.4a–e).
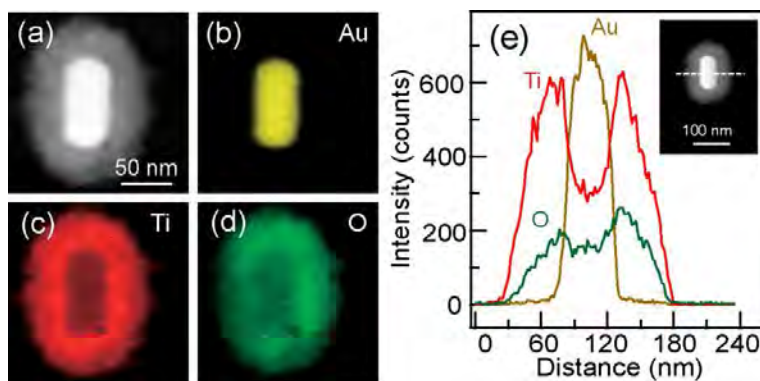
Figure 4.3 Elemental mapping of the (Au nanorod core)/(TiO2 shell) nanostructures. (a) HAADF-STEM image of a single core/shell nanostructure. (b–d) Elemental maps of Au, Ti, and O on the nanostructure shown in (a), respectively. The scale bar in (a) also applies for (b–d). (e) Elemental profiles of Au, Ti, and O acquired along the dashed line indicated on the HAADF-STEM image in the inset.
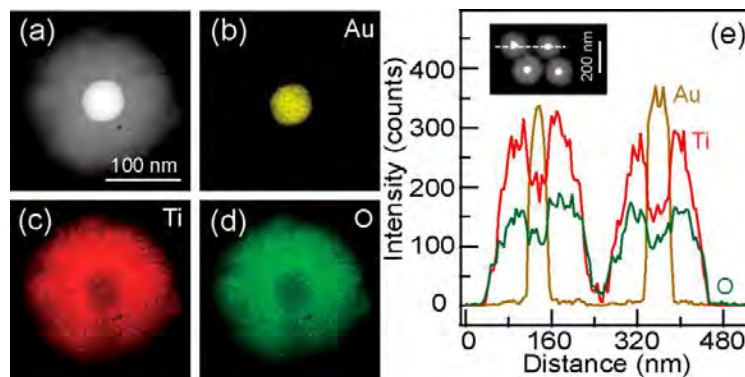
Figure 4.4 Elemental mapping of the (Au nanosphere core)/(TiO₂ shell) nanostructures. (a) HAADF-STEM image of a single core/shell nanostructure. (b–d) Elemental maps of Au, Ti, and O on the nanostructure shown in (a), respectively. The scale bar in (a) also applies for (b–d). (e) Elemental profiles of Au, Ti, and O acquired along the dashed line indicated on the HAADF-STEM image in the inset.
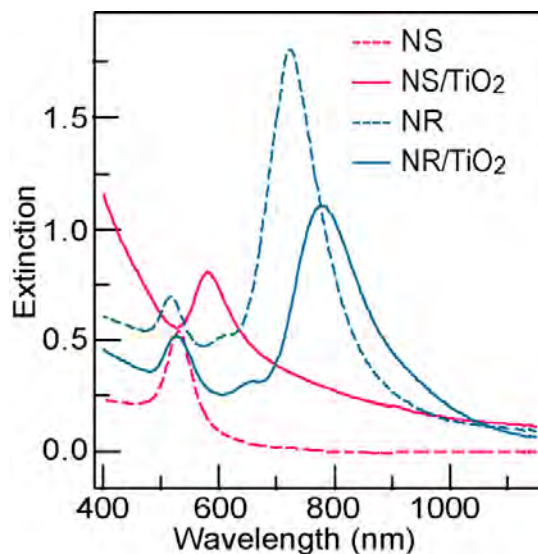
Figure 4.5 Extinction spectra of the uncoated Au nanocrystal samples (dashed lines) and the corresponding core/shell nanostructure samples (solid lines).

The effect of TiO₂ coating on the optical response is shown in Figure 4.5. For the (Au nanosphere core)/(TiO₂ shell) nanostructures, the LSPR peak is seen to red-shift from 531 nm to 580 nm with a concomitant increase in the peak intensity by 48%. For the (Au nanorod core)/(TiO₂ shell) nanostructures, the transverse and longitudinal plasmon peaks red-shift from 516 nm to 529 nm and from 724 nm to 781 nm,

respectively. The longitudinal plasmon peak is red-shifted by 57 nm, with an intensity decrease by 38%. The red shifts in the extinction peaks are caused by a refractive-index increase of the surrounding medium after TiO_2 coating. The increase in the peak intensity and the rising background towards the short-wavelength region on the extinction spectrum of the (Au nanosphere core)/(TiO_2 shell) nanostructures are mainly caused by the increased scattering due to the larger size of the core/shell nanostructures and the scattering from the TiO_2 shell, respectively [29].The asymmetric profile of the extinction spectrum is believed to arise from the Fano resonance between the core and shell [30], which will be introduced in Chapter 5. The extinction intensity decrease of the (Au nanorod core)/(TiO_2 shell) nanostructures is believed to be caused by particle loss during centrifugation, which outweighs the intensity increase caused by the size enlargement after the formation of the nanostructures.
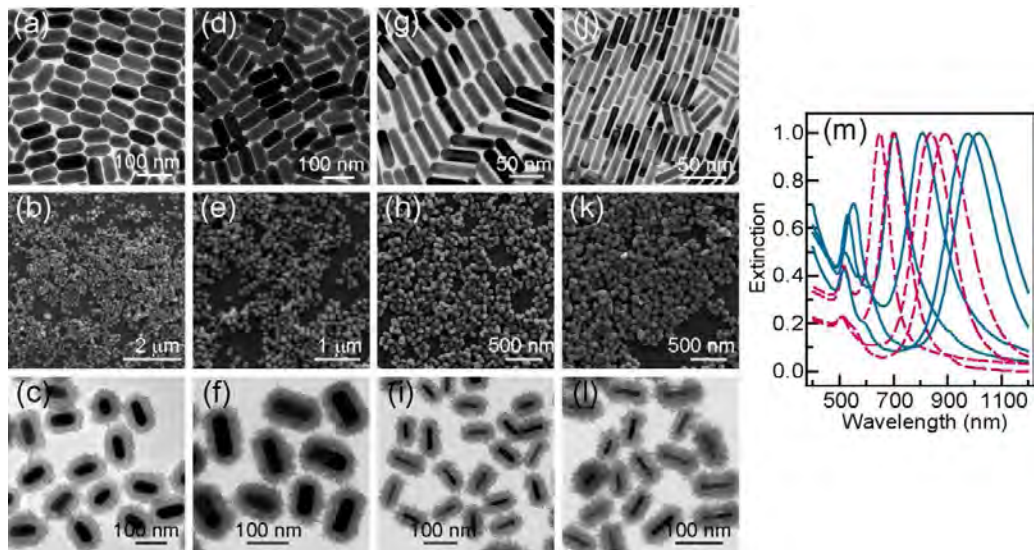
Figure 4.6 (Au nanorod core)/(TiO_2 shell) nanostructures produced from differently sized Au nanorods. (a,d,g,j) TEM images of the Au nanorod samples with longitudinal plasmon wavelengths of 650 nm, 700 nm, 838 nm, and 890 nm, respectively. (b,e,h,k) SEM images of the corresponding core/shell nanostructure samples. (c,f,i,l) TEM images of the corresponding core/shell nanostructure samples. (m) Normalized extinction spectra of the uncoated Au nanorod samples (red dashed

lines) and the corresponding nanostructure samples (blue solid lines). The extinction spectra of the samples can be identified according to the longitudinal plasmon wavelength.

The LSPR of a metal nanocrystal is very sensitive to its composition, shape, size, and dielectric environment. The LSPR of the (Au nanocrystal core)/(TiO$_2$ shell) nanostructure is therefore dependent on both the Au nanocrystal core and the TiO$_2$ shell. Au nanorod samples with the longitudinal plasmon wavelength varied from 650 nm to 890 nm have been utilized as the cores (Figure 4.6). Their sizes are measured to be 87 ± 6 nm by 38 ± 3 nm, 94 ± 6 nm by 41 ± 3 nm, 60 ± 7 nm by 16 ± 1 nm, and 68 ± 5 nm by 15 ± 1 nm, respectively from the TEM images of the uncoated Au nanorod samples. The SEM and TEM images of the products show unambiguously the successful coating of TiO$_2$ shell on Au nanorods. The shell thicknesses of the four core/shell nanostructure samples are measured to be 30 ± 5 nm, 32 ± 4 nm, 23 ± 4 nm, and 20 ± 3 nm, respectively. The coating is also confirmed by the clearly observable red shift of the longitudinal plasmon peak for each Au nanorod sample. The longitudinal plasmon wavelengths of the core/shell nanostructure samples are varied from 700 nm to 1020 nm (Figure 4.6m). In addition, the average thickness of the TiO$_2$ shell can be readily varied by controlling the reaction time (Figure 4.7), the added amounts of NaHCO$_3$ (Figure 4.8) and TiCl$_3$ (Figure 4.9). The Au nanorods sample has a longitudinal plasmon wavelength of 716 nm and a transverse plasmon wavelength of 512 nm. The particle concentrations have been adjusted to be the same for all the samples so that the extinction peak intensities can be compared. The time-dependent extinction is shown in Figure 4.7a, which is obtained by fixing the amount of TiCl$_3$ (200 μL) and NaHCO$_3$ (1.2 mL). The longitudinal and transverse plasmon peaks are red-shifted to 858 nm and 571 nm, respectively, at 30 min after the coating reaction was started. After that, the plasmon peaks remain nearly unchanged. The thicknesses of the shells are measured to be 25 ± 2 nm, 53 ± 7nm, and 59 ± 7 nm, respectively from the TEM images of the products that were collected at 0.5 min, 15 min, and 50min (Figure 4.7b–d). When the reaction time is fixed at 30 min and the amount of

- 108 -

TiCl$_3$ is 200 μL, and the volume of NaHCO$_3$ solution is varied from 1.1 mL to 1.4 mL, the longitudinal plasmon peak is red-shifted to 806 nm, 834 nm, 871 nm, and 879 nm, respectively (Figure 4.8a). The transverse plasmon peak is red-shifted from 512 nm to 573 nm. The thicknesses of the shells are increased from 32 ± 3 nm to 104 ± 9 nm, respectively (Figure 4.8b and c). Figure 4.9 displays the effect of the amount of the TiCl$_3$ precursor. The longitudinal plasmon peak is red-shifted from 716 nm to 854 nm when 200 μL of the TiCl$_3$ solution is used. When the volume of the TiCl$_3$ solution is increased to 500 μL, only a slight red shift to 861 nm is observed. At the same time, the transverse plasmon peak is red-shifted from 512 nm to 563 nm when 200 μL of the TiCl$_3$ solution is added. The transverse plasmon peak is further red-shifted to 566 nm when the volume of the TiCl$_3$ solution is increased to 500 μL. The thicknesses of the shells are measured to be 48 ± 7 nm, 53 ± 8 nm, 59 ± 7 nm, and 68 ± 8 nm, respectively. The shell thickness variation also allows the longitudinal plasmon wavelength to be finely tailored for a given Au nanorod core sample.
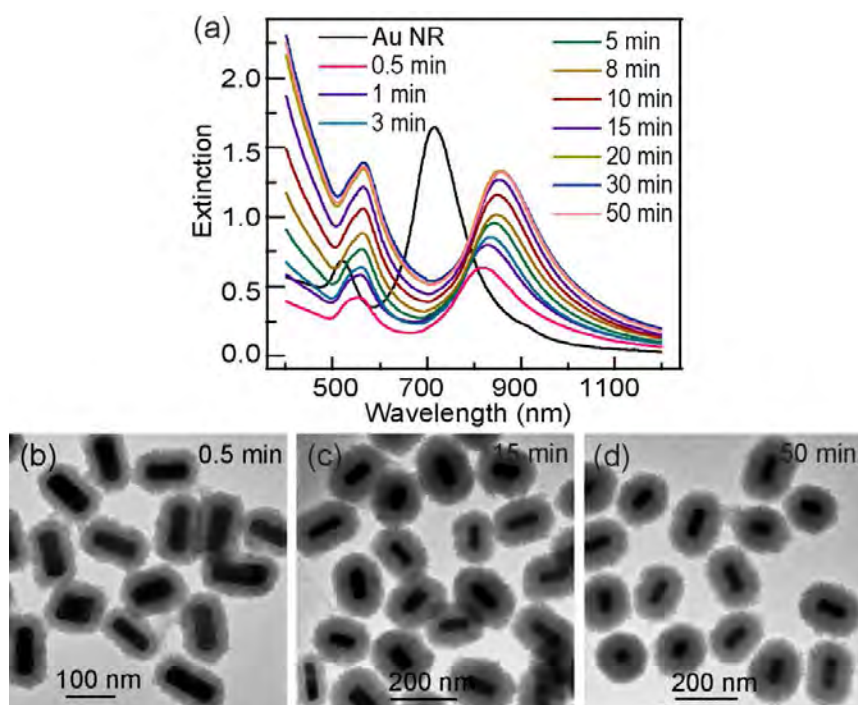
Figure 4.7 Time-dependent variations in the extinction spectrum and the shell thickness for the coating of a Au nanorod sample. (a) Extinction spectra recorded as a function of time after the addition of the PSS-encapsulated Au nanorod solution into

the TiCl₃ solution. (b–d) Representative TEM images of the (Au nanorod core)/(TiO₂ shell) nanostructure samples collected at 0.5 min, 15 min, and 50 min, respectively, after the coating reaction was started.
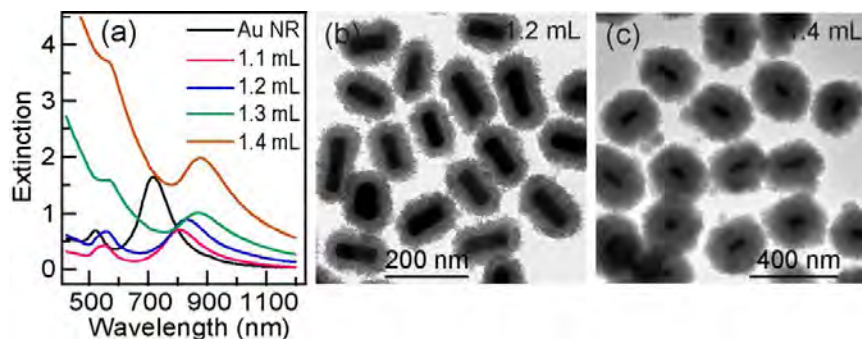
Figure 4.8 Effect of the added amount of NaHCO₃ on the TiO₂ coating. (a) Extinction spectra of the products obtained when varying amounts of NaHCO₃ were employed in the coating. (b,c) Representative TEM images of the (Au nanorod core)/(TiO₂ shell) nanostructures produced when 1.2 mL and 1.4 mL of the NaHCO₃ solution were used for the coating, respectively.
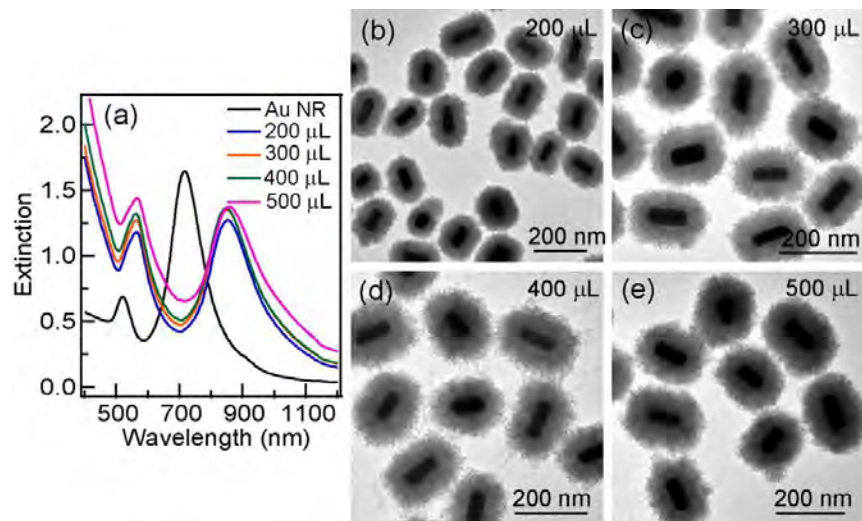
Figure 4.9 Effect of the amount of TiCl₃ on the TiO₂ coating. (a) Extinction spectra of the products obtained when varying amounts of TiCl₃ were employed for the coating. (b–e) Representative TEM images of the (Au nanorod core)/(TiO₂ shell) nanostructures made when 200 μL, 300 μL, 400 μL, and 500 μL of the TiCl₃ solution were employed, respectively, while the volume of the NaHCO₃ solution was kept

unchanged at 1.2 mL. The coating reaction was allowed to proceed for 30 min.

X-ray photoelectron spectroscopy (XPS) and X-ray diffraction (XRD) were used to characterize the elements and crystalline phases of a representative (Au nanorod core)/(TiO$_2$ shell) nanostructure sample. The XPS survey spectrum (Figure 4.10a) indicates that the nanostructures are composed of Au, Ti, and O. The detected C signal is believed to come from the CTAB and PSS molecules adsorbed on the surface of the Au nanorods. The high-resolution XPS spectrum of Ti 2p exhibits two strong peaks located at 458.65 eV and 464.5 eV, which correspond to Ti 2p3/2 and Ti 2p1/2, respectively. The measured binding energies of Ti 2p indicate that Ti dominantly exists in the form of Ti^{4+} (Figure 4.10b) [31]. The XPS spectrum of Au 4f shows that Au is existent in the metallic Au(0) state (Figure 4.10c). The XPS peak of O 1s is asymmetric, with a tail towards the high-energy region. The asymmetric shape was fitted into two peaks, corresponding to Ti–O (530.1 eV) and O–H (531.4 eV) (Figure 4.10d), respectively. The weaker O–H peak is attributed to the surface species, such as Ti–OH, which result from the reaction of the chemisorbed water with the Ti–species on the TiO$_2$ shell surface [32].
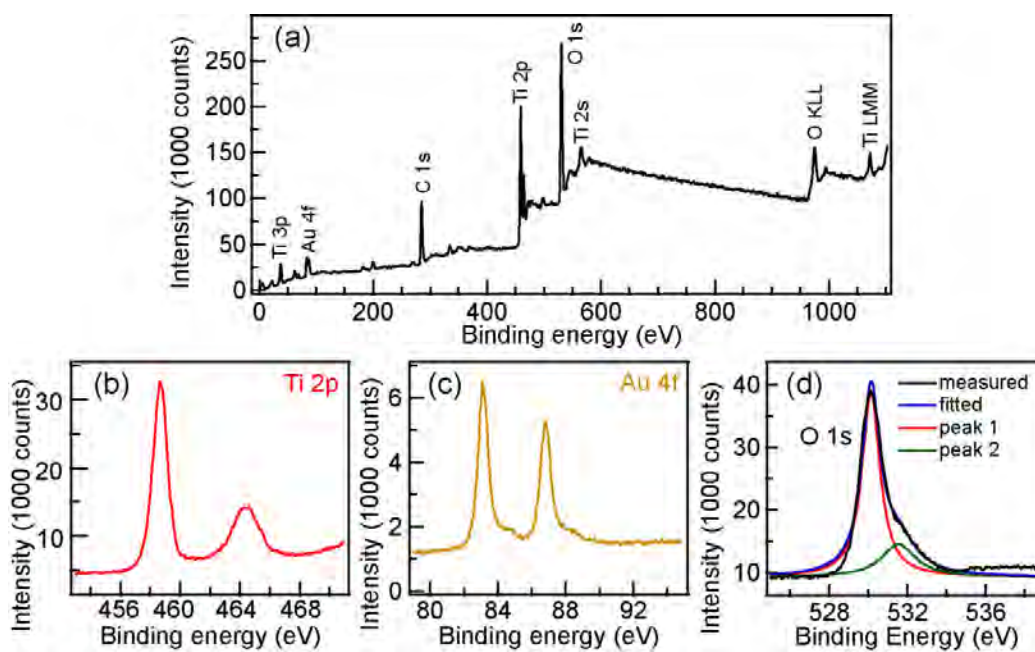
Figure 4.10 XPS characterization of a representative (Au nanorod core)/(TiO$_2$ shell)

nanostructure sample. (a) XPS survey spectrum of the as-prepared core/shell nanostructure sample. (b,c) High-resolution XPS spectra of Ti 2p and Au 4f, respectively. (c) High-resolution XPS spectrum of O 1s. The spectrum is fitted with two Lorentzian peaks. The coefficient of determination for the fitting is $R^2 = 0.9763$.

The XRD pattern (Figure 4.11a) taken on the as-prepared (Au nanorod core)/(TiO$_2$ shell) nanostructures shows only the diffraction peaks of the face-centered-cubic structure of Au, indicating that the TiO$_2$ shell formed at room temperature is amorphous. Thermal treatment carried out in a box furnace in air at 450 °C for 2 h with a ramp rate of 5 °C min^{-1} causes the amorphous shell to crystallize into anatase TiO$_2$, yet the morphology of the core/shell nanostructures is retained, as seen from Figure 4.12b and c. The crystallization causes shrinkage of the TiO$_2$ shell as well as increases its refractive index. The increase of the refractive index further red-shifts the plasmon peaks on the extinction spectrum (Figure 4.11d). The transverse and longitudinal plasmon wavelengths of the as-prepared nanostructure sample are 560 nm and 845 nm, respectively. After the thermal treatment, the corresponding wavelengths become 635 nm and 925 nm. The extinction peaks show slight broadening, which might be caused by slight aggregation of the core/shell nanostructures. A shoulder is also seen on the transverse plasmon peak at ~590 nm after the thermal treatment. The shoulder is suspected to be a higher-order plasmon resonance mode, which can be excited when the Au nanorods are coated with a high-index dielectric shell. The thermal treatment was also carried out for a (Au nanosphere core)/(TiO$_2$ shell) nanostructure sample. After the thermal treatment, the spherical morphology is retained, with a decrease in the shell thickness (Figure 4.11e and f). The crystallization of the TiO$_2$ shell induces a red shift of the plasmon resonance peak (Figure 4.11g)
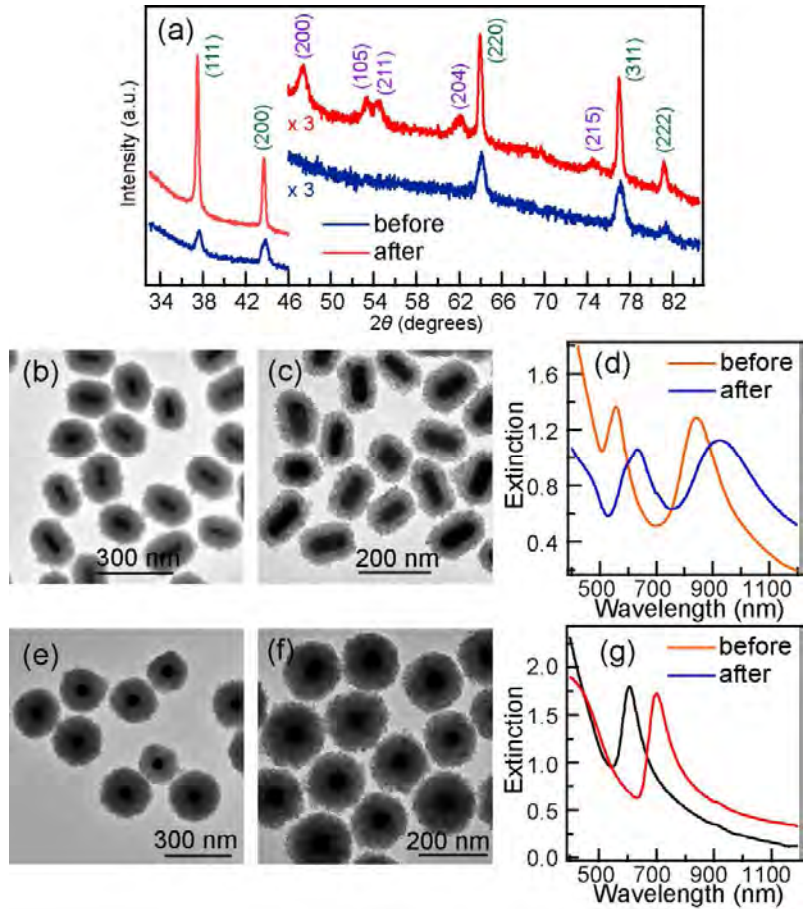
Figure 4.11 XRD characterization and thermal treatment of the (Au nanocrystal core)/(TiO$_2$ shell) nanostructures. (a) XRD patterns of the as-prepared and thermally treated (Au nanorod core)/(TiO$_2$ shell) nanostructure sample. The patterns are magnified in the high-angle region for better revealing the weak diffraction peaks. The diffraction peaks are indexed according to the faced-centered-cubic structure of Au (JCPDS 1-1172, green numbers) and the anatase phase of TiO$_2$ (JCPDS 21-1272, purple numbers). (b,c) TEM images of the (Au nanosphere core)/(TiO$_2$ shell) nanostructure sample before and after the thermal treatment, respectively. The measured sizes before the treatment are: core length, 98 $\pm$ 10 nm; core diameter, 46 $\pm$ 7 nm; shell thickness, 51 $\pm$ 9 nm. The measured sizes after the treatment are: core length, 96 $\pm$ 11 nm; core diameter, 51 $\pm$ 5 nm; shell thickness, 39 $\pm$ 4 nm. (e) Extinction spectra of the (Au nanorod core)/(TiO$_2$ shell) nanostructures before and after the thermal treatment. (f,g) TEM images of the (Au nanosphere core)/(TiO$_2$ shell)

nanostructure sample before and after the thermal treatment, respectively. The measured sizes before the treatment are: core diameter, 59 ± 6 nm; shell thickness, 77 ± 9 nm. The sizes after the treatment are: core diameter, 58 ± 6 nm; shell thickness, 64 ± 6 nm. (h) Extinction spectra of the (Au nanosphere core)/(TiO_2 shell) nanostructure sample before and after the thermal treatment.

4.1.2 Pd/TiO$_2$, Pt/TiO$_2$, Au/Pd/TiO$_2$, and Au/Pt/TiO$_2$ Nanostructures

The robust coating of TiO_2 has been demonstrated on variously sized Au nanocrystals, which exhibit intriguing, synthetically tunable LSPR properties. Other noble metals, such as Pd and Pt, are widely used as catalysts in petrochemical, pharmaceutical, and energy-related industries. It would be highly desirable to coat TiO_2 on Pd and Pt nanocrystals. Recent studies have shown that loading Pd nanoparticles on TiO_2 nanotube arrays increases the photon-to-current conversion efficiency to nearly 100% at 330 nm and promotes the photocatalytic H_2 production rate by 1.6-fold in comparison to the typical TiO_2 photoanode [33]. The catalytic performances of TiO_2 have been demonstrated to be improved in the presence of Pt nanoparticles [34,35]. However, the coating of TiO_2 on Pd and Pt nanocrystals has been rarely investigated [36]. Moreover, bimetallic nanocrystals, such as Au/Pd and Au/Pt, integrate together the plasmonic properties of Au nanocrystals and the excellent catalytic properties of Pd and Pt. They can not only widen the applications of plasmonics but also offer enhanced catalytic performances in comparison to monometallic nanocrystals [37,38]. Hybridization of such bimetallic nanocrystals with semiconductors, especially TiO_2, can therefore combine together LSPR, catalysis, and photocatalysis in one nanomaterial system, and is expected to offer great potential in photocatalysis, energy harvesting and utilization [39–41]. However, to the best of our knowledge, (bimetallic nanocrystal core)/(TiO_2 shell) nanostructures have not been reported yet.
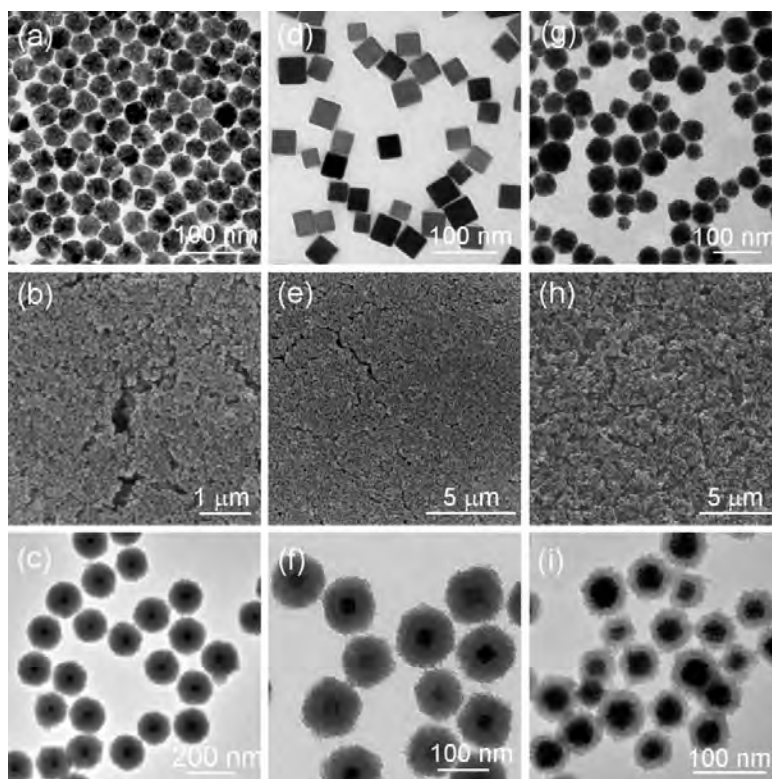
Figure 4.12 Electron microscopy images of the core/shell nanostructure samples with monometallic Pd and Pt nanocrystals as the cores. (a,d,g) TEM images of uncoated porous Pd, cubic Pd, and porous Pt nanocrystals, respectively. (b,e,h) SEM images of the (porous Pd nanocrystal core)/(TiO$_2$ shell), (cubic Pd nanocrystal core)/(TiO$_2$ shell), and (porous Pt nanocrystal core)/(TiO$_2$ shell) nanostructure samples, respectively. (c,f,i) TEM images of the (porous Pd nanocrystal core)/(TiO$_2$ shell), (cubic Pd nanocrystal core)/(TiO$_2$ shell), and (porous Pt nanocrystal core)/(TiO$_2$ shell) nanostructure samples, respectively.

Monometallic Pd, Pt nanocrystals and bimetallic Au/Pd, Au/Pt nanocrystals were utilized as the cores for TiO$_2$ coating. Both porous and solid Pd nanocrystals were employed. TEM imaging shows that the uncoated porous Pd nanocrystals have a nearly spherical shape, with a narrow size distribution (Figure 4.12a). The obtained core/shell nanostructures also have a spherical shape and are nearly monodisperse (Figure 4.12b and c). EDX elemental mapping reveals that the core is made of Pd and the shell is composed of Ti and O. Both Ti and O have two peaks and a valley

- 115 -

between them, while Pd has only one peak, which spatially overlaps with the valleys on the Ti and O profiles, as revealed by elemental mapping and line profiling (Figure 4.13). Similarly, cubic Pd nanocrystals (Figure 4.12d) can also be coated with TiO_2 shell, according to SEM, TEM imaging (Figure 4.12e and f) and elemental distribution characterization (Figure 4.14). Our method is also applicable to porous Pt nanocrystals (Figure 4.12g). Electron microscopy (Figure 4.12h and i) and elemental characterization (Figure 4.15) show clearly the formation of well-dispersed (porous Pt nanocrystal core)/(TiO_2 shell) nanostructures.
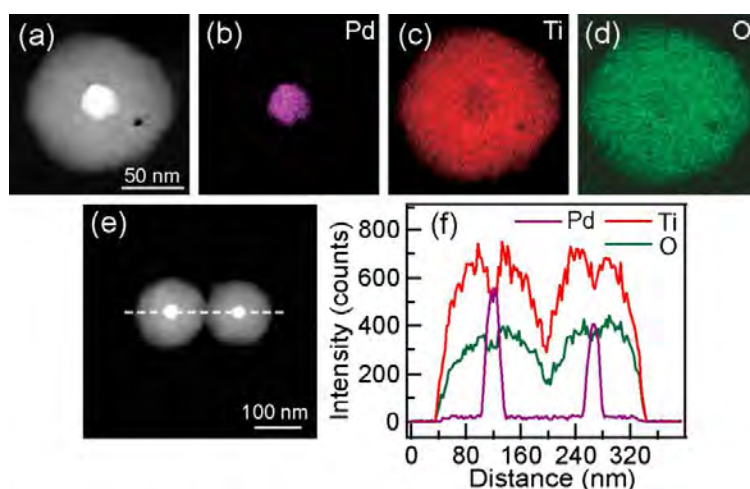
Figure 4.13 Elemental mapping of the (porous Pd nanocrystal core)/(TiO_2 shell) nanostructures. (a) HAADF-STEM image of a single core/shell nanostructure. (b–d) Elemental maps of Pd, Ti, and O on the nanostructure shown in (a), respectively. The scale bar in (a) also applies for (b–d). (e) HAADF-STEM images of the nanostructures. (f) Elemental profiles of Pd, Ti, and O acquired along the dashed line shown in (e).
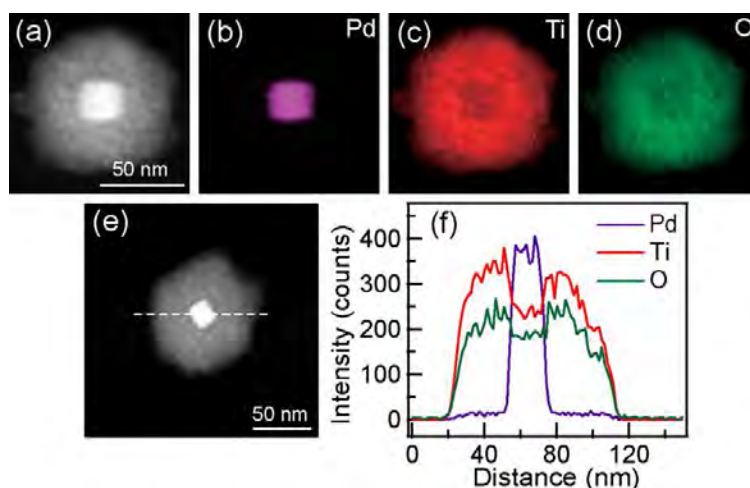
Figure 4.14 Elemental mapping of the (cubic Pd nanocrystal core)/(TiO$_2$ shell) nanostructures. (a) HAADF-STEM image of a single core/shell nanostructure. (b–d) Elemental maps of Pd, Ti, and O on the nanostructure shown in (a), respectively. The scale bar in (a) also applies for (b–d). (e) HAADF-STEM images of a single nanostructure for element profiling. (f) Elemental profiles of Pd, Ti, and O acquired along the dashed line shown in (e).
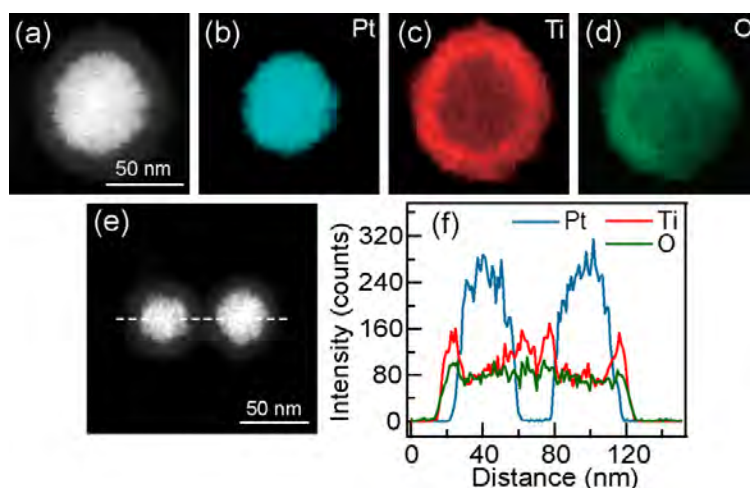
Figure 4.15 Elemental mapping of the (porous Pt nanocrystal core)/(TiO$_2$ shell) nanostructures. (a) HAADF-STEM image of a single core/shell nanostructure. (b–d) Elemental maps of Pt, Ti, and O on the nanostructure shown in (a), respectively. The scale bar in (a) also applies for (b–d). (e) HAADF-STEM images of two nanostructures. (f) Elemental profiles of Pt, Ti, and O acquired along the dashed line

- 117 -

shown in (e).

Three (Au nanorod)-based bimetallic nanocrystal samples were tested for TiO_2 coating. They are Au nanorods decorated with discrete Pd nanoparticles (Figure 4.16a), Au nanorods encapsulated with continuous Pd shell (Figure 4.16b), and Au nanorods decorated with discrete Pt nanoparticles (Figure 4.16c). During their preparations, CTAB or CTAC was employed as the stabilizing agent. These bimetallic nanocrystals can also be readily modified with negatively charged PSS. They are therefore compatible with our coating method. Low-magnification SEM imaging indicates that the produced core/shell nanostructure samples are relatively uniform in size (Figure 4.16d–f). The successful coating of TiO_2 on these bimetallic nanocrystals is also clearly shown by comparing the TEM images of the uncoated nanocrystal samples with those of the corresponding core/shell nanostructure samples (Figure 4.17g–i). EDX elemental mapping and profiling not only verify the formation of TiO_2 shell but also reveal that the morphologies of the bimetallic nanocrystals are preserved after the coating process (Figure 4.17–4.19).
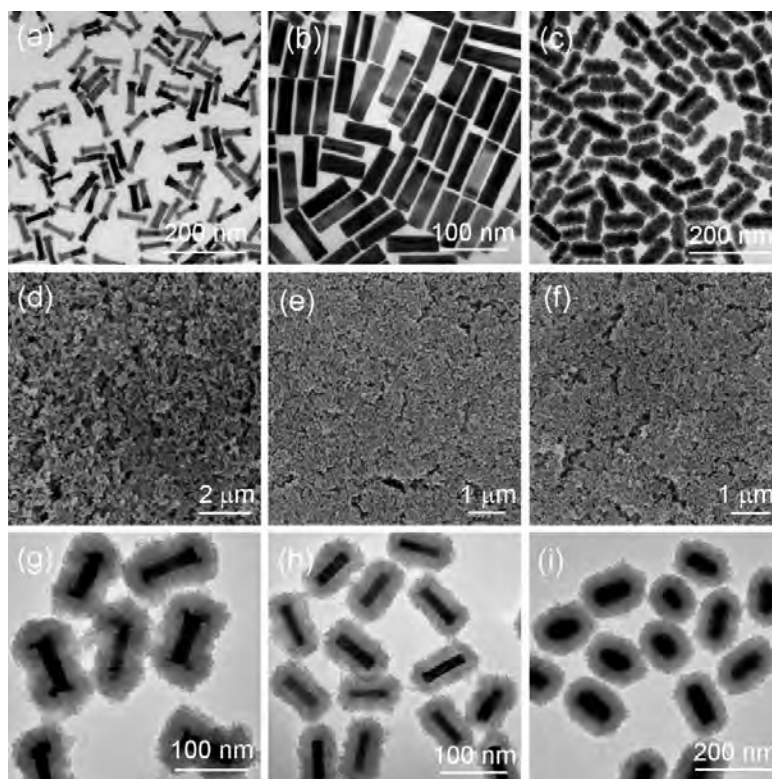
Figure 4.16 Electron microscopy images of the core/shell nanostructure samples with monometallic Pd and Pt nanocrystals as the cores. (a–c) TEM images of the uncoated (Au nanorod core)/(discontinuous Pd shell) nanocrystals, (Au nanorod core)/(continuous Pd shell) nanocrystals, and (Au nanorod core)/(Pt shell) nanocrystals, respectively. (d–f) SEM images of the (Au nanorod core)/(discontinuous Pd shell)/(TiO$_2$ shell) nanostructures, (Au nanorod core)/(continuous Pd shell)/(TiO$_2$ shell) nanostructures, and (Au nanorod core)/(Pt shell)/(TiO$_2$ shell) nanostructures, respectively. (g–i) TEM images of the (Au nanorod core)/(discontinuous Pd shell)/(TiO$_2$ shell) nanostructures, (Au nanorod core)/(continuous Pd shell)/(TiO$_2$ shell) nanostructures, and (Au nanorod core)/(Pt shell)/(TiO$_2$ shell) nanostructures, respectively.
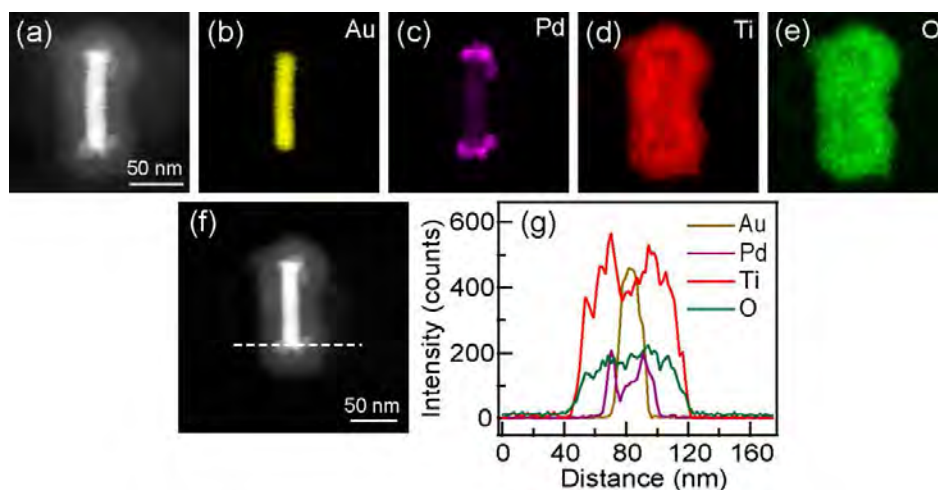
Figure 4.17 (Au nanorod core)/(discrete Pd shell)/(TiO$_2$ shell) nanostructures. (a) HAADF-STEM image of a single nanostructure. (b–e) Elemental maps of Au, Pd, Ti, and O on the nanostructure shown in (a), respectively. The scale bar in (a) also applies for (b–e). (f) HAADF-STEM image of a single nanostructure for elemental profiling. (g) Elemental profiles of Au, Pd, Ti, and O acquired along the dashed line shown in (f).
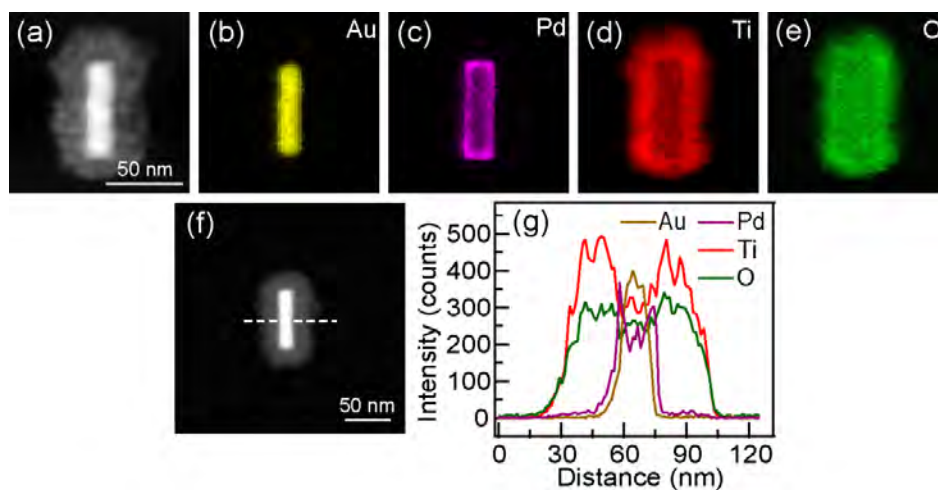
Figure 4.18 (Au nanorod core)/(continuous Pd shell)/(TiO$_2$ shell) nanostructures. (a) HAADF-STEM image of a single nanostructure. (b–e) Elemental maps of Au, Pd, Ti, and O on the nanostructure shown in (a), respectively. The scale bar in (a) also applies for (b–e). (f) HAADF-STEM image of a single nanostructure for elemental profiling. (g) Elemental profiles of Au, Pd, Ti, and O acquired along the dashed line shown in

(f).
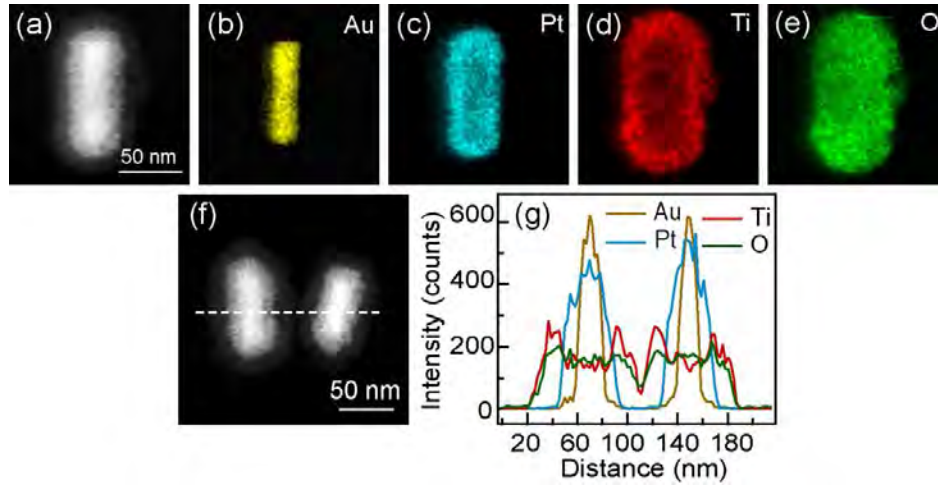
Figure 4.19 (Au nanorod core)/(Pt shell)/(TiO$_2$ shell) nanostructures. (a) HAADF-STEM image of a single nanostructure. (b–e) Elemental maps of Au, Pt, Ti, and O on the nanostructure shown in (a), respectively. The scale bar in (a) also applies for (b–e). (f) HAADF-STEM image of two nanostructures for elemental profiling. (g) Elemental profiles of Au, Pt, Ti, and O acquired along the dashed line shown in (f).

Figure 4.20 shows the extinction spectra of the nanostructures with the Pd, Pt, and Au nanorod-based bimetallic nanocrystals as the cores. The imaginary parts of the dielectric functions of Pd and Pt are much larger than that of Au. Therefore, the LSPR of monometallic Pd and Pt nanocrystals is strongly damped. In the visible-to-near-infrared region, the extinction spectra of the Pd and Pt nanocrystals only show a rising trend toward the short wavelength region (Figure 4.20a–c). When Pd and Pt are deposited on Au nanorods, the plasmon damping causes the LSPR of Au nanorods to be weakened and even disappear (Figure 4.20d–f). Comparison of the extinction spectra indicates that the overall extinction intensities of the core/shell nanostructure samples are generally higher than those of the corresponding uncoated metal nanocrystal samples (Figure 4.20). The increases in the extinction intensity are attributed to the increases in the overall particle size. In addition, the longitudinal plasmon resonance peaks of the (Au nanorod core)/(discrete Pd shell) and (Au

nanorod core)/(continuous Pd shell) nanocrystal samples are still observable at 955 nm and 750 nm, respectively, even though they are damped by the Pd shell. After TiO$_2$ coating, the longitudinal plasmon resonance peaks are red-shifted by 200 nm and 180 nm, respectively, owing to the large refractive index of the TiO$_2$ shell (Figure 4.20d and e).
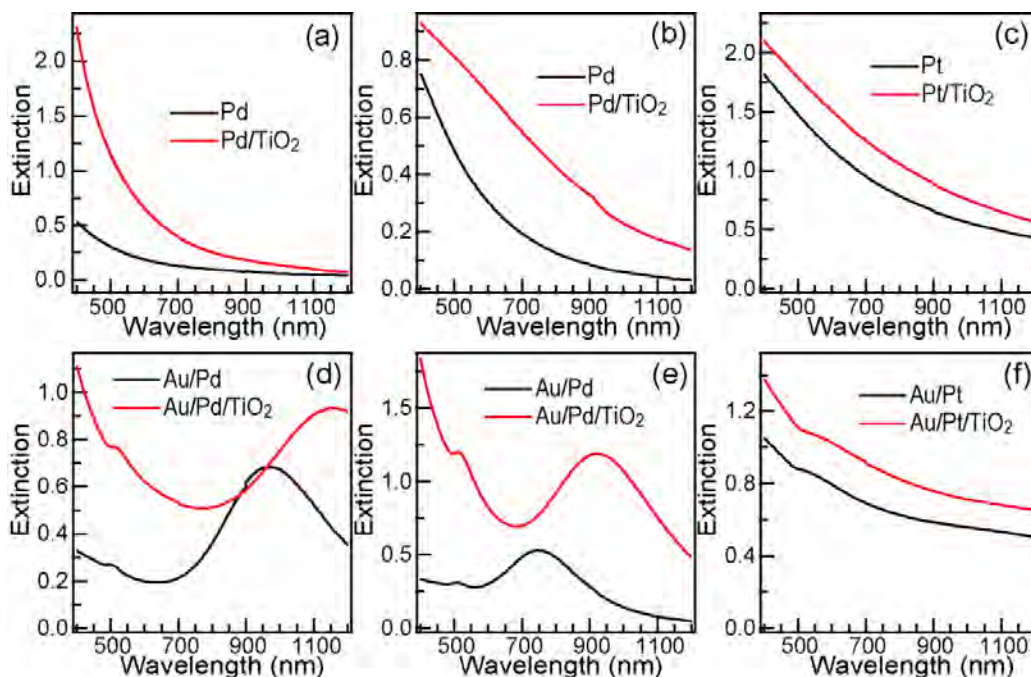
Figure 4.20 Extinction spectra of the uncoated monometallic and bimetallic nanocrystal samples and the corresponding core/shell nanostructure samples. (a) Porous Pd nanocrystals. (b) Cubic Pd nanocrystals. (c) Porous Pt nanocrystals. (d) (Au nanorod core)/(discrete Pd shell) nanocrystals. (e) (Au nanorod core)/(continuous Pd shell) nanocrystals. (f) (Au nanorod core)/(Pt shell) nanocrystals.

4.2 Applications of the (Au nanocrystal Core)/(TiO$_2$ Shell) Nanostructures

(Au nanocrystal core)/(TiO$_2$ shell) nanostructures, one of the most important plasmonic metal/semiconductor hybrids, offer a platform to integrate LSPR with

semiconductors. Their core/shell nanostructures even give more opportunity to enhance photon-harvesting applications, such as in solar cells and photocatalysis. Herein, I investigated the utilization of (Au nanocrystal core)/(TiO$_2$ shell) in DSSCs and ROS generation as proof-of-concept applications.

4.2.1 Plasmon-Enhanced Dye-Sensitized Solar Cells

Studies have shown that plasmonic metal nanocrystals can remarkably improve the power conversion efficiency (PCE) of DSSCs. In most previous investigations, surface-protected metal nanocrystals are mixed together with TiO$_2$ nanoparticles during the fabrication of photoanodes. Metal nanocrystals are present across the entire film electrode [42–44]. In such electrode structures, the intrinsic light absorption of metal nanocrystals always competes with the light harvesting of dye molecules. A high concentration of metal nanocrystals can block light transmission. As a result, light harvesting becomes progressively inefficient away from the front side of the anode. To minimize these negative effects, the particle concentration of plasmonic metal nanocrystals in the anode has to be very low, which restricts the plasmonic enhancement of light harvesting.

In this study, (Au nanorod core)/(TiO$_2$ shell) nanostructures were incorporated solely in the back side of the anode to overcome the limit, allowing for a high concentration of Au nanorods for efficient light scattering. Traditional and plasmonic DSSC photoanodes were involved in the fabrication process. The same nanostructure sample as shown in Figure 4.11b was employed to fabricate plasmonic DSSCs. First, the (Au nanorod core)/(TiO$_2$ shell) nanostructure paste was prepared according to a reported method with modifications [45]. Specifically, two types of ethyl cellulose powders, which are specified with viscosities of 9–11 cP and 45–55 cP in toluene (80 vol%)/isopropanol (20 vol%), respectively, were dissolved together beforehand in ethanol. The concentration of each type of ethyl cellulose was 5 wt%. The (Au nanorod core)/(TiO$_2$ shell) nanostructure sample (100 mg) was dispersed in ethanol

(10 mL) by ultrasonication for 1 h to ensure good dispersion. Anhydrous terpineol (350 mg) and the ethyl cellulose solution (500 mg) were added subsequently dropwise, followed by stirring and ultrasonication. The final mixture was kept in a water bath at 60 °C and under magnetic stirring until ethanol was completely evaporated to give a paste. The standard DSSC photoanode was composed of a 7-μm transparent layer and a 5-μm scattering layer [46]. The diameters of the TiO_2 nanoparticles in the two layers were ~20 nm (P25) and 100–200 nm, respectively. In the plasmonic DSSCs, the (Au nanorod core)/(TiO_2 shell) nanostructure paste was utilized as the scattering layer. The detailed procedure for the device fabrication is as follows. A transparent glass slide coated with fluorine-doped tin oxide (FTO) at 15 Ω/sq was cleaned by ultrasonication in ethanol, acetone, and water in sequence. The transparent layer was then printed onto the cleaned FTO slide with a doctor blade, followed by a thermal treatment at 120 °C for 10 min to solidify the layer. The scattering layer was subsequently applied at a controlled thickness, followed again by a thermal treatment at 120 °C for 10 min for solidification. The obtained electrode was thereafter thermally processed under air flow sequentially at 275 °C for 5 min, 325 °C for 5 min, 375 °C for 5 min, and 450 °C for 30 min to remove the organic molecules. After being cooled down to room temperature, the sintered electrode was soaked in an aqueous TiF_4 solution (0.02 M, containing 2.5 wt% $NH_3 \cdot H_2O$) for 120 min at 70 °C. The soaking allowed the pores in the scattering layer to be filled with TiO_2 to generate good connection between the TiO_2 nanoparticles. The film electrode was then rinsed with water and annealed again at 450 °C for 30 min. All of the temperature ramp rates during the fabrication of the DSSCs were 5 °C min^{-1}. After being cooled down to room temperature, the electrode was immersed in a solution of N719 dye (0.3 mM, in acetonitrile [50 vol%]/tert-butyl alcohol [50 vol%]) for 16 h to allow for maximal adsorption of the dye molecules. Non-adsorbed dye molecules were removed by rinsing with ethanol. The Pt counter-electrode was prepared by sputtering at 15 mA for 90 s at a power of 150 W. The photoanode and the Pt counter-electrode were assembled into a sandwich-type cell and sealed with a 60-μm hot-melt parafilm at 100

°C. An iodide-based liquid electrolyte (Dyesol, EL-HPE, 0.1 M LiI, 50 mM I_2, and 0.6 M 1,2-dimethy-l-3-propylimidazolium iodide in acetonitrile [85 vol%]/valeronitrile [15 vol%]) was subsequently introduced into the cell through a 0.75-mm-diameter hole that was predrilled on the back side of the Pt electrode. Finally, the hole was sealed with parafilm and covered with a glass slide at an elevated temperature. The effective areas of all the DSSCs were 0.24 cm^2.
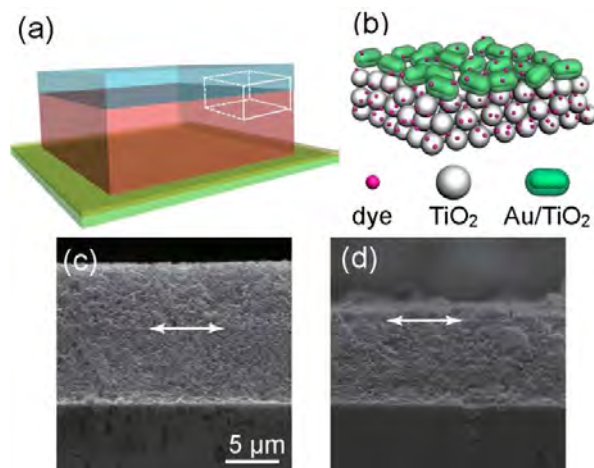
Figure 4.21 Characterization of the plasmonic and standard DSSCs. (a) Schematic of the photoanode, which contains a glass slide, FTO film, transparent layer, and scattering layer from bottom to top, respectively. (b) Schematic showing the zoomed-in part indicated with a box in (a). (c,d) SEM images of the cross sections of the photoanodes for a standard cell and a plasmonic cell, respectively. The white double-arrowed line indicates the interface between the transparent layer and the scattering layer.
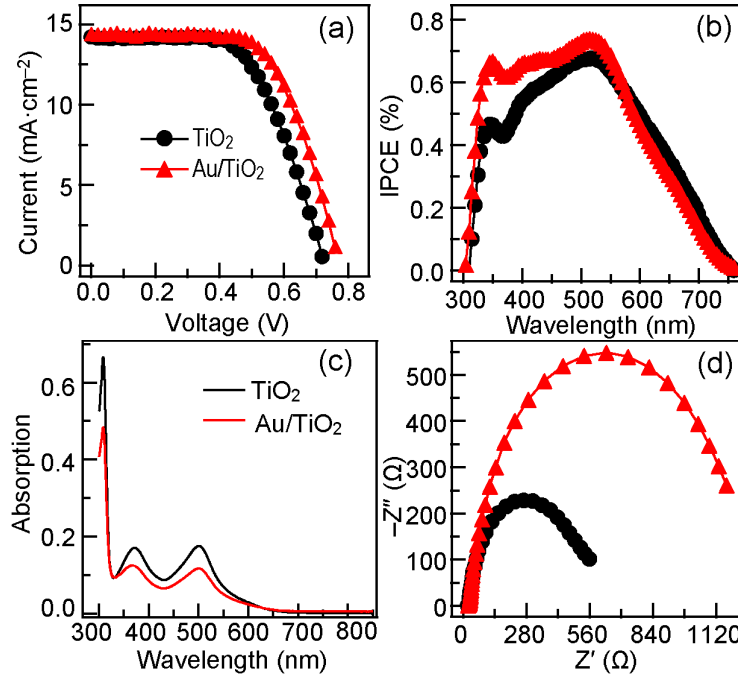
Figure 4.22 Performances of the plasmonic and standard DSSCs. The plasmonic photoanode is fabricated by incorporating the (Au nanorod core)/(TiO₂ shell) nanostructures. (a) Current–voltage curves. (b) IPCE spectra. (c) Absorption spectra of the dye molecules that were stripped from the photoanodes that contained the TiO₂ scattering layer and the (Au nanorod core)/(TiO₂ shell) nanostructure scattering layer. The adsorbed dye molecules were removed by immersing the photoanodes in an aqueous NaOH solution (0.1 M, 3 mL) for 24 h. (d) EIS spectra measured in dark.
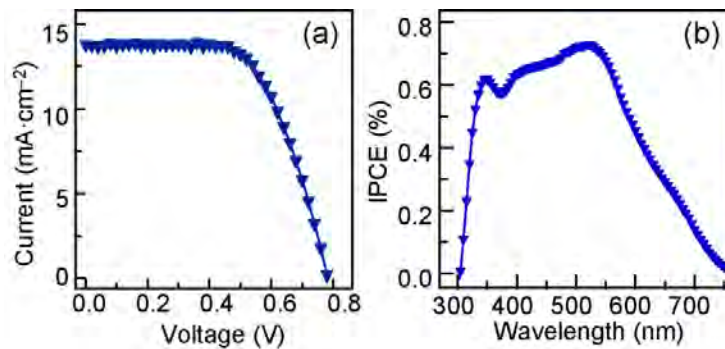
Figure 4.23 Performances of the plasmonic DSSCs that is fabricated by incorporating the (Au nanosphere core)/(TiO₂ shell) nanostructures. (a) Current–voltage curve. (b) IPCE spectrum.

Figure 4.21a and b display the schematic of the plasmonic photoanode. As observed on the SEM image of the cross section of the anode film (Figure 4.21c), the standard cell is composed of a ~7-μm transparent layer and a ~5-μm scattering layer. These thicknesses have been optimized for the solar cell performance. The plasmonic photoanode possesses a ~7-μm transparent layer and a ~1.3-μm scattering layer (Figure 4.21d). The performances of both the standard and plasmonic cells were examined. The standard cell exhibits a PCE of 6.22%, with a short-circuit current density (J_{sc}) of 14.23 mA cm^{-2}, an open-circuit voltage (V_{oc}) of 0.727 V, and a fill factor (FF) of 0.601 (Figure 4.22a). In comparison, the corresponding performance parameters for the plasmonic cell are 7.05%, 14.26 mA cm^{-2}, 0.771 V, and 0.641. Therefore, with the plasmonic scattering layer at a thickness ~1/4 that of the standard scattering layer, a remarkable improvement of 13.3% in the PCE is obtained. The PCE improvement is ascribed to the following two mechanisms. First, the introduction of the core/shell nanostructures increases the optical path in the cell. Au nanorods possess very high scattering cross-sections. The incident light is scattered by the nanostructures and trapped in the cell, leading to an increase in the optical path [6]. Therefore, a thin nanostructure layer can outperform the TiO$_2$ nanoparticle layer for scattering light back to the absorber layer. This is confirmed by the incident photon-to-electron conversion efficiency (IPCE) spectra (Figure 4.22b). Although the amount of the loaded dye in the plasmonic cell is considerably smaller than that in the standard cell (Figure 4.23c), the photocurrent generation of the former is still higher than that of the latter. The larger optical path of the plasmonic anode enables more efficient usage of light energy and allows for an improved photocurrent generation efficiency. Second, the plasmonic cell with a thinner anode reduces the recombination probability of electrons. Owing to the reduced film thickness, the path length of electron transport is also shortened. The fast electron transport to the collecting electrode suppresses the back reaction between electrons in the conduction band and I$_3^-$ ions in the electrolyte [47]. The suppression of the back reaction is evidenced by the electrochemical impedance spectroscopy (EIS) characterization. Figure 4.22d

displays the EIS spectra acquired in dark. The Nyquist arc on the EIS spectrum reflects the back transfer of electrons from the conduction band of TiO_2 to I_3^- ions in the electrolyte [48]. Apparently, the diameter of the Nyquist arc for the plasmonic cell is much larger than that of the standard one. The calculated recombination resistances are 1550 Ω and 548 Ω, respectively, for the plasmonic and standard cells. This result indicates clearly that the recombination kinetics in the plasmonic cell is substantially retarded. The improved DSSC performance was also verified by employing the (Au nanosphere core)/(TiO_2 shell) nanostructures as the scattering layer (Figure 4.23). The PCE is 6.80%, an increase of 9.3% in comparison with that of the standard cell. The J_{sc}, V_{oc}, and FF values are 13.76 mA cm^{-2}, 0.781 V, and 0.633, respectively.

4.2.2 Plasmon-Enhanced Reactive Oxygen Species Generation

Photodynamic therapy (PDT) is a promising, minimally invasive cancer treatment method. It needs three key components: light, oxygen, and a photosensitizer. Under light illumination at a proper wavelength, the photosensitizer is excited and subsequently transfers energy to oxygen in the surrounding environment, generating ROS mainly in the form of free radicals and singlet oxygen. The generated ROS can oxidatively kill cells through apoptosis, necrosis, or autophagy [49]. Photo-excitation of TiO_2 nanoparticles with UV light has been shown to produce ROS, including hydrogen peroxide, superoxide, $^1O_2$, and $\cdot$OH [50]. However, the poor penetration of UV light in biological tissues hampers the effective therapeutic effects of TiO_2 nanoparticles. In this regard, great efforts have been made to develop organic photosensitizers that can efficiently absorb visible or near-infrared light in coincidence with the biological window [51,52]. The LSPR wavelength of our (Au nanorod core)/(TiO_2 shell) nanostructures can be tailored in the range from 700 nm to over 1000 nm. To explore if our nanostructures can function as photosensitizers for PDT, we investigated if they can generate $^1O_2$ and $\cdot$OH under light illumination around their plasmon wavelength.
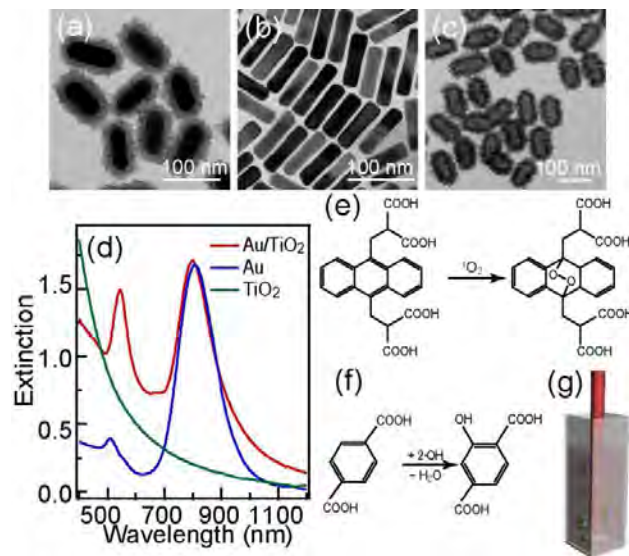
Figure 4.24 ROS generation examination using (Au nanorod core)/(TiO$_2$ shell) nanostructures as photosensitizers. (a–c) TEM images of the core/shell nanostructure sample, the Au nanorod sample, and the hollow TiO$_2$ nanostructures, respectively. The measured sizes of the core/shell nanostructures in (a) are: core length, 89 ± 10 nm; core diameter, 34 ± 3 nm; shell thickness, 18 ± 3 nm. The sizes of the Au nanorods in (b) are: length, 83 ± 6 nm; diameter, 22 ± 2 nm. The hollow TiO$_2$ nanostructure sample in (c) is made from the core/shell nanostructure sample in (a). (d) Extinction spectra of the three samples as mentioned in (a–c). (e) Reaction between ABDA and ^{1}O$_2$. (f) Reaction between TA and ·OH. (g) Schematic of the setup for the ROS generation.

In my experiments, a semiconductor diode laser at 809 nm was used as the light source. A (gold nanorod core)/(TiO$_2$ shell) nanostructure sample (Figure 4.24a) with the longitudinal plasmon wavelength at 806 nm was examined. For comparison, a gold nanorod sample with the longitudinal plasmon wavelength at 809 nm and a hollow TiO$_2$ nanostructure sample were also tested (Figure 4.24b–d). The generation of ^{1}O$_2$ was monitored using 9,10-anthracenediyl-bis(methylene) dimalonic acid (ABDA) as a probe. ABDA reacts irreversibly with ^{1}O$_2$ to yield an endoperoxide (Figure 4.24e), causing a reduction in the absorption peak intensity [53,54]. The formation of ·OH was detected with terephthalic acid (TA). TA has been widely used

in photocatalysis for detecting ·OH. It can react with ·OH to generate a fluorescent product emitting around 425 nm (Figure 4.24f) [55,56]. The spectral changes of ABDA and TA were monitored, respectively. Typically, an as-prepared (Au nanorod core)/(TiO$_2$ shell) nanostructure solution (10 mL) was precipitated by centrifugation and redispersed in the dye solution in a cuvette with 1-cm path length. To avoid the heating of the solution by the photothermal effect, the cuvette was placed in a water bath kept at room temperature. The illumination laser beam was introduced vertically from the top surface into the solution (Figure 4.24g). The optical power density from the laser was measured to be 8.5 W cm^{-2}. For detecting $^1O_2$, ABDA (4.2 mL, 0.12 mM) was employed. The particle concentration of the nanostructure sample is estimated to be ~0.47 nM. To eliminate the adsorption effect of ABDA on the nanostructures, the mixture solution was first kept under stirring in dark for 4–6 h to reach adsorption equilibrium. Under the laser illumination, at every 20 min, 0.6 mL of the mixture solution was taken out and subjected to centrifugation. The absorption spectrum of the supernatant was then measured. For detecting ·OH, TA (2 mL, 10 mM, pH = 7–8, adjusted using a NaOH solution) was utilized. The particle concentration of the nanostructure sample is estimated to be ~0.98 nM. After the laser illumination for 2 h, the mixture solution was centrifuged to remove the nanostructures. The fluorescence emission spectrum of the generated 2-hydroxy terephthalic acid in the supernatant was subsequently measured under the excitation wavelength of 315 nm.
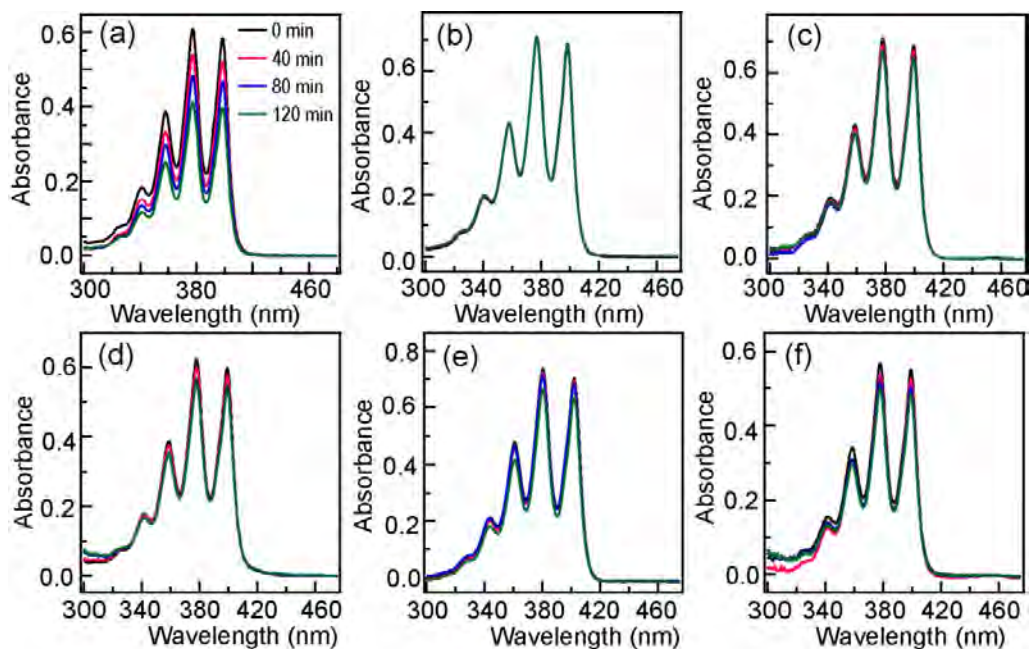
Figure 4.25 Time-dependent absorption spectra of ABDA measured in different control experiments. (a) ABDA together with the (Au nanorod core)/(TiO$_2$ shell) nanostructures under the 809-nm laser illumination. (b) ABDA only, without light illumination. (c) ABDA only, under the laser illumination. (d) ABDA together with the (Au nanorod core)/(TiO$_2$ shell) nanostructure sample, without light illumination. (e) ABDA together with the uncoated Au nanorod sample, under the laser illumination. (f) ABDA together with the hollow TiO$_2$ nanostructure sample, under the laser illumination.

When ABDA was present in the (Au nanorod core)/(TiO$_2$ shell) nanostructure solution, a distinct reduction in the absorption of ABDA was observed when the solution had been exposed to the laser illumination for 2 h (Figure 4.25a). The decrease in the absorption indicates the generation of $^1O_2$. To see clearly the $^1O_2$ generation behavior, we plotted the absorption decrease of the strongest peak at 377 nm as a function of the illumination time in Figure 4.26a, where the decrease has been normalized against the value right before the laser illumination. The absorption shows a rapid decrease and drops to ~57% after illumination for 2 h, revealing that the generated amount of $^1O_2$ increases with the illumination time. To further verify the

$^1O_2$ generation capability of the core/shell nanostructures, five control experiments were performed, where the sole dye, the uncoated Au nanorod sample, the hollow TiO$_2$ nanostructure sample, and the core/shell nanostructure sample were examined either with or without the laser illumination (Figure 4.25b–f and Figure 4.26a). After 2 h of illumination, the absorption of ABDA only decreases slightly to ~90% of its starting value for both the uncoated Au nanorod and hollow TiO$_2$ nanostructure samples. The slight decrease in the absorption is probably caused by the generation of a small amount of $^1O_2$ and/or the photobleaching of ABDA under the laser illumination.
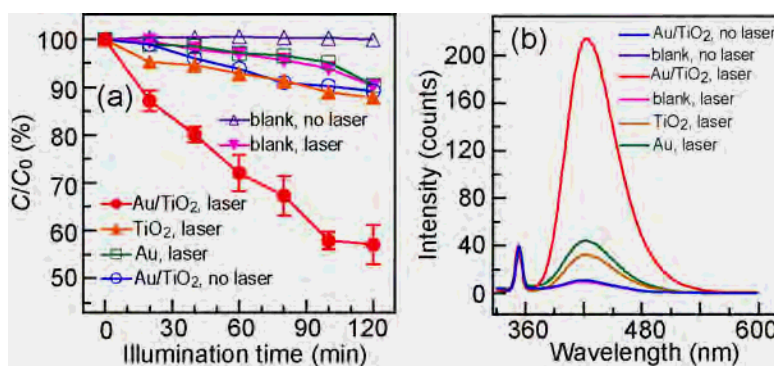
Figure 4.26 Performances of ROS generation. (a) Normalized reductions in the absorption of ABDA at 377 nm as functions of the illumination time. (b) Fluorescence spectra of the different sample solutions containing TA.

When TA was used as the probe for ·OH, very weak fluorescence was detected for the uncoated Au nanorod and hollow TiO$_2$ nanostructure samples after 2 h of illumination (Figure 4.26b). In contrast, a more than 5-times stronger fluorescence emission was measured for the (Au nanorod core)/(TiO$_2$ shell) nanostructure sample. These results indicate that the core/shell nanostructures can effectively produce ·OH upon plasmon excitation.

Our measurements clearly show that the (Au nanorod core)/(TiO$_2$ shell) nanostructures can effectively generate both $^1O_2$ and ·OH under resonant excitation. The ROS production efficiency of organic photosensitizers has been known to be

dependent on the efficacy and amount of the photosensitizer, the wavelength and intensity of the laser, and the environment temperature [57]. In our study, the laser source and the environment temperature are fixed. The fact that the hollow TiO_2 nanostructures only generate a very small amount of ROS suggests that LSPR plays a key role in the ROS generation by the (Au nanorod core)/(TiO_2 shell) nanostructures. LSPR in this work functions through a so-called plasmonic sensitization mechanism that is described in Chapter 1 (*Section 1.2.1*), where a metal nanocrystal absorbs light through its LSPR excitation, produce hot electrons, and inject hot electrons into the conduction band of a semiconductor in contact with the metal nanocrystal [5]. In the (Au nanorod core)/(TiO_2 shell) nanostructure, the Au nanorod is in contact with the TiO_2 shell. A Schottky barrier is formed at the interface between the two materials. Under resonant plasmon excitation, a population of electron–hole pairs is generated. The fraction of excited electrons that have energies higher than the Schottky barrier can inject into the conduction band of TiO_2. The injected electrons react with oxygen molecules in the surrounding environment to yield superoxide anion radicals ($O_2^{\bullet-}$), which will either react with holes in the Au nanorod to give $^1O_2$ or react with water to produce ·OH.

4.3 Summary

In this chapter, I demonstrated a facile and robust method for coating TiO_2 onto noble metal nanocrystals. The tested noble metal nanocrystals include monometallic Au, Pd, Pt and (Au nanorod)-based bimetallic nanocrystals with different sizes and shapes. The core/shell nanostructures are obtained by first surface-modifying the pre-grown metal nanocrystals and using $TiCl_3$ as the TiO_2 precursor. The morphology of the metal nanocrystal core is preserved after TiO_2 shell coating. In particular, Au nanocrystals exhibit strong size-, shape-, and environment-dependent LSPR. By changing the size, shape of the Au nanocrystal core and/or the thicknesses of the TiO_2 shell, the plasmon band of the produced core/shell nanostructure can be tailored over

a broad spectral range. Furthermore, we have also examined the plasmonic effects of (Au nanorod core)/(TiO$_2$ shell) nanostructures in improving DSSC performance and generating ROS under near-infrared light. When the core/shell nanostructures are utilized as the scattering layer in DSSCs, a 13% higher PCE is obtained even though the thickness of the plasmonic scattering layer is about one fourth of that of the standard TiO$_2$ scattering layer. When the core/shell nanostructures are examined as photosensitizers, they are found to exhibit a remarkable capability to generate ROS under near-infrared excitation. Taken together, our results show unambiguously that the (Au nanocrystal core)/(TiO$_2$ shell) nanostructures can serve as a multifunctional platform for light harvesting applications in photovoltaics, photocatalysis, and nanomedicine. This facile and versatile synthetic approach provides an attractive way for coating TiO$_2$, a metal oxide semiconductor of wide interests in photocatalysis and solar energy harvesting, onto a variety of noble metal nanocrystals to achieve integrated as well as synergistic functionalities.

References

[1] Roy, P.; Berger, S.; Schmuki, P. *Angew. Chem. Int. Ed.* **2011**, *50*, 2904–2939.

[2] Kumar, S. G.; Devi, L. G. *J. Phys. Chem. A* **2011**, *115*, 13211–13241.

[3] Linic, S.; Christopher, P.; Ingram, D. B. *Nat. Mater.* **2011**, *10*, 911–921.

[4] Ming, T.; Chen, H. J.; Jiang, R. B.; Li, Q.; Wang, J. F. *J. Phys. Chem. Lett.* **2012**, *3*, 191–202.

[5] Xiao, M. D.; Jiang, R. B.; Wang, F.; Fang, C. H.; Wang, J. F.; Yu, J. C. *J. Mater. Chem. A* **2013**, *1*, 5790–5805.

[6] Atwater, H. A.; Polman, A. *Nat. Mater.* **2010**, *9*, 205–213.

[7] Feng, X. J.; Sloppy, J. D.; LaTempa, T. J.; Paulose, M.; Komarneni, S.; Bao, N. Z.; Grimes, C. A. *J. Mater. Chem.* **2011**, *21*, 13429–13433.

[8] Brown, M. D.; Suteewong, T.; Kumar, R. S. S.; D'Innocenzo, V.; Petrozza, A.; Lee, M. M.; Wiesner, U.; Snaith, H. J. *Nano Lett.* **2011**, *11*, 438–445

[9] Tsukamoto, D.; Shiraishi, Y.; Sugano, Y.; Ichikawa, S.; Tanaka, S.; Hirai, T. *J. Am. Chem. Soc.* **2012**, *134*, 6309–6315.

[10] Camellone, M. F.; Zhao, J. L.; Jin, L. Y.; Wang, Y. M.; Muhler, M.; Marx, D. *Angew. Chem. Int. Ed.* **2013**, *52*, 5780–5784.

[11] Green, I. X.; Tang, W. J.; Neurock, M.; Yates Jr, J. T. *Science* **2011**, *333*, 736–739.

[12] Pastoriza-Santos, I.; Pérez-Juste, J.; Liz-Marzán, L. M. *Chem. Mater.* **2006**, *18*, 2465–2467.

[13] Gorelikov, I.; Matsuura, N. *Nano Lett.* **2008**, *8*, 369–373.

[14] Fernández-López, C.; Mateo-Mateo, C.; Álvarez-Puebla, R. A.; Pérez-Juste, J.; Pastoriza-Santos, I.; Liz-Marzán, L. M. *Langmuir* **2009**, *25*, 13894–13899.

[15] Guerrero-Martínez, A.; Pérez-Juste, J.; Liz-Marzán, L. M. *Adv. Mater.* **2010**, *22*, 1182–1195.

[16] Sun, H.; He, J. T.; Wang, J. Y.; Zhang, S.-Y.; Liu, C. C.; Sritharan, T.; Mhaisalkar, S.; Han, M.-Y.; Wang, D.; Chen, H. Y. *J. Am. Chem. Soc.* **2013**, *135*, 9099–9110.

[17] Seh, Z. W.; Liu, S. H.; Zhang, S.-Y.; Shah, K. W.; Han, M.-Y. *Chem. Commun.* **2011**, *47*, 6689–6691.

[18] Liu, W.-L.; Lin, F.-C.; Yang, Y.-C.; Huang, C.-H.; Gwo, S.; Huang, M. H.; Huang, J.-S. *Nanoscale* **2013**, *5*, 7953–7962.

[19] Lee, I.; Joo, J. B.; Yin, Y. D.; Zaera, F. *Angew. Chem. Int. Ed.* **2011**, *50*, 10208–10211.

[20] Zhang, Q.; Lima, D. Q.; Lee, I.; Zaera, F.; Chi, M. F.; Yin, Y. D. *Angew. Chem. Int. Ed.* **2011**, *50*, 7088–7092.

[21] Chen, H. J.; Shao, L.; Li, Q.; Wang, J. F. *Chem. Soc. Rev.* **2013**, *42*, 2679–2724.

[22] Liu, L. Q.; Ouyang, S. X.; Ye, J. H. *Angew. Chem. Int. Ed.* **2013**, *52*, 6689–6693.

[23] Pu, Y.-C; Wang, G. M.; Chang, K.-D.; Ling, Y.-C.; Lin, Y.-K.; Fitzmorris, B. C.; Liu, C.-M.; Lu, X. H.; Tong, Y. X.; Zhang, J. Z.; Hsu, Y.-J.; Li, Y. *Nano Lett.* **2013**, *13*, 3817–3823.

[24] Seh, Z. W.; Liu, S. H.; Zhang, S.-Y.; Bharathi, M. S.; Ramanarayan, H.; Low, M.; Shah, K. W.; Zhang, Y.-W.; Han, M.-Y. *Angew. Chem. Int. Ed.* **2011**, *50*, 10140–10143.

[25] Ni, W. H.; Yang, Z.; Chen, H. J.; Li, L.; Wang, J. F. *J. Am. Chem. Soc.* **2008**, *130*, 6692–6693.

[26] Guo, W. X.; Xu, C.; Wang, X.; Wang, S. H.; Pan, C. F.; Lin, C. J.; Wang, Z. L. *J. Am. Chem. Soc.* **2012**, *134*, 4437–4441.

[27] Hosono, E.; Fujihara, S.; Kakiuchi, K.; Imai, H. *J. Am. Chem. Soc.* **2004**, *126*, 7790–7791.

[28] Liu, R.; Sen, A. *J. Am. Chem. Soc.* **2012**, *134*, 17505–17512.

[29] Xiao, M. D.; Zhao, C. M.; Chen, H. J.; Yang, B. C.; Wang, J. F. *Adv. Funct. Mater.* **2012**, *22*, 4526–4532.

[30] Chen, H. J.; Shao, L.; Man, Y. C.; Zhao, C. M.; Wang, J. F.; Yang, B. C. *Small* **2012**, *8*, 1503–1509.

[31] Zhao, X. W.; Jin, W. Z.; Cai, J. G.; Ye, J. F.; Li, Z. H.; Ma, Y. R.; Xie, J. L.; Qi, L. M. *Adv. Funct. Mater.* **2011**, *21*, 3554–3563.

[32] Zhao, X. W.; Jin, W. Z.; Cai, J. G.; Ye, J. F.; Li, Z. H.; Ma, Y. R.; Xie, J. L.; Qi, L. M. *Adv. Funct. Mater.* **2011**, *21*, 3554–3563.

[33] Ye, M. D.; Gong, J. J.; Lai, Y. K.; Lin, C. J.; Lin, Z. Q. *J. Am. Chem. Soc.* **2012**, *134*, 15720–15723.

[34] Huang, H. B.; Leung, D. Y. C.; Ye, D. Q. *J. Mater. Chem.* **2011**, *21*, 9647–9652.

[35] Deshlahra, P.; Schneider, W. F.; Bernstein, G. H.; Wolf, E. E. *J. Am. Chem. Soc.* **2011**, *133*, 16459–16467.

[36] Wu, X.-F.; Chen, Y.-F.; Yoon, J.-M.; Yu, Y.-T. *Mater. Lett.* **2010**, *64*, 2208–2210.

[37] Wang, F.; Li, C. H.; Chen, H. J.; Jiang, R. B.; Sun, L.-D.; Li, Q.; Wang, J. F.; Yu, J. C.; Yan, C.-H. *J. Am. Chem. Soc.* **2013**, *135*, 5588–5601.

[38] Zhang, G.-R.; Zhao, D.; Feng, Y.-Y.; Zhang, B. S.; Su, D. S.; Liu, G.; Xu, B.-Q. *ACS Nano* **2012**, *6*, 2226–2236

[39] Su, R.; Tiruvalam, R.; He, Q.; Dimitratos, N.; Kesavan, L.; Hammond, C.; Lopez-Sanchez, J. A.; Bechstein, R.; Kiely, C. J.; Hutchings, G. J.; Besenbacher, F. *ACS Nano* **2012**, *6*, 6284–6292.

[40] Enache, D. I.; Edwards, J. K.; Landon, P.; Solsona-Espriu, B.; Carley, A. F.; Herzing, A. A.; Watanabe, M.; Kiely, C. J.; Knight, D. W.; Hutchings, G. J. *Science* **2006**, *311*, 362–365.

[41] Jin, Z.; Wang, F.; Wang, F.; Wang, J. X.; Yu, J. C.; Wang, J. F. *Adv. Funct. Mater.* **2013**, *23*, 2137–2144.

[42] Zhang, W.; Saliba, M.; Stranks, S. D.; Sun, Y.; Shi, X.; Wiesner, U.; Snaith, H. J. *Nano Lett.* **2013**, *13*, 4505–4510.

[43] Qi, J. F.; Dang, X. N.; Hammond, P. T.; Belcher, A. M. *ACS Nano* **2011**, *5*, 7108–7116.

[44] Dang, X. N.; Qi, J. F.; Klug, M. T.; Chen, P.-Y.; Yun, D. S.; Fang, N. X.; Hammond, P. T.; Belcher, A. M. *Nano Lett.* **2013**, *13*, 637–642.

[45] Ito, S.; Chen, P.; Comte, P.; Nazeeruddin, M. K.; Liska, P.; Péchy, P.; Grätzel, M. *Prog. Photovolt: Res. Appl.* **2007**, *15*, 603–612.

[46] Ito, S.; Murakami, T. N.; Comte, P.; Liska, P.; Grätzel, C.; Nazeeruddin, M. K.;

Grätzel, M. *Thin Solid Films* **2008**, *516*, 4613–4619.

[47] Frank, A. J.; Kopidakis, N.; van de Lagemaat, J. *Coord. Chem. Rev.* **2004**, *248*, 1165–1179.

[48] Chang, S.; Wang, H. D.; Hua, Y.; Li, Q.; Xiao, X. D.; Wong, W.-K.; Wong, W. Y.; Zhu, X. J.; Chen, T. *J. Mater. Chem. A.* **2013**, *1*, 11553–11558.

[49] Chatterjee, D. K.; Fong, L. S.; Zhang, Y. *Adv. Drug Delivery Rev.* **2008**, *60*, 1627–1637.

[50] Dimitrijevic, N. M.; Rozhkova, E.; Rajh, T. *J. Am. Chem. Soc.* **2009**, *131*, 2893–2899.

[51] Kuo, W.-S.; Chang, C.-N.; Chang, Y.-T.; Yang, M.-H.; Chien, Y.-H.; Chen, S.-J.; Yeh, C.-S. *Angew. Chem., Int. Ed.* **2010**, *49*, 2711–2715.

[52] Idris, N. M.; Gnanasammandhan, M. K.; Zhang, J.; Ho, P. C.; Mahendran, R.; Zhang, Y. *Nat. Medicine* **2012**, *18*, 1580–1586.

[53] Jensen, R. L.; Arnbjerg, J.; Ogilby, P. R. *J. Am. Chem. Soc.* **2012**, *134*, 9820–9826.

[54] Zhao, T. T.; Shen, X. Q.; Li, L.; Guan, Z. P.; Gao, N. Y.; Yuan, P. Y.; Yao, S. Q.; Xu, Q.-H.; Xu, G. Q. *Nanoscale* **2012**, *4*, 7712–7719.

[55] Yang, W. L.; Zhang, L.; Hu, Y.; Zhong, Y. J.; Wu, H. B.; Lou, X. W. *Angew. Chem. Int. Ed.* **2012**, *51*, 11501–11594.

[56] Yang, H. G.; Liu, G.; Qiao, S. Z.; Sun, C. H.; Jin, Y. G.; Smith, S. C.; Zou, J.; Cheng, H. M.; Lu, G. Q. *J. Am. Chem. Soc.* **2009**, *131*, 4078–4083.

[57] Fales, A. M.; Yuan, H.; Vo-Dinh, T. *Langmuir* **2011**, *27*, 12186–12190.

Chapter 5

Tunable Fano Resonance in (Au Nanorod Core)/(TiO$_2$ Shell) Nanostructures

Fano resonance is a relatively old topic that has been extensively investigated in atomic and condensed matter physics. It is named after Ugo Fano, who experimentally discovered the distinctly asymmetric absorption spectra of metal gases and studied it theoretically [1,2]. He ascribed the asymmetric spectra to the constructive and destructive interference between the discrete and broad continuous states with overlapping energies. Subsequent to this discovery, Fano resonance has been observed and investigated in several optical systems, such as photonic crystals, metamaterials, and plasmonic systems [3–8]. Among them, Fano resonance in plasmonic nanostructures is of particular interest [9,10]. Efficient excitation and interference of different plasmon modes can generate pronounced Fano resonance [11]. Since plasmonic Fano resonance comes from the interference between broad and narrow resonance modes with spectral overlap [2], it possesses an inherent sensitivity to the surrounding environment as well as the geometry. Small perturbations can lead to dramatic spectral shifts. Plasmonic Fano resonance has been demonstrated to be more sensitive to the refractive index of the surrounding medium than the primitive plasmon modes in an individual metal nanocrystal [12–14]. They therefore show great potential in applications of ultrasensitive chemical and biological sensing. For example, introduction of a layer of molecules in the intermediate environment can induce a significantly spectral shift in the resonant peak [15]. The single-molecule detection limit can be approached in the presence of Fano resonance [10].

Many works have revealed that symmetry breaking in plasmonic metal nanostructures is the most efficient way to inducing Fano resonance. Symmetry breaking in plasmonic systems provides a nonuniform electromagnetic environment

near the nanostructures, which will enable the effective interference of various plasmon modes [16]. A variety of plasmonic nanostructures have been designed for realizing symmetry breaking. For example, heterodimers that are composed of two adjacent plasmonic nanocrystals with different shapes, sizes, or compositions are an effective configuration [17–19]. Symmetry breaking can be achieved in Au nanosphere-involved multilayer nanoshell or eccentric nanostructures, where the central particle is displaced with respect to the center of the surrounding shell [11,20,21]. Fano resonance can also be generated by introducing an anisotropic environment, such as placing a plasmonic nanocrystal on a dielectric substrate [22]. Although Fano resonance can be generated and tuned using such strategies, the fabrication of such architectures often involves expensive techniques or rigorous conditions, making them difficult for practical applications. In this context, plasmonic nanostructures that possess Fano resonance and can be simply prepared are highly desired. Pal *et al*. have demonstrated in simulations that (Au core)/(Ag shell) nanostructures are a good candidate as a Fano generator [23]. However, a uniform shell thickness below 5 nm is required, which is still a great challenge in preparation. Experiments have shown that coating Au nanospheres with sulfide can induce Fano resonance in the scattering spectrum [16]. The broad and strong scattering background of the sulfide shell couples efficiently with the narrow plasmon resonance of the Au core, leading to a distinct Fano resonance. The Fano resonance is highly dependent on the gap distance between the core and shell (Figure 5.1). As shown in Figure 5.1d, the feature of an asymmetric line shape on the scattering spectra is a signature of Fano resonance. In addition, the Fano resonance peak gradually blue shifts with decreasing intensities as the gap distance is increased. The increasing gap distance weakens the coupling interaction between the core and shell, resulting in the blue shift and intensity decrease in the scattering spectrum.
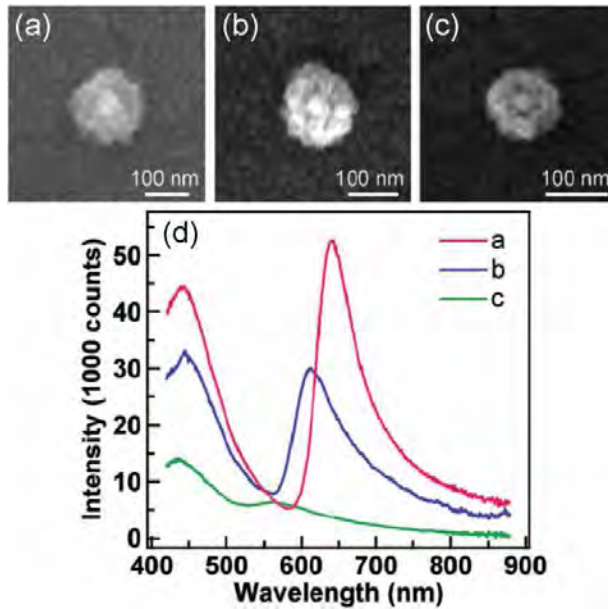
Figure 5.1 Fano resonance in (Au nanosphere core)/(ZnS shell) nanostructures [16]. (a–c) SEM images of an individual (Au nanosphere core)/(ZnS shell) nanostructure with the gap distance of 0 nm, 1 nm, and 5 nm, respectively. (d) Representative scattering spectra for the nanostructure samples.

In this chapter, I will introduce the realization of tunable Fano resonance in (Au nanorod core)/(TiO$_2$ shell) nanostructures. The core/shell nanostructures can be easily prepared by a simple method that has been described in Chapter 4. TiO$_2$ shell with a large refractive index provides a broad and strong scattering background. Moreover, the Au nanorod core supports a transverse plasmon mode at around 530 nm and a synthetically tunable longitudinal plasmon mode covering the visible and near-infrared region [24]. The coupling between the core and shell is therefore expected to simultaneously occur in both transverse and longitudinal modes. Furthermore, I think that the Fano resonance arising from the interference between the shell and the longitudinal plasmon mode of the core can be tailored.

5.1 Effect of the Plasmon Energy of the Au Nanorod Core

Au nanocrystals stabilized with cetyltrimethylammonium bromide were

synthesized by employing the seed-mediated method together with oxidation shortening [25–27] (see the detailed process in Chapter 2). The (Au nanocrystal core)/(TiO$_2$ shell) nanostructures were prepared using the "seeded growth" method that has been described in detail in Chapter 4. The as-grown (Au nanocrystal core)/(TiO$_2$ shell) nanostructures were immobilized onto indium tin oxide (ITO)-coated glass substrates for optical characterization. A pattern-matching method was used to correlate the same nanostructure under scanning electron microscopy (SEM) imaging and its scattering spectrum obtained on our dark-field optical system [28]. For each (Au nanocrystal core)/(TiO$_2$ shell) nanostructure sample, the scattering spectra of at least 25 nanoparticles were acquired. The shown spectra are the most typical ones.
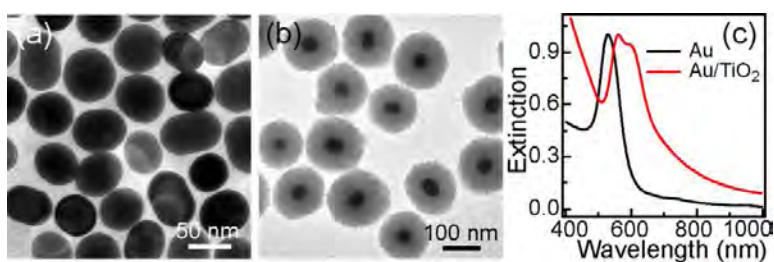
Figure 5.2 TEM images of the Au nanospheres (a), (Au nanosphere core)/(TiO$_2$ shell) nanostructures (b), and the corresponding extinction spectra (c), respectively.
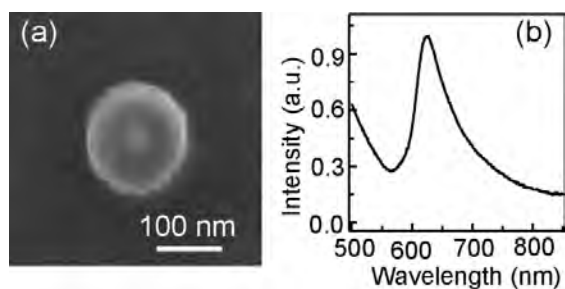
Figure 5.3 SEM image of an individual (Au nanosphere core)/(TiO$_2$ shell) nanostructure (a) and the corresponding scattering spectrum (b). The scattering spectrum was normalized against the peak intensity.

Fano resonance was first examined in (Au nanosphere core)/(TiO$_2$ shell)

nanostructures. The diameter of the Au nanosphere sample was determined to be 41.9 ± 3.0 nm from transmission electron microscopy (TEM) images (Figure 5.2a). TiO_2 is grown on the Au nanospheres with a uniform thickness of 49.2 ± 2.9 nm (Figure 5.2b). Owing to the higher refractive index of TiO_2 than that of water, the plasmon resonance red-shifts from 528 nm to 561 nm after the formation of the core/shell nanostructures (Figure 5.2c). A small peak at 598 nm is present on the extinction spectrum. It is caused by the impurity of the Au nanosphere sample, which can also be verified in the TEM images of the uncoated Au nanocrystals. Figure 5.3 displays the representative scattering spectrum of a single (Au nanosphere core)/(TiO_2 shell) nanostructure. The plasmon peak is red-shifted to 627 nm. The red shift is caused by the interaction between the nanostructure and the ITO substrate [28–30]. Moreover, the scattering peak exhibits an asymmetric line shape. Previous results in our group have proved that ITO substrates only cause a red shift on the resonance peak. It does not modify the plasmonic spectral shape of supported Au nanocrystals [16]. Therefore, the distinct asymmetric spectral profile is caused by Fano resonance originated from the interference between the core and shell.
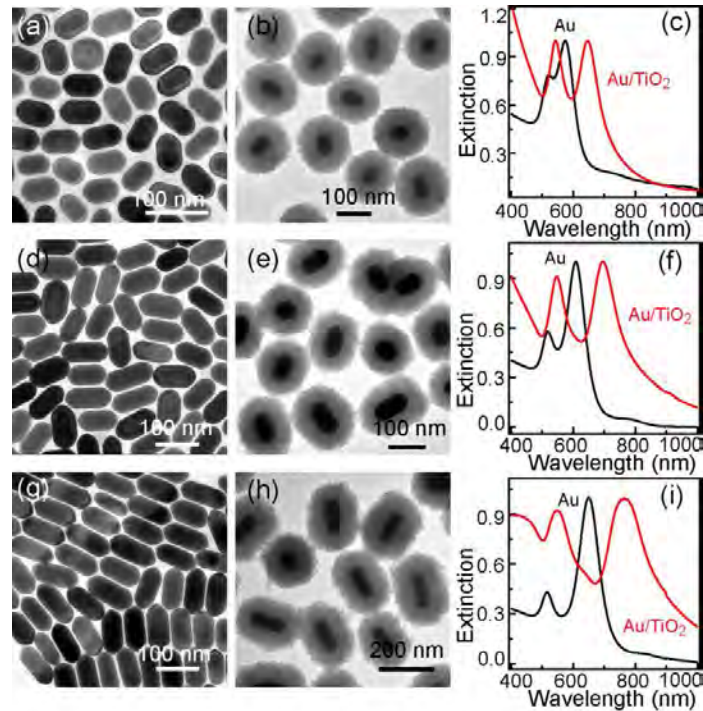
Figure 5.4 TEM images and extinction spectra of the Au nanorods and (Au nanorod core)/(TiO$_2$ shell) nanostructures. The bare Au nanorods possess a longitudinal plasmon wavelength of 574 nm (a–c), 608 nm (d–f), and 650 nm (g–i), respectively. The extinction spectra were normalized against the peak intensity of the longitudinal plasmon mode.

Three Au nanorod samples with longitudinal plasmon wavelengths of 574 nm, 608 nm, and 650 nm were chosen to investigate the Fano resonance in (Au nanorod core)/(TiO$_2$ shell) nanostructure samples. The core sizes were measured to be $(57.6 \pm 2.1) \times (37.8 \pm 1.3)$ nm, $(80.6 \pm 6.1) \times (40.4 \pm 2.8)$ nm, and $(88.2 \pm 7.9) \times (41.2 \pm 3.4)$ nm with shell thicknesses of (48.1 ± 3.4) nm, (42.7 ± 4.5) nm, and (49.8 ± 5.0) nm, respectively (Figure 5.4). After being coated with TiO$_2$, the longitudinal plasmon modes red-shift to 646 nm, 695 nm, and 775 nm in aqueous solutions, respectively. The extinction intensity ratio between the transverse and longitudinal plasmon modes is significantly increased after shell coating. Figure 5.5 shows the representative scattering spectra of the individual (Au nanorod core)/(TiO$_2$ shell) nanostructures. Each scattering spectrum shows two scattering peaks, a low-energy longitudinal mode and a high-energy transverse mode. Red shifts caused by the higher refractive index of the ITO substrate are detected for both plasmon modes. Clear asymmetric line shapes are observed for both modes for the three samples. Under excitation, both the transverse and longitudinal plasmon modes can couple with the scattering of the shell, resulting in Fano resonance. As the longitudinal dipole plasmon energy becomes smaller, the corresponding Fano resonance peak is red-shifted. More interestingly, the transverse plasmon mode of the Au nanorods is greatly magnified in the (Au nanorod core)/(TiO$_2$ shell) nanostructures. In comparison, the transverse plasmon mode of an individual bare Au nanorod is too weak to be detected on our dark-field optical microscope, as reported in our previous work [31]. The amplification of the transverse plasmon peak intensity is believed to be caused by the TiO$_2$ shell. In shells with higher permittivities (or refractive indices), more polarization charges can be induced under the excitation of external light, leading to stronger Coulombic interaction and

therefore higher scattering intensities. I believe that the strong resonance for both the transverse and longitudinal plasmon modes will widen their plasmon-based applications, such as in fluorescence enhancement [32].
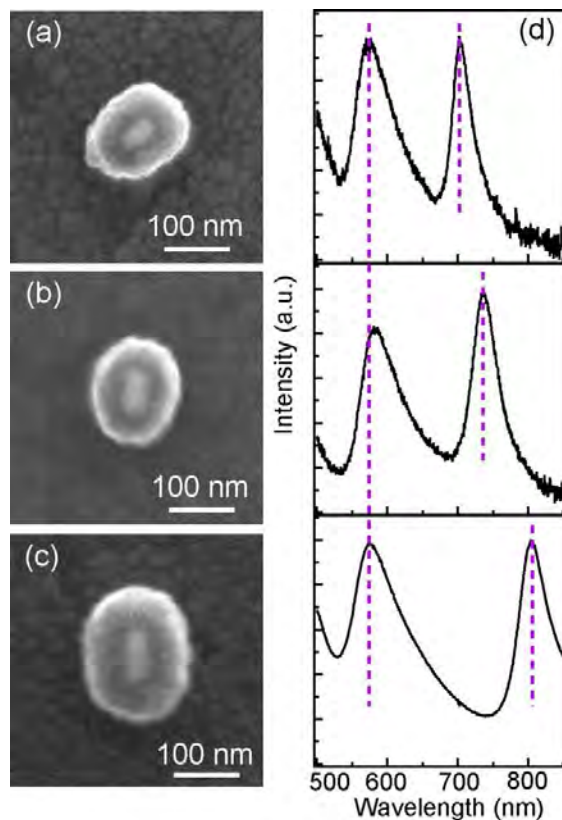
Figure 5.5 Plasmonic response of the three (Au nanorod core)/(TiO$_2$ shell) nanostructure samples. (a–c) SEM images of the individual nanostructures by employing the Au nanorods with longitudinal plasmon wavelengths at 574 nm, 608 nm, and 650 nm, respectively. (d) Corresponding measured scattering spectra. Each spectrum is normalized against the corresponding peak intensity of the longitudinal plasmon mode. The longitudinal plasmon modes red-shift to 705 nm, 735.5 nm, and 805 nm, respectively.

5.2 Summary

In this chapter, distinct Fano resonance is first examined in the scattering spectra of

(Au nanosphere core)/(TiO$_2$ shell) nanostructures. The Fano resonance originates from the strong interference between the broad scattering background of the TiO$_2$ shell and the narrow plasmon resonance of Au nanosphere core. For (Au nanorod core)/(TiO$_2$ shell) nanostructures, both the narrow transverse and longitudinal plasmon resonance of the Au nanorod core can interference efficiently with the scattering background of TiO$_2$ shell. Two strong Fano resonances are therefore observed. Moreover, the longitudinal Fano resonance in (Au nanorod core)/(TiO$_2$ shell) nanostructures can be tailored by changing the plasmon energy of the Au nanorod core. As the longitudinal dipole plasmon energy becomes smaller, the corresponding Fano resonance peak is red-shifted. Furthermore, the transverse plasmon mode of the Au nanorods is greatly magnified after coating with TiO$_2$. I believed the tunable Fano resonance in our (Au nanorod core)/(TiO$_2$ shell) nanostructure can be a promising candidate in biological sensing applications.

References

[1] Fano, U. *Nuovo Cimento* **1935**, *12*, 8.

[2] Fano, U. *Phys. Rev.* **1961**, *124*, 1866–1878.

[3] Rybin, M. V.; Khanikaev, A. B.; Inoue, M.; Samusev, A. K.; Steel, M. J.; Yushin, G.; Limonov, M. F. *Photon. Nanostruct.* **2010**, *8*, 86–93.

[4] Rybin, M. V.; Khanikaev, A. B.; Inoue, M.; Samusev, K. B.; Steel, M. J.; Yushin, G.; Limonov, M. F. *Phys. Rev. Lett.* **2009**, *103*, 023901.

[5] Al-Naib, I. A. I.; Jansen, C.; Born, N.; Koch, M. *Appl. Phys. Lett.* **2011**, *98*, 091107.

[6] Chen, Z. C.; Rahmani, M.; Gong, Y. D.; Chong, C. T.; Hong, M. H. *Adv. Mater.* **2012**, *24*, OP143–OP147.

[7] Chen, Z. C.; Hong, M. H.; Lim, C. S.; Han, N. R.; Shi, L. P.; Chong, T. C. *Appl. Phys. Lett.* **2010**, *96*, 3424793.

[8] Mirin, N. A.; Bao, K.; Nordlander, P. *J. Phys. Chem. A* **2009**, *113*, 4028–4034.

[9] Miroshnichenko, A. E.; Flash, S.; Kivshar, Y. S. *Rev. Mod. Phys.* **2010**, *82*, 2257–2298.

[10] Luk'yanchuk, B.; Zheludev, N. I.; Maier, S. A.; Halas, N. J.; Nordland, P.; Giessen, H.; Chong, C. T. *Nat. Mater.* **2010**, *9*, 707–715.

[11] Hao, F.; Sonnefraud, Y.; Van Dorpe, P. V.; Maier, S. A.; Hals, N. J.; Nordland, P. *Nano Lett.* **2008**, *8*, 3983–3988.

[12] Hao, F.; Sonnefraud, Y.; Van Dorpe, P.; Maier, S. A.; Halas, N. J.; Nordland, P. *Nano Lett.* **2008**, *9*, 2343–2349.

[13] Lassoter, J. B.; Sobhani, H.; Fan, J. A.; Kundu, J.; Capasso, F.; Nordland, P.; Halas, N. J. *Nano Lett.* **2010**, *10*, 3184–3189.

[14] Liu, N.; Weiss, T.; Mesch, M.; Langguth, L.; Eigenthaler, U.; Hirscher, M.; Sönnichsen, C.; Giessen, H. *Nano Lett.* **2010**, *10*, 1103–1107.

[15] Verellen, N.; Sonnefraud, Y.; Sobhani, H.; Hao, F.; Moshchalkov, V. V.; Van Dorpe, P.; Nordlander, P.; Marier, S. A. *Nano Lett.* **2009**, *9*, 1663–1667.

[16] Chen, H. J.; Shao, L.; Man, Y. C.; Zhao, C. M.; Wang, J. F.; Yang, B. C. *Small* **2012**, *8*, 1503–1509.

[17] Shao, L.; Fang, C. H.; Chen, H. J.; Man, Y. C.; Wang, J. F.; Lin, H.-Q. *Nano Lett.* **2012**, *12*, 1424–1430.

[18] Woo, K. C.; Shao, L.; Chen, H. J.; Liang, Y.; Wang, J. F.; Lin, H.-Q. *ACS Nano* **2011**, *5*, 5976–5986.

[19] Brown, L. V.; Sobhani, H.; Lassiter, B.; Nordland, P.; Halas, N. J. *ACS Nano* **2010**, *4*, 819–832.

[20] Sonnefraud, Y.; Verellen, N.; Sobhani, H.; Vandenbosch, G. A. E.; Moshchalkov, V. V.; Van Dorpe, P.; Nordlander, P.; Maier, S. A. *ACS Nano* **2010**, *4*, 1664–1670.

[21] Mukherjee, S.; Sobhani, H.; Lassiter, J. B.; Bardhan, R.; Nordlander, P.; Halas, N. J. *Nano Lett.* **2010**, *10*, 2694–2701.

[22] Zhang, S. P.; Bao, K.; Halas, N. J.; Xu, H. X.; Nordland, P. *Nano Lett.* **2011**, *11*, 1657–1663.

[23] Peña-Rodríguez, O.; Pal, U. *Nanoscale* **2011**, *3*, 3609–3612.

[24] Chen, H. J.; Shao, L.; Li, Q.; Wang, J. F. *Chem. Soc. Rev.* **2013**, *42*, 2679–2724.

[25] Ni, W. H.; Kou, X. S.; Yang, Z.; Wang, J. F. *ACS Nano* **2008**, *2*, 677–686.

[26] Tsung, C.-K.; Kou, X. S.; Shi, Q. H.; Zhang, J. P.; Yeung, M. H.; Wang, J. F.; Stucky, G. D. *J. Am. Chem. Soc.* **2006**, *128*, 5352–5353.

[27] Ming, T.; Kou, X. S.; Chen, H. J.; Wang, T.; Tam, H.-L.; Cheah, K.-W.; Chen, J.-Y.; Wang, J. F. *Angew. Chem. Int. Ed.* **2008**, *47*, 9685–9690.

[28] Chen, H. J.; Sun, Z. H.; Ni, W. H.; Woo, K. C.; Lin, H.-Q.; Sun, L. D.; Yan, C. H.; Wang, J. F. *Small* **2009**, *5*, 2111–2119.

[29] Chen, H. J.; Ming, T.; Zhang, S. R.; Jin, Z.; Yang, B. C.; Wang, J. F. *ACS Nano* **2011**, *5*, 4865–4877.

[30] Chen, H. J.; Shao, L.; Ming, T.; Woo, K. C.; Man, Y. C.; Wang, J. F.; Lin, H.-Q. *ACS Nano* **2011**, *5*, 6754–6763.

[31] Shao, L.; Ruan, Q. F.; Jiang, R. B.; Wang, J. F. *Small* **2014**, *10*, 802–811.

[32] Liu, S.-Y.; Huang, L.; Li, J.-F.; Wang, C.; Li, Q.; Xu, H.-X.; Guo, H.-L.; Meng, Z.-M.; Shi, Z.; Li, Z.-Y. *J. Phys. Chem. C* **2013**, *117*, 10636–10642.

Chapter 6

Conclusion and Outlook

In this thesis, I described my work on (plasmonic metal core)/(semiconductor shell) nanostructures, including the plasmonic and structural evolutions during the sulfidation of Ag nanocubes to form (Ag core)/(Ag$_2$S shell) nanostructures, the synthesis and applications of (Au core)/(TiO$_2$ shell) nanostructures, and the tunable Fano resonances in (Au nanorod core)/(TiO$_2$ shell) nanostructures.

Sulfidation of Ag nanocubes was carried out at both the ensemble and single-particle levels. Extinction measurements of the ensemble Ag nanocube samples reveal that the sulfidation reaction first causes the disappearance of the higher-order triakontadipolar plasmon modes, which originate from the electron charges located at the sharp edges and vertices of Ag nanocubes. This result indicates that the sulfidation reaction begins at the vertices of Ag nanocubes. As the reaction continues, the dipolar plasmon peak undergoes a red shift with the intensity first decreasing and then increasing. Structural characterizations reveal that sulfidation progresses from the outer region to the center of Ag nanocubes. The overall nanostructures maintain their cubic shape. Single-particle scattering spectra indicate that the dipolar plasmon peak is red-shifted and the intensity is reduced during sulfidation. In addition, a new peak appears at the higher energy at the later stage of sulfidation. The differences in the plasmonic variations between the ensemble and single-particle measurements are understood by performing electrodynamic simulations. Sulfidation is initiated at the sharp vertices of Ag nanocubes. As the sulfidation reaction is carried on, each Ag nanocube is truncated gradually from the outer region into a nanosphere. Sulfidation stops at an intermediate stage in the ensemble experiment, while Ag nanocuebs are completely transformed into Ag$_2$S. The new scattering peak at a higher energy is

contributed by Ag_2S.

Although many approaches have been demonstrated in the preparation of Au nanocrystal-coupled TiO_2 nanostructures, the synthesis of (Au nanocrystal core)/(TiO_2 shell) nanostructures has remained relatively challenging, especially when Au nanorod sample is employed as the core. I therefore developed a facile and reliable method for the preparation of plasmonic (Au nanocrystal core)/(TiO_2 shell) nanostructures on the basis of the "seeded growth" method. A Ti(III) compound is employed as the titania source. It undergoes an oxidative process during the titania shell coating. Pre-grown Au nanocrystals are surface-modified to make them negatively charged and facilitate the initial electrostatic adsorption of the Ti(III) species. By using differently-sized Au nanorods as the cores and varying the shell thickness, the plasmon resonance bands of the core/shell nanostructures can be tuned from the visible to near-infrared region. TiO_2 coating has also been successfully carried out on other monometallic and bimetallic Pd, Pt, Au nanocrystals, showing that the method is highly versatile. (Au nanorod core)/(TiO_2 shell) nanostructures are employed to function as the scattering layer in dye-sensitized solar cells. The resultant solar cells exhibit higher power conversion efficiencies in comparison to the cells with the standard TiO_2 scattering layer, while the thickness of the nanostructure scattering layer is much thinner than that of the TiO_2 scattering layer. Moreover, under resonant excitation, (Au nanorod core)/(TiO_2 shell) nanostructures can efficiently utilize photons with energies below the band gap of TiO_2. The generation of reactive oxygen species, including singlet oxygen and hydroxyl radicals, are greatly improved compared to those of the uncoated Au nanorods.

Moreover, I also investigated the Fano resonances of the (Au nanorod core)/(TiO_2 shell) nanostructures. The TiO_2 shell with a higher refractive index can couple with both the transverse and the longitudinal plasmon modes of the Au nanorod core, resulting in the simultaneous observation of Fano resonances in both plasmon modes. In addition, the longitudinal Fano resonance can be tuned by changing the plasmon

energy of the Au nanorod core. The intensity of the transverse plasmon mode on Au nanorods is greatly enhanced after coating with TiO_2 shell.

I believed that my research work during my PhD study will be very helpful for the design and application of metal/semiconductor hybrid nanostructures. The clear understanding of the plasmonic and structural variations during the sulfidation process enables fine tuning of the structural composition and the plasmonic properties of Ag/Ag_2S hybrid nanostructures. This work also provides an elegant route by employing localized surface plasmon resonance to monitor and guide chemical transformation of metal nanocrystals into hybrid nanomaterials with desired plasmonic properties. On the other hand, my study has also provided an attractive way for coating TiO_2 onto various noble metal nanocrystals for achieving the hybridization and the synergistic function, widening its applications in solar energy harvesting, such as in dye-sensitized solar cell and photodynamic therapy. Furthermore, the investigation of the Fano resonances in (Au nanorod core)/(TiO_2 shell) nanostructures will promote their potential applications as ultrasensitive chemical and biological sensors. The simultaneously detectable transverse and longitudinal plasmon modes of Au nanorods after coating with TiO_2 will also promote its applications in optics. As illustrated in this thesis, metal/semiconductor nanostructures integrate plasmonic metal nanocrystals with semiconductors, which will flourish their applications in energy and environment fields. However, great efforts are still required to further investigate the synthesis, plasmonic properties, and applications of metal/semiconductor nanostructures. On the basis of the results shown in this thesis, further explorations can focus on the following aspects.

First, although diverse metal/semiconductor nanostructures have been prepared, the morphology of the overall nanostructures and the interface between the metal and semiconductor components cannot be controlled very well. Therefore, preparation of metal/semiconductor nanostructures, in which the morphologies for the overall as well as each component can be better controlled, needs further progress. For example,

it is still a great challenge to prepare (Au nanorod core)/(TiO$_2$ shell) nanostructures with a shell thickness that is as thin as several nanometers, which will be very helpful for fully utilizing the strong electric field to improve photon harvesting applications.

Second, the mechanisms for plasmon-enhanced photocatalysis with metal/semiconductor nanostructures require further experimental and theoretical studies. Numerous works have suggested plasmon-induced hot-carrier injection from metals to semiconductors. However, this transfer process has been studied only in a few experiments. More efforts are required. Photoelectrochemical measurements would be an effective method. Take (Au nanorod core)/(TiO$_2$ shell) nanostructures as an example, if hot electrons are injected in the conductive band of TiO$_2$, the Femi level of TiO$_2$ will be raised, leading to higher positive potentials measured on an electrochemical station.

Third, multifunctional metal/semiconductor nanostructures, integrating several functions into one nanostructure, are highly desired in practical applications. We have demonstrated that the (Au nanorod core)/(TiO$_2$ shell) nanostructures can efficiently generate reactive oxygen species under near-infrared light illumination. Therefore it will be a promising candidate as a photosensitizer in photodynamic therapy. Moreover, the porous shell can be used to load drugs. The photothermal effect of the Au nanorod core can control the drug release. The (Au nanorod core)/(TiO$_2$ shell) nanostructures are therefore ideal nanomaterials, which can simultaneously realize photodynamic therapy and drug delivery and release in disease treatment.

Nevertheless, I am firmly convinced that the challenges above will be overcome eventually. On the basis of all of the achievements, metal/semiconductor nanomaterials will be widely developed. They therefore will play an irreplaceable role in solving energy and environmental problems in our daily life in the future.

Publications

(1) **<u>Caihong Fang</u>**, Henglei Jia, Shuai Chang, Qifeng Ruan, Peng Wang, Tao Chen*, Jianfang Wang* "(Gold core)/(titania shell) nanostructures for plasmon-enhanced photon harvesting and generation of reactive oxygen species", *Energy Environ. Sci.* **Accepted**.

(2) **<u>Caihong Fang</u>**, Yih Hong Lee, Lei Shao, Ruibin Jiang, Jianfang Wang,* Qing-Hua Xu* "Correlating the plasmonic and structural evolutions during the sulfidation of silver nanocubes", *ACS Nano* **2013**, *7*, 9354–9365.

(3) **<u>Caihong Fang</u>**, Lei Shao, Yihua Zhao, Jianfang Wang,* Hongkai Wu* "A Au nanocrystal/poly(dimethylsiloxane) composite for plasmonic heating on microfluidic chips", *Adv. Mater.* **2012**, *24*, 94–98.

(4) Lei Shao, **<u>Caihong Fang</u>** (equal contribution), Huanjun Chen, Yat Cho Man, Jianfang Wang,* Hai-Qing Lin* "Distinct plasmonic manifestation on gold nanorods induced by the spatial perturbation of small gold nanospheres", *Nano Lett.* **2012**, *12*, 1424–1430.

(5) Ruibin Jiang, Benxia Li, **<u>Caihong Fang</u>**, Jianfang Wang "Metal/semiconductor hybrid nanostructures for plasmon-enhanced applications" *Adv. Mater.* DOI: 10.1002/adma.201400203.

(6) Manda Xiao, Ruibin Jiang, Feng Wang, **<u>Caihong Fang</u>**, Jianfang Wang,* Jimmy C. Yu "Plasmon-enhanced chemical reactions", *J. Mater. Chem. A* **2013**, *1*, 5790–5805.

(7) Zhenhua Sun,* Zhihong Bao, **<u>Caihong Fang</u>**, Jianfang Wang* "Formation of different gold nanocrystal core-resin shell structures through the control of the core assembly and shell polymerization", *Langmuir* **2012**, *28*, 9082–9092.

(8) Xi Wu, Ji-Yao Chen,* Andreas Brech, **<u>Caihong Fang</u>**, Jianfang Wang, P. Johannes Helm, Qian Peng* "The use of femto-second lasers to trigger powerful explosions of gold nanorods to destroy cancer cells", *Biomaterials* **2013**, *34*, 6157–6162.

(9) Qian Li, Ruibin Jiang, Tian Ming, **<u>Caihong Fang</u>**, Jianfang Wang* "Crystalline structure-dependent growth of bimetallic nanostructures", *Nanoscale* **2012**, *4*, 7070–7077.

(10) Baoyou Geng*, **<u>Caihong Fang</u>**, Fangming Zhan, Nan Yu "Synthesis of polyhedral $ZnSnO_3$ microcrystals with controlled exposed facets and their selective gas-sensing properties", *Small* 2008, *4*, 1337–1343.

(11) **<u>Caihong Fang</u>**, Baoyou Geng*, Jun Liu, Fangming Zhan "D-fructose molecule template route to ultra-thin $ZnSnO_3$ nanowire architectures and their application as efficient photocatalyst", *Chem. Commun.* 2009, 2350–2352.

(12) **<u>Caihong Fang</u>**, Shaozhen Wang, Qian Wang, Jun Liu, Baoyou Geng* "Coralloid SnO_2 with hierarchical structure and their application as recoverable gas sensors for the detection of benzaldehyde/acetone", *Mater. Chem. Phys.* 2010, 122, 30–34.

(13) Baoyou Geng*, Fangming Zhan, **<u>Caihong Fang</u>**, Nan Yu "A facile coordination compound precursor route to controlled synthesis of Co_3O_4 nanostructures and their room-temperature gas sensing properties", *J. Mater. Chem.* **2008**, *18*, 4977–4984.

(14) Baoyou Geng*, Fangming Zhan, Han Jiang, Zhoujing Xing, **<u>Caihong Fang</u>** "Facile production of self-assembly hierarchical dumbbell-like CoOOH nanostructures and their room-temperature CO-gas-sensing properties", *Cryst. Growth Des.* **2008**, *8*, 3497–3500.

(15) Baoyou Geng*, Jiahui You, Fangming Zhan, Mingguang Kong, **<u>Caihong Fang</u>**, "Controllable morphology evolution and photoluminescence of ZnSe hollow microspheres", *J. Phys. Chem. C* **2008**, *112*, 11301–11306.